

INFORMATION TO USERS

This manuscript has been reproduced from the microfilm master. UMI films the text directly from the original or copy submitted. Thus, some thesis and dissertation copies are in typewriter face, while others may be from any type of computer printer.

The quality of this reproduction is dependent upon the quality of the copy submitted. Broken or indistinct print, colored or poor quality illustrations and photographs, print bleedthrough, substandard margins, and improper alignment can adversely affect reproduction.

In the unlikely event that the author did not send UMI a complete manuscript and there are missing pages, these will be noted. Also, if unauthorized copyright material had to be removed, a note will indicate the deletion.

Oversize materials (e.g., maps, drawings, charts) are reproduced by sectioning the original, beginning at the upper left-hand corner and continuing from left to right in equal sections with small overlaps.

Photographs included in the original manuscript have been reproduced xerographically in this copy. Higher quality 6" x 9" black and white photographic prints are available for any photographs or illustrations appearing in this copy for an additional charge. Contact UMI directly to order.

ProQuest Information and Learning
300 North Zeeb Road, Ann Arbor, MI 48106-1346 USA
800-521-0600

UMI[®]

Investigation of the non-Arrhenius behavior of Fast Ion Conducting glasses

by

Jeremy Allen Schrooten

**A dissertation submitted to the graduate faculty
in partial fulfillment of the requirements for the degree of
DOCTOR OF PHILOSOPHY**

Major: Materials Science and Engineering

**Program of Study Committee:
Steve W. Martin (Major Professor)
David Cann
Vikram Dalal
Surya Mallapragada
David Martin**

**Iowa State University
Ames, IA
2001**

Copyright © Jeremy Allen Schrooten, 2001. All rights reserved

UMI Number: 3034221

Copyright 2001 by
Schrooten, Jeremy Allen

All rights reserved.

UMI[®]

UMI Microform 3034221

Copyright 2002 by ProQuest Information and Learning Company.
All rights reserved. This microform edition is protected against
unauthorized copying under Title 17, United States Code.

ProQuest Information and Learning Company
300 North Zeeb Road
P.O. Box 1346
Ann Arbor, MI 48106-1346

**Graduate College
Iowa State University**

This is to certify that the dissertation of

Jeremy Allen Schrooten

has met the dissertation requirements of Iowa State University

Signature was redacted for privacy.

Committee Member

Signature was redacted for privacy.

Major Professor

Signature was redacted for privacy.

For the Major Program

TABLE OF CONTENTS

1. GENERAL INTRODUCTION	1
1.1. Thesis Introduction.....	1
1.2. Thesis Organization.....	2
1.3. Thesis Background.....	4
1.3.1. Theory of Glass Formation.....	4
1.3.1.1. Structural Theory.....	4
1.3.1.2. Kinetic Theory.....	7
1.3.2. Theories of Ionic Conductivity.....	11
1.3.2.1. Nernst-Einstein and Diffusion Relations.....	12
1.3.2.2. Models for Activation Energy.....	15
1.1.1.1.1. Weak Electrolyte Model.....	15
1.1.1.1.2. Anderson and Stuart Model.....	16
1.3.3. Models of Non-Arrhenius Behavior.....	18
1.3.3.1. Ngai Coupling Model.....	19
1.3.3.2. Cut-Off Model.....	22
1.3.3.3. Distribution of Activation Energy Model.....	23
1.3.4. Compositional Dependence of Ionic Conductivity.....	24
1.4. Experimental Methods.....	25
1.4.1. Sample Preparation.....	25
1.4.1.1. Preparation of Boron Trisulfide.....	26

1.4.1.2.	Preparation of Fast Ion Conducting Glass	29
1.4.2.	Sample Characterization.....	30
1.4.2.1.	Scanning Electron Microscopy	30
1.4.2.2.	X-Ray Diffraction.....	31
1.4.2.3.	Differential Scanning Calorimetry	32
1.4.2.4.	Density Measurements.....	33
1.4.2.5.	Infrared Absorption Spectroscopy.....	33
1.4.2.6.	Raman Spectroscopy.....	34
1.4.2.7.	Neutron Diffraction	34
1.4.2.8.	Nuclear Magnetic Resonance.....	35
1.4.2.9.	Impedance Spectroscopy.....	36
1.5.	References.....	39
2.	Preparation and Characterization of Boron Oxysulfide Glasses.....	40
2.1.	Abstract.....	40
2.2.	Introduction.....	41
2.3.	Preparation	43
2.4.	Experimental Techniques	44
2.4.1.	Raman Spectroscopy	44
2.4.2.	Differential Scanning Calorimetry	44
2.4.3.	Density Measurements	45
2.4.4.	Nuclear Magnetic Resonance	46
2.5.	Results.....	46
2.6.	Discussion	49

2.7.	Conclusions.....	51
2.8.	Acknowledgements	52
2.9.	References.....	53
2.10.	Captions	54
3.	Structural Characterization of Silver Thioborosilicate Glasses	65
3.1.	Abstract.....	65
3.2.	Introduction.....	66
3.3.	Experimental	67
3.3.1.	Sample Preparation.....	67
3.3.2.	Scanning Electron Microscopy	68
3.3.3.	X-Ray Diffraction	68
3.3.4.	Differential Scanning Calorimetry	68
3.3.5.	Infrared Spectroscopy.....	69
3.3.6.	Raman Spectroscopy	69
3.3.7.	Nuclear Magnetic Resonance	69
3.4.	Results.....	70
3.4.1.	Scanning Electron Microscopy	70
3.4.2.	X-Ray Diffraction	71
3.4.3.	Differential Scanning Calorimetry.....	72
3.4.4.	Raman Spectroscopy	72
3.4.5.	Infrared Spectroscopy.....	73
3.4.6.	Nuclear Magnetic Resonance	73
3.5.	Discussion.....	74

3.6.	Conclusions.....	76
3.7.	Acknowledgements	76
3.8.	References.....	77
3.9.	Captions	78
4.	Ion Scattering Model as an Explanation of Non-Arrhenius Ionic Conductivity	98
4.1.	Abstract.....	98
4.2.	Introduction.....	99
4.3.	Experimental	100
4.3.1.	Sample Preparation.....	100
4.3.2.	Impedance Spectroscopy	101
4.4.	Results.....	103
4.5.	Discussion	104
4.6.	Conclusions.....	114
4.7.	Acknowledgements	115
4.8.	References.....	116
4.9.	Captions	117
5.	General Conclusion	137
5.1.	General Discussion.....	137
5.2.	Recommendations for Future Research.....	138
6.	Acknowledgements	139

1. GENERAL INTRODUCTION

1.1. Thesis Introduction

Ionic conduction in glassy materials has been known since 1884 when Warburg¹ used a piece of Thurger glass as a membrane separating two sodium amalgams. When he placed a d.c. electric field to the glass, he observed that the sodium ions could pass through. Although there were some applications that exploited this property of glass, prior to 1970 the primary interest was in minimizing ionic transport in glasses to produce low loss substrates and envelopes for electronic applications. In the immediate wake of the energy crisis of the 1970's, there was strong interest in the potential of solid glass electrolytes for electrochemical energy storage as in power sources and load leveling². Glasses are exciting electrolytic materials because they have several advantages over their crystalline counterparts. Glasses offer isotropic conductivity with an absence of grain boundaries. Glassy materials offer wide compositional flexibility that allows for the optimization of electrolyte properties and glasses can easily be fabricated into complex shapes. Initial efforts were directed towards the identification of glasses with good ionic conductivities and electrochemical stability.

Traditional glassy ion conductors exhibit Arrhenius temperature dependence to the d.c. conductivity, see Fig. (1-4). Recently, Kincs and Martin³ reported the discovery of a fast ion conducting (FIC) glass with ionic conductivities as high as $10^{-2} (\Omega\text{-cm})^{-1}$. Unfortunately, while this is a very high conductivity for a glassy material, it is still several orders of magnitude lower than that predicted by the low temperature Arrhenius behavior. An example of this behavior is shown in Fig. (4-1). While Kincs and Martin did a thorough

investigation of these materials at low temperatures, they did not explore the temperatures above room temperature. They propose a simple model to explain their observed non-Arrhenius ionic conductivity, but they leave it as a hypothesis with no experimental backing.

This is the point where the present investigation picks up the study of these glasses. Several researchers have since attempted to explain the cause of the behavior observed by Kincs and Martin; however, no conclusive understanding has been given for the true origin of this behavior. Most of the attempts have been purely mathematical fits, with no basis in the physical world. Other researchers simply write off the observed behavior as a fluke of crystallized or phase separated samples. The present investigation examines the high temperature behavior of the same glass compositions that Kincs and Martin investigated to determine if there is ionic conductivity saturation or perhaps even an ionic conductivity maximum. The study then goes on to develop a theory that explains the observed results in a physical manner that is based on current knowledge ionic conductors and glass structure.

1.2. Thesis Organization

This thesis is separated into five sections. The first section includes basic background information on glass formation and structure as well as a discussion of ionic conductivity. Also included in this first section is a detailed discussion on sample preparation as well as a discussion on the characterization techniques that were used.

The second section is a paper that discusses the effects of oxygen contamination in boron sulfide. It is extremely difficult to remove all of the oxygen present in boron trisulfide, and it is generally accepted that there is a small amount of oxygen contamination[†]. However, before this investigation, the effect of this contamination was unknown and unstudied. This

paper finds that the two networks, B_2S_3 and B_2O_3 mix, but that the B_2S_3 network is more robust, tolerating the oxygen contamination with little effect. An unusual occurrence happens as the oxygen concentration approaches 85%. The glass melt becomes unstable due to a large exothermic event causing the glass melt to boil.

The third section of this thesis is a paper that investigates the structure and physical properties of silver iodothioborosilicate ($AgI + Ag_2S + B_2S_3 + SiS_2$) glasses. A detailed SEM and XRD study is included to determine the homogenous nature of the glasses as well as to determine the crystalline fraction. The SEM analysis concludes the samples do indeed contain a small amount of oxygen contamination, but it is insignificantly small. The XRD analysis concludes that to the resolution of the instrument the samples are glassy. It moves on to investigate the structure of the glass and determines that the structure of the glass is primarily composed of SiS_2 and BS_2 tetrahedra with small amounts of B_2S_3 six-membered rings and trigonal units. These structural units appear to intermix with the Ag_2S adding equally to the B_2S_3 structures and to the SiS_2 structures. The addition of AgI has very little effect on the structure of the glass due to AgI dissolving into voids in the glass causing a network expansion. This occurs without disrupting the short-range order of the glass.

The final section of the thesis is a paper that proposes a model to explain the non-Arrhenius temperature dependence to the ionic conductivity. The ionic conductivity is measured to near the glass transition temperature of the samples and determines that the ionic conductivity continues to increase, but at a much slower rate than at lower temperatures. The trend is of ionic conductivity saturation, however, the glass transition occurs before this can be conclusively determined. The proposed model, the Ion Scattering Model, takes a physical approach to explain the cause of the non-Arrhenius deviation. By assuming the high

temperature conductivity is limited by mobile ion scattering, good fits with experimental data were achieved in the non-Arrhenius region. Due to the assumption that the ions do not conduct independently, the low temperature conductivity is over-estimated.

1.3. Thesis Background

1.3.1. Theory of Glass Formation

To begin our discussion of glass formation, it seems appropriate that a definition of what constitutes a glass is in order. Several definitions have been proposed; for instance, The American Society for Testing and Materials (ASTM) at one time defined glass as “an inorganic product of fusion that has been cooled to a rigid condition without crystallizing.”⁵ This definition seems too restrictive as there are several known organic glass systems and fusion is not the only method to form a glass. In order to not be overly restrictive in the definition of a glass, a more appropriate definition would be: a solid with a liquid-like structure; a non-crystalline solid, or simply; an amorphous solid⁵.

There are two basic theories for glass formation: structural theory, and kinetic theory⁵, we will begin with the structural theory.

1.3.1.1. Structural Theory

Zachariasen provided the classical argument for the structural theory of glass formation in oxide systems⁶. His hypothesis is largely based on the idea that the internal energy of the glass is comparable to that of the corresponding crystal. In order to meet this criterion, it is necessary that the glass and crystal be made up of similar polyhedra that are

joined in similar ways, with the exception that the glass contains disorder in the form of a distribution of bond angles and lengths. In order to support this disorder without greatly increasing the internal energy it is necessary that these polyhedra be joined only by corners and not by faces or edges. By analysis of crystalline structures exhibited by oxides of various stoichiometries, A_mO_n , Zachariasen found that only compounds of the stoichiometry AO_2 , A_2O_3 , A_2O_5 , AO_3 , and A_2O_7 had the necessary corner sharing polyhedra to support glass formation. These compounds were termed *network formers* or *glass-formers* to designate their inherently good glass forming character. As a result of his analysis, Zachariasen stated that there are four rules to glass formation (known as Zachariasen's criteria) in a compound such as A_mO_n :

1. An oxygen atom is linked to no more than two atoms of A.
2. The oxygen coordination around A is small, three or four.
3. The cation polyhedra share corners, not edges, not faces.
4. At least three corners are shared

Other compounds such as alkali oxides, alkaline earth oxides and some transition metal oxides dissolve in and react with network formers. When one of these compounds is added to a network former, the reaction is to break up the continuous network of "bonding oxygen" (BO), as shown in Fig. (1-1). The result of this reaction is that many of the physical properties of the melt and the cooled glass such as the temperature dependence of the viscosity, glass transition temperature, density, coefficient of thermal expansion and ionic conductivity are all modified, hence these materials are called *network modifiers*.

There is a third class of materials known as *intermediate modifiers*. They can go into the glass network as either a network former or modifier depending on the glass compositions involved.

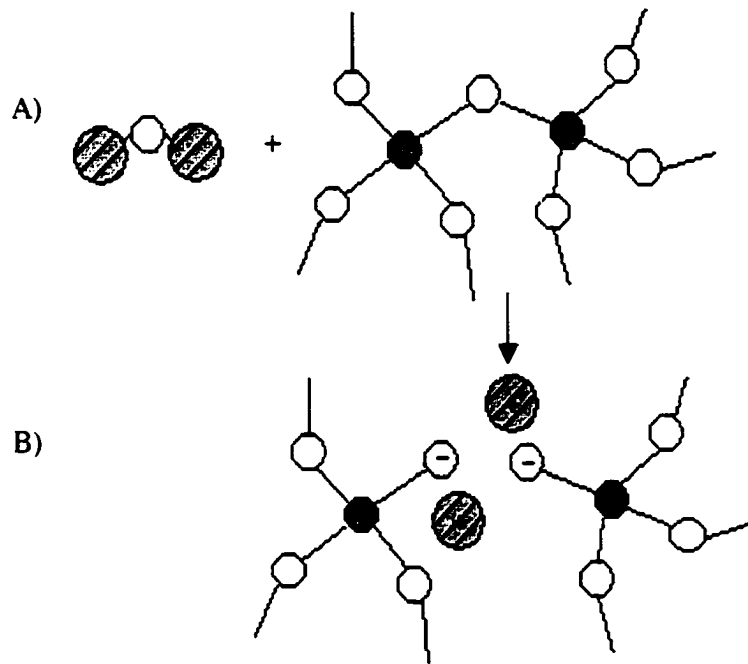


Figure (1-1). Schematic showing the reaction of a modifier oxide with a glass-forming oxide.
A) intact glass forming network, B) formation of a pair of non-bridging oxygen

Support for Zachariasen's criteria grew by the successful prediction of glass formation in systems that had not previously been vitrified based on their adherence to these rules. Zachariasen's contribution to the theory of glass formation is quite significant; however, the discovery of glass formation in non-oxide systems and systems that do not follow his criteria have led to the development of other glass forming theories.

1.3.1.2. Kinetic Theory

The question “Which compounds can form a glass” should really be phrased “At what rate should a given liquid be cooled to bring it into a glassy state?” It is well established that *all liquids*, including water and molten metals, can be vitrified providing the rate of cooling is rapid enough to avoid crystallization below the freezing point⁵. In order for crystallization to occur, a measurable amount of nuclei must form first and then those nuclei must grow at a measurable rate. The sequence in which these events occur is important. It is possible to have a fast growth rate but no nuclei present; in such a situation, the material would still form a glass. The following steps are used to determine whether a system will form a glass⁵:

1. Calculate the rate of nucleation, I , as a function of temperature.
2. Calculate the rate of crystal growth, u , as a function of temperature.
3. Combine (1) and (2) to determine the volume fraction of crystallization when the mass is held at a given temperature for a length of time. This is normally accomplished by using the Johnson-Mehl-Avrami equation and developing T-T-T (time-temperature-transformation) diagrams.

Let us first consider the nucleation rate. First off, there are two different types of nucleation: homogeneous and heterogeneous. If a liquid is cooled below its equilibrium melting temperature, it might be expected that the liquid phase would spontaneously solidify (crystallize)⁷. This is; however, not always the case. The reason for this behavior is that the container walls or impurity particles often catalyze the formation of nuclei. This process is

known as heterogeneous nucleation. In the event there is no catalyst to nuclei formation is known as homogeneous nucleation. The nucleation rate can be expressed by Eq. (1-1),

$$I = n \cdot v \cdot e^{-\frac{N}{R \cdot T} \cdot \frac{16 \cdot \pi \cdot \sigma^3}{3 \cdot (\Delta H_f)^2} \cdot \left(\frac{T_m}{\Delta T}\right)^2} \cdot e^{-\frac{\Delta E_D}{R \cdot T}} \quad (1-1)$$

where n is the number of atoms, v is the atomic vibration frequency, N is Avogadro's number, R is the gas constant, T is the absolute temperature, σ is the surface energy of the interface per unit area, ΔH_f is the heat of fusion per unit volume, T_m is the melting temperature, ΔT is the undercooling, ΔE_D the energy required for an atom to cross the liquid-solid interface, this is also the energy required for diffusion.

The growth rate of the nuclei strongly depends on the speed at which atoms can diffuse from the liquid region to the interface. The growth rate can be determined by Eq. (1-2), where f is the fraction of the surface area on which growth sites may be

$$u = \frac{f \cdot R \cdot T}{3 \cdot N \cdot \pi \cdot a^2 \cdot \eta(T)} \cdot \left(1 - e^{-\frac{\Delta H_f \cdot \Delta T}{R \cdot T \cdot T_m}}\right) \quad (1-2)$$

available, a is the distance between the last liquid site and the first solid site, and η is the viscosity.

Figure (1-2) is a plot of the nucleation and the growth rates versus temperature. Note that the peak nucleation rate occurs at a temperature below that of the peak growth rate. As a result of this, the degree of overlap gives an indication as to the ease in which the liquid can form a glass upon cooling: the smaller the overlap, the easier the glass formation.

To determine the fraction of material crystallized as a function of heat treatment time, one must combine the equations for nucleation and growth. This is accomplished using the Johnson-Mehl-Avrami equation⁵, which is given as Eq. (1-3), where V_x is the volume of

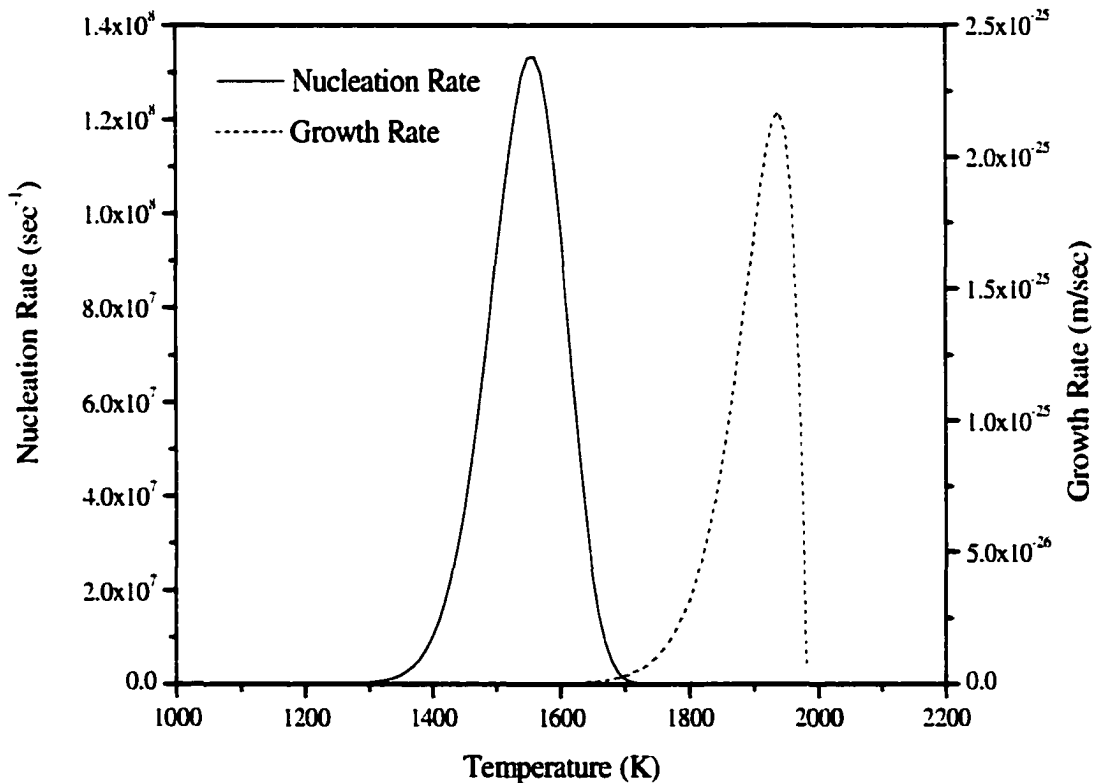


Figure (1-2). Dependence of nucleation and growth rate on temperature.

crystals, V_0 is the entire volume, and t is time. Equation (1-3) can be approximated by Eq. (1-4). Using this equation, curves can be constructed that yield the values of t necessary to cause a given volume fraction crystallization, X , in an isothermal heat treatment at temperature T . These curves are called T-T-T (time-temperature-transformation) curves. An example curve is given in Fig. (1-3).

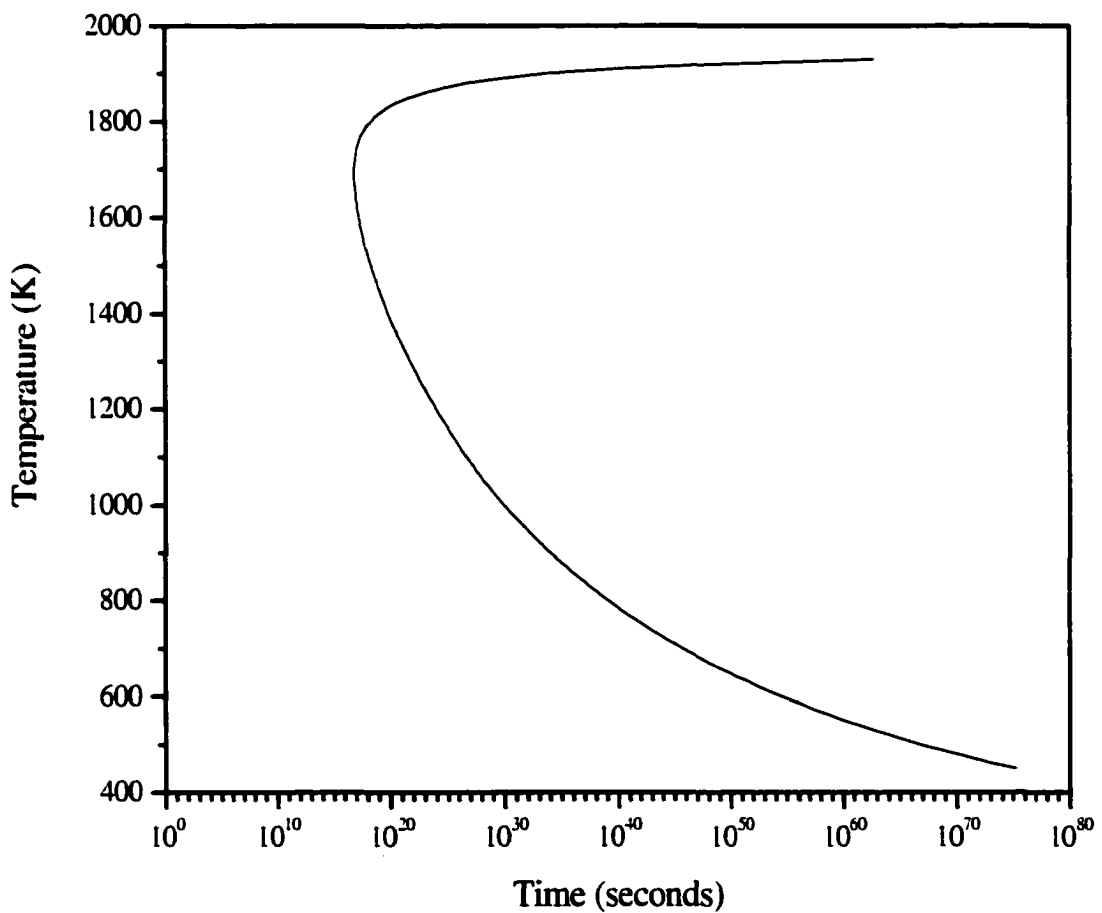


Figure (1-3). Time-Temperature-Transformation diagram for silica.

$$X = \frac{V_x}{V_o} = 1 - e^{-\frac{\pi \cdot I \cdot u^3 \cdot t^4}{3}} \quad (1-3)$$

$$\approx \frac{\pi \cdot I \cdot u^3 \cdot t^4}{3} \quad (1-4)$$

The criterion for glass formation is generally considered to be a crystallized fraction of $\leq 10^{-6}$, which is the accepted instrumental limit for detecting the presence of crystals. If the heat treatments are such that one is always to the left of the curve, detectable crystallization is avoided. Therefore, glass formation will occur so long as the cooling rate is faster than the rate given by the tangent to the T-T-T curve.

1.3.2. Theories of Ionic Conductivity

The total conductivity of a system is given by the sum of the contributions of all of the charge carrying species. However, since in most glass systems transport is carried by only one species (an ion), the conductivity of the material is determined by the conductivity of the ion². Since glasses are isotropic materials, the conductivity due to alkali cations may be represented as shown in Eq. (1-5), where n is the number of mobile cations, Z is the

$$\sigma = n \cdot Z \cdot e \cdot \mu \quad (1-5)$$

valence of the cation, e fundamental unit of charge, and μ is the cation mobility. Models to understand the importance of these terms will be developed later; first functional forms of these terms will be developed.

1.3.2.1. Nernst-Einstein and Diffusion Relations

The variation in ionic conductivity with temperature, composition, and structure is the key to understanding transport phenomena in both glasses and crystals². The ionic nature of conduction in glass has been known for about a century where the electric current is carried entirely by ions. The conductivity usually increases continuously with increasing temperature in an Arrhenius fashion, as shown in Fig. (1-4). This process is commonly described by the Nernst-Einstein Equation, shown in Eq. (1-6), where D is the diffusivity, k_b is Boltzmann's constant, and T is absolute temperature.

$$\frac{\sigma}{D} = \frac{n \cdot (Z \cdot e)^2}{k_b \cdot T} \quad (1-6)$$

The random walk model gives us the expression for diffusivity, Eq. (1-7), where λ is the jump distance and Γ is the jump frequency. The jump frequency is a thermally activated process that can be determined from Eq. (1-8), where ν_0 is the vibrational frequency of an ion in a potential well and ΔS_m and ΔH_m are the entropy and enthalpy of motion, respectively. Rewriting Eq. (1-6) in a more useful form gives Eq. (1-9) and Eq. (1-10), where ΔE_A is the

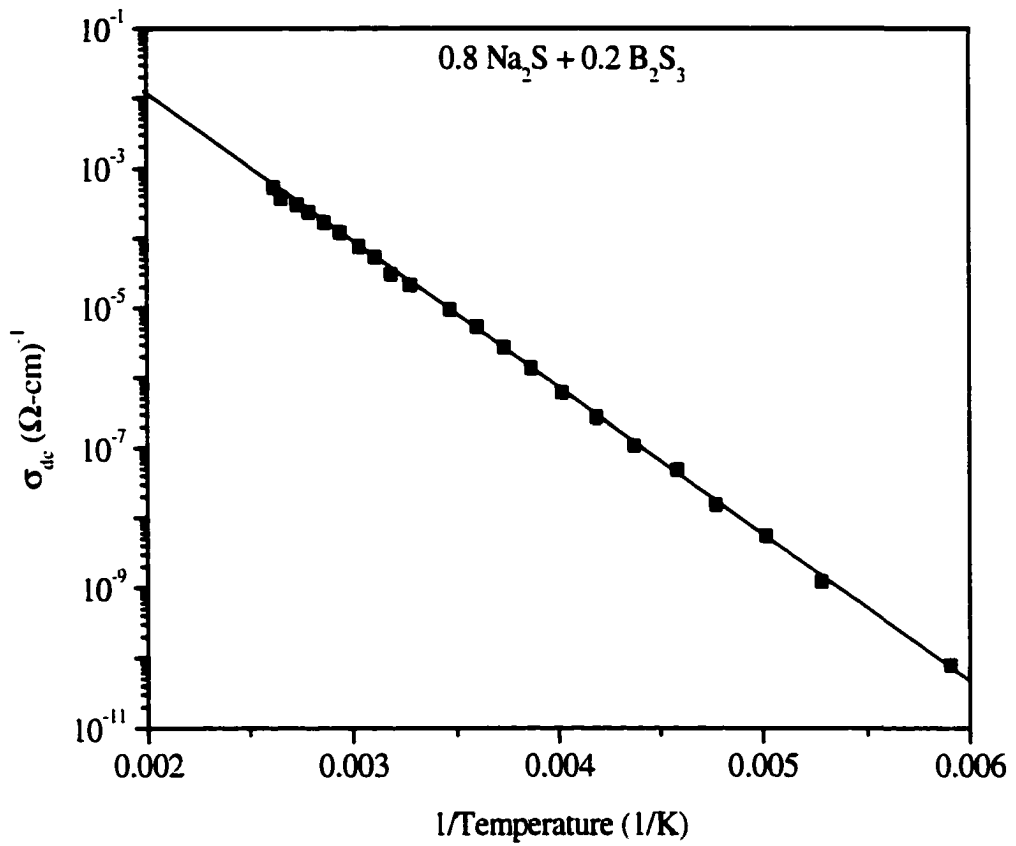


Figure (1-4). Typical Arrhenius behavior exhibited by ionic conductivity. (From ref. 12)

$$D = \frac{1}{6} \cdot \lambda^2 \cdot \Gamma \quad (1-7)$$

$$\Gamma = v_0 \cdot e^{\frac{-\Delta H_m}{k_b \cdot T}} \cdot e^{\frac{\Delta S_m}{k_b}} \quad (1-8)$$

activation energy as determined from the slope of an Arrhenius plot and γ is a geometrical constant that describes the number of directions an ion can hop. Inherent in the Nernst-Einstein equation are three important assumptions. First, it assumes that the activation

$$\sigma = \frac{n \cdot \gamma \cdot (Z \cdot e)^2 \cdot \lambda^2 \cdot v_0 \cdot e^{\frac{-\Delta H_m}{k_b \cdot T}} \cdot e^{\frac{\Delta S_m}{k_b}}}{k_b \cdot T} \quad (1-9)$$

energy for conductivity is the same as the activation energy for diffusion. Second, it requires that the field strength be sufficiently low so that the conductivity is field independent in order to be compatible with the random walk model². Third, it assumes that all diffusive species

$$\sigma = \frac{\sigma_0}{T} \cdot e^{\frac{-\Delta E_A}{k_b \cdot T}} \quad (1-10)$$

are charge carries and; therefore, neglects the possibility of a neutral complex². An advantage of plotting conductivity data in an Arrhenius fashion as shown in Fig. (1-4) is that if the slope of the data is equal to the activation energy in Eq. (1-10) divided by Boltzmann's constant.

Examining Eq. (1-10) shows that the pre-exponent will only vary by one or two orders of magnitude at most as a function of composition. Therefore, large improvements to conductivity can only be achieved through modification of the activation energy, ΔE_A .

1.3.2.2. Models for Activation Energy

There are two possible origins of the activation energy of ionic conduction. The energy barrier may be a result of difficulties in the ion migrating through the glassy network (carrier mobility), or it may be the result of cations dissociating from the anions (carrier creation). The models for activation energy may be distinguished based on their emphasis on carrier creation or carrier mobility. The weak electrolyte model focuses on the composition and temperature dependence of the dissociated carrier concentration, while the Anderson and Stuart model focus on the ion mobility through the glass structure.

1.1.1.1.1 Weak Electrolyte Model

The weak electrolyte model suggests that there are two types of cations: dissociated and associated. The dissociated ions are the ions that have sufficient energy to overcome the coulombic attraction to the network-forming anion and contribute to conduction. Therefore, the activation energy is the energy necessary to perform this dissociation.

The applicability of this model can be evaluated by using the Debye-Huckel reciprocal length², Eq. (1-11), where ϵ_{inf} is the high frequency permittivity, ϵ_0 is the permittivity of free space, C_i is the concentration of i^{th} ion, Z is the valence of the i^{th} ion, and e is the fundamental unit of charge. The Debye-Huckel theory is only accurately used when

$$K^{-1} = \epsilon_{\text{inf}} \epsilon_0 \frac{k_b \cdot T}{4 \cdot \pi} \left(\frac{1}{\sum_i C_i \cdot Z_i \cdot e^2} \right)^{\frac{1}{2}} \quad (1-11)$$

K^{-1} exceeds the inter-ionic separations. Thus, this approach would appear inappropriate for use in concentrated electrolytes such as FIC glasses².

1.1.1.1.2 Anderson and Stuart Model

Anderson and Stuart separate the activation energy for conduction into two terms. The first is called the binding energy term (ΔE_b) and is used to describe the energy necessary to dissociate an ion from the network. The second term is called the strain energy term (ΔE_s) and is used to describe the energy necessary for an ion to move through the interstices in the glass network⁸. Figure (4-11) is a graphical representation of what happens as an ion migrates through the glass network.

The binding energy term can be expressed as Eq. (1-12), where Z and Z_0 is the

$$\Delta E_b = \frac{Z \cdot Z_0 \cdot e^2}{\gamma} \cdot \left(\frac{1}{r+r_0} - \frac{2}{\lambda} \right) \quad (1-12)$$

valence of the ion pair, e is the fundamental unit of charge, r is the radius of the migrating ion in its equilibrium position, r_0 is the radius of the non-bridging ion bonded to the migrating ion, λ is the jump distance, and γ is a covalency parameter used to describe the ease of

polarizability of the ions. Experimentally, γ is found to be equal to the dielectric constant of the glass.

The strain energy term can be expressed as Eq. (1-13), where G is the shear modulus, r is the ionic radius, and r_D is the radius of the opening through which the ion must move to get to the next available interstitial site. The use of this equation has been criticized by

$$\Delta E_s = 4 \cdot \pi \cdot G \cdot r_D \cdot (r - r_D)^2 \quad (1-13)$$

McElfresh and Howitt⁹ because it predicts that the strain energy decreases with r_D for $r_D < r/3$, a physically unrealistic result. McElfresh and Howitt propose that this inconsistency is due to the inappropriate application of Frenkel's theory for a spherically symmetric strain field. Such an approximation is incorrect for diffusing because the diffusing atom must move into a vacant site and leave one behind. Therefore, there is little or no strain immediately in front of or behind the moving atom. McElfresh and Howitt suggest that the strain is instead associated from the adjacent atoms moving aside to create an opening large enough for the diffusing atom to squeeze through. The modified strain energy term derived by McElfresh and Howitt is given in Eq. (1-14).

$$\Delta E_s = \frac{\pi \cdot G \cdot (r - r_D)^2 \cdot \lambda}{2} \quad (1-14)$$

The Anderson and Stuart model calculate the strain energy contribution to the total activation energy based on the elastic properties of the bulk material. Such a treatment of a

microscopic process by a macroscopic property is at best an approximation for the diffusion of an inert gas diffusing through a glass much less alkali ions conducting through a glass². It is certain that substantial interactions between the cations and the doorway atoms of the highly charged network have been ignored².

1.3.3. Models of Non-Arrhenius Behavior

There are several models that have been developed to attempt to explain the non-Arrhenius ionic conductivity seen in several fast ion conducting systems. Non-Arrhenius temperature dependence for the d.c. conductivity of glassy materials was first reported in 1978 by Ingram et al⁴⁶ where they saw a non-Arrhenius temperature dependence in glassy $\text{Ag}_7\text{LiAsO}_4$. They attributed the non-Arrhenius behavior as a result of the “unfreezing” of the glass network and the onset of localized anionic motions, which may then facilitate the migration of mobile cations. However, they do not develop their model any further than the above statement.

It wasn't until the mid 1990's that interest in the non-Arrhenius behavior started to pick up when Kins and Martin saw a very large non-Arrhenius behavior in the silver iodothioborosilicate system³. They suggested that this behavior may represent a limit to the maximum conductivity possible in a glassy system and could that the behavior may be explained by mobile ion scattering; however, this hypothesis is not developed further.

With the suggestion that this behavior might limit the ion conductivity, several researchers tried to explain the behavior. Maass et al.⁴⁸ used Monte Carlo simulations to try to understand the cause of the behavior. They learned that if you use a model of charged

particles moving between the sites of a lattice with random site energies and take into account coulombic interactions it was possible to accurately model the experimental data published by Kins and Martin. This model is the most useful to date in that it actually fits the experimental data, the drawback is that it does this by using several scaling parameters. In addition, it does not explain the nature of the coulombic interaction nor does it explain the differences in conductivity seen from one glass system to another.

The remaining discussion on non-Arrhenius models will be a more detailed look into three of the more general models: Ngai Coupling Model (CM), the Cutoff Model (COM), and the Distribution of Activation Energy Model (DAE). Both the CM and COM are theoretical simulations that are used more to model the observed behavior than attempt to explain the origin of it while the DAE model is a more physical model.

1.3.3.1. Ngai Coupling Model

The coupling model was originally developed for dielectric polarization involving permanent dipoles or non-percolating charged particles¹⁰. This model involves two coupled response equations. The first is applied at very short times and high frequencies and the second is for long times and low frequencies. A crucial assumption that the coupling model makes is that there exists a temperature independent microscopic time, t_c , before which interactions between ions has no effect on the dynamics of an ion¹¹. The ion hopping correlation function for $t < t_c$ is given by Eq. (1-15). Equation (1-16) is the independent

$$C(t) = e^{-\frac{t}{\tau_0}} \quad t \leq t_c \quad (1-15)$$

$$\tau_0(T) = \tau_{inf} e^{\frac{\Delta E_A}{k_b \cdot T}} \quad (1-16)$$

hopping relaxation time of an ion with an attempt frequency of τ_{inf}^{-1} over its energy barrier ΔE_A . At $t > t_c$ the effect of nonlinear classical mechanics between the ions sets in and slows down the relaxation rate¹¹. This modifies the correlation function to assume the Kohlrausch's stretched exponential form as given in Eq. (1-17)¹¹, where n is a coupling

$$C(t) = e^{-\left(\frac{t}{\tau_\sigma}\right)^{1-n}} \quad t > t_c \quad (1-17)$$

parameter limited to $0 \leq n < 1$ and is a measure of the degree of slowing down of the relaxation time¹¹. Macdonald¹⁰ notes that for a conductive-system dispersive response (such as in a glassy FIC material) a pure stretched exponential is inappropriate. He suggests that Eq. (1-17) should be replaced with Eq. (1-18). The requirement of continuity of the correlation function at $t = t_c$ gives rise to Eq. (1-19). This equation is important because it has been used to explain many experimental facts such as the isotope mass dependence of the conductivity and the difference between NMR and conductivity relaxations¹¹.

$$C(t) = e^{-\left(\frac{t_c}{\tau_\sigma}\right)^{1-n}} - \left(\frac{t}{\tau_\sigma}\right)^{1-n} - \left(\frac{t_c}{\tau_\sigma}\right)^{1-n} \quad t \geq t_c \quad (1-18)$$

$$\tau_\sigma = \left(t_c^{-n} \cdot \tau_{inf}\right)^{\frac{1}{1-n}} \cdot e^{\frac{-\Delta E_A}{(1-n) \cdot k_b \cdot T}} \quad (1-19)$$

Equations (1-15) and (1-18) give the correlation function in two pieces. The formal expression for the correlation function, $C(t)$, is given in Eq. (1-20)¹¹. From $g(\tau)$, the average conductivity relaxation time $\langle \tau_{inf} \rangle$ can be calculated and the d.c. conductivity is given by Eq. (1-21), where ϵ_∞ is the permittivity of free space and ϵ_0 is the dielectric constant of the material. Macdonald¹⁰ notes that although equations (1-15) and (1-18) lead to the same result at $t = t_c$, it is clear that there will be a discontinuity in the slope at this point. This discontinuity is a result of the piecewise construction of the relaxation function. A completely satisfactory treatment would presumably be continuous in all derivatives¹⁰.

$$C(t) = \int_0^\infty g(\tau) \cdot e^{-\frac{t}{\tau}} d\tau \quad (1-20)$$

$$\sigma_{dc} = \frac{\epsilon_0 \cdot \epsilon_{inf}}{\langle \tau_{\sigma} \rangle} = \frac{\epsilon_0 \cdot \epsilon_{inf}}{\int_0^{\infty} \tau \cdot g(\tau) d\tau} \quad (1-21)$$

1.3.3.2. Cut-Off Model

Many frequency response models that are associated with a distribution of relaxation time involve a physically possible low-frequency response. However, their treatment of high frequency behavior is not limited to frequencies that are physically possible. The Cut-off Model (COM) avoids this problem by cutting off a distribution of relaxation times at some small non-zero time, τ_{min} ¹⁰. This treatment produces a smooth transition from the low temperature behavior to the high temperature behavior avoiding the problem of the coupling model. The cutoff model defines U_1 as an un-normalized measure or model quantity (conductivity in this case) of interest¹⁰. It is then mathematically convenient to define the normalized form of U_1 as I_1 in terms of a distribution of relaxation times, $g_1(\tau)$ ¹⁰, as given in Eq. (1-22), where x is τ/τ_k , τ_k is a characteristic response time, Ω is τ_k times the frequency, and $G_1(x)$ is $\tau_k g_1(\tau)$.

$$I_1(\Omega) \equiv \frac{U_1(\Omega) - U_1(\infty)}{U_1(0) - U_1(\infty)} = \int_0^{\infty} \frac{G_1(x)}{1 + i\Omega \cdot x} dx = \int_{-\infty}^{\infty} \frac{x \cdot G_1(x)}{1 + i\Omega \cdot e^{\ln(x)}} d\ln(x) \quad (1-22)$$

In order to achieve the appropriate cutoff, one needs an available $G(x)$ expression that is defined over the full range of x . The integration can then be performed by replacing one or more of the integration limits of Eq. (1-22) with finite, nonzero values¹⁰.

1.3.3.3. Distribution of Activation Energy Model

The distribution of activation energy (DAE) model assumes that there is an energy profile in the host glass where the conducting cation resides in potential energy wells. A simple representation of this is shown in Fig. (4-11). The energy barrier for conduction consists of two parts, a coulombic interaction between the conducting cation and the non-bridging sulfur (NBS), and a strain energy that is associated with the strain that occurs when the ion must squeeze through openings in the structure in order to hop to the adjacent site. The total activation energy for conduction is the sum of these two contributions. An extension of this model is to treat the ions as residing in sites that are randomly distributed throughout the glass and are expected to have variations in the local bond distances, bond angles, and coordination numbers that will lead to these sites exhibiting a variation or distribution of activation energies for ionic conduction⁷⁷. The choice of the appropriate mathematical distribution to use for the DAE is subject to choice, however with a few reasonable assumptions the choices narrow considerably. The DAE is assumed to be continuous, centered about a mean, and symmetrical to high and low values⁷⁷. These assumptions make the use of a Gaussian distribution obvious. A Gaussian distribution takes the form of Eq. (1-23), where E_m is the average activation energy and E_b is the activation energy standard deviation. Figure (4-12) is a plot of this equation with E_b and E_m equal to

0.037 eV and 0.248 eV respectively. The values of E_b and E_m can be experimentally determined by performing NMR experiments on the cation of interest.

$$z(E_a) = \frac{1}{\sqrt{2 \cdot \pi \cdot E_b}} e^{-\frac{(E_m - E_a)^2}{2 \cdot E_b^2}} \quad (1-23)$$

1.3.4. Compositional Dependence of Ionic Conductivity

Kincs¹² did an extensive investigation into the effect composition has on ionic conductivity. Kincs states that there are five factors that effect conductivity:

1. Cation Polarizability – It has been demonstrated that polarizability is the most important characteristic for the modifier cation in regards to increasing room temperature ionic conductivity.
2. Anion Polarizability – Larger, more polarizable glass-former anions have been shown to exhibit improved ionic conductivity.
3. Glass-Former Cation – It has been shown that little variation exists when data is interpreted with respect to glass-former cations. The dominating factor here is the glass system that remains glass forming at highest modifier cation concentration will have the highest conductivity.

4. Halide Salts – The addition of halide salts to the glass has been shown to maximize the conductivity of glass; however, they degrade the thermal properties.
5. Mixed Glass-Former Effect – The mixing two glass-former cations, boron and silicon for example, has been experimentally shown to increase conductivity as well as the glass transition temperature of the glass.

Keeping these factors in mind, Kincs¹² chose to work in the $\text{AgI} + \text{Ag}_2\text{S} + \text{B}_2\text{S}_3 + \text{SiS}_2$ system to develop the highest conductivity for any glassy fast ion conductor to date.

1.4. Experimental Methods

This section is divided up into two parts. The first part describes the basic procedures used to prepare the glassy samples. The second part describes the instrumentation that will be used to characterize and test the samples.

1.4.1. Sample Preparation

The most difficult part of the sample preparation is the production of boron trisulfide (B_2S_3). Boron trisulfide is not commercially available in a pure form and; therefore, must be produced in the laboratory. Because B_2S_3 is unstable in either water or air, special precautions must be used to ensure that the material is in its pure form.

In order to turn pure B_2S_3 into a fast ion conductor, additional chemicals need to be added. Fortunately, most of these are commercially available in pure form.

1.4.1.1. Preparation of Boron Trisulfide

The method used for the production of B_2S_3 is a modified version of Martin and Bloyer¹³. The problem with Martin and Bloyer's method is that it is limited to batch sizes of a maximum of only four grams; in the modified version, successful batches of forty grams have been produced.

High purity B_2S_3 can be prepared by the direct reaction of elemental boron and sulfur at high temperature (850°C) in a pyrolytically carbon coated (carburized), evacuated silica ampoule. The first step in this process is the manufacture of the specially prepared silica tube. A schematic of the tube is given in Fig. (1-5). Once the tube is prepared, it is washed

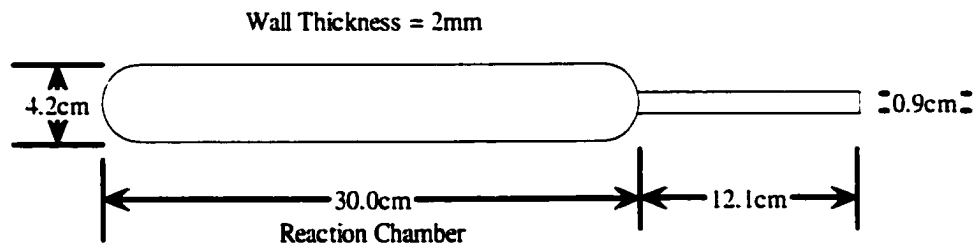


Figure (1-5). Schematic drawing of reaction tube for preparation of boron trisulfide.

with a solution of ammonium bifluoride. If this step is skipped, it is likely that the pyrolytic carbon will not adhere to the silica. To coat the inside of the tube with pyrolytic carbon, the tube is placed in a tube furnace at 950°C with approximately one inch of the open end remaining outside the furnace. Air is passed through the tube for twenty minutes followed by nitrogen gas for an additional twenty minutes. The nitrogen gas is then bubbled through an

acetone bath via a gas diffuser and directed into the silica tube. In order to evenly coat the entire length of the reaction chamber of the tube, it is necessary to use a specially designed “coater”, see Fig. (1-6). The coater consists of a small motor that drives an alumina tube in such a way that the alumina slides along the length of the reaction chamber of the silica tube. The flow rate of the nitrogen gas is approximately 20 cc/min for twenty minutes. At 950°C, the acetone gas anaerobically decomposes to ethanol leaving behind a thin pyrolytic coating of carbon. It is important to use a slow flow rate otherwise the pyrolytic coating is significantly weakened. The tube was then purged an additional twenty minutes with pure nitrogen gas. The only measure of the appropriate thickness of the coating was that once absolutely no light could penetrate through, the coating was thick enough.

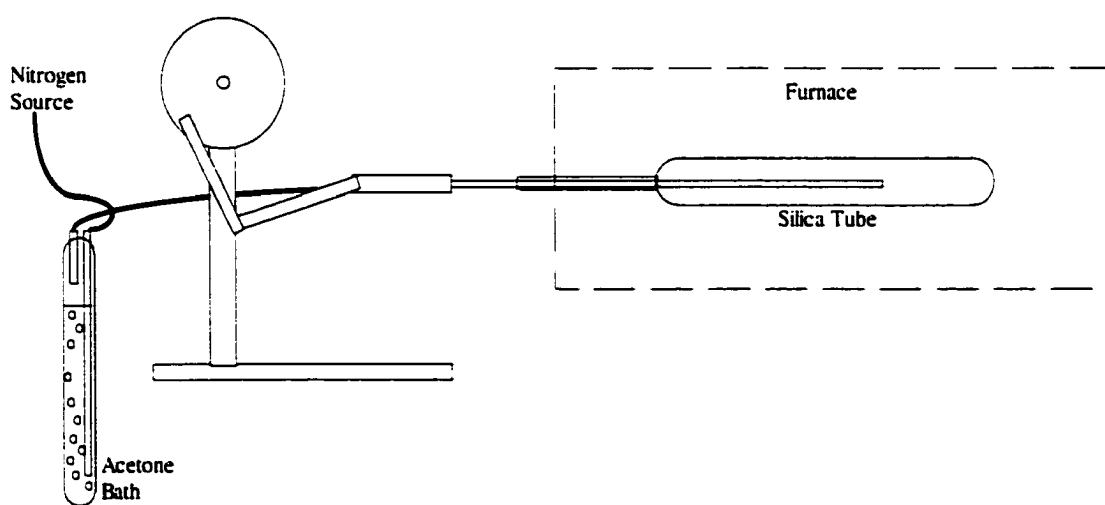


Figure (1-6). Schematic drawing of pyrolytic carbon coating system.

Once the carburized tube is prepared, a valve is fitted to the open end that is then connected to a liquid nitrogen trap in series with a roughing vacuum pump. Under vacuum with the valve open, the tube is passed over an oxy-propane torch to remove any moisture

from the interior of the tube. The valve is then closed and disconnected from the liquid nitrogen trap leaving a vacuum in the tube. The assembly is then placed in an oxygen- (<0.1 ppm) and water- (<0.1 ppm) free helium atmosphere glovebox.

Inside the glovebox, the valve is removed and stoichiometric amounts of boron (amorphous, < 1 μ m, 99.999% pure, Cerac) and sulfur (99.9999% pure, Cerac) totaling 40 grams were loaded into the tube. The valve is refitted to the tube, ensuring that the valve is closed, the filled tube and valve is removed from the glovebox. A vacuum is once again drawn on the tube and the open end is sealed with an oxy-propane torch. The sealed tube is heat according to the schedule in Table (1-1) while being rotated at 5 rpm at an angle of 5°.

Table (1-1). Heating schedule for production of boron trisulfide.

Heat Rate (°C/min)	Temperature (°C)	Hold Time (min)
3	450	60
3	650	60
3	850	480

After the heating schedule is complete, the tube is taken out of the furnace and allowed to air cool. Once cool, the tube is returned to the glovebox where it is broken open. If all went as planned, inside the tube is a 40-gram ingot of pure B₂S₃.

1.4.1.2. Preparation of Fast Ion Conducting Glass

Conductivity measurements by impedance spectroscopy require samples to be of uniform dimensions. For this reason, all FIC samples were prepared in disc form.

Appropriate amounts of all starting materials, Ag_2S , AgI , SiS_2 , and B_2S_3 were weighed in an oxygen- (<0.1 ppm) and water- (<0.1 ppm) free helium atmosphere glovebox and transferred to a vitreous carbon crucible. The crucible is covered with a vitreous carbon lid and placed in a tantalum holder that is part of a custom designed furnace and casting system, see Fig. (1-7). All samples were melted at a temperature of 850°C and allowed to soak for 10 minutes. The samples were allowed to cool in the crucible and were weighed to check for weight loss. All samples had weight loss of 1% or less. The samples were then returned to the furnace for an additional five minutes and then cast into a brass mold held at a temperature approximately 50°C below the glass transition temperature for the glass. The

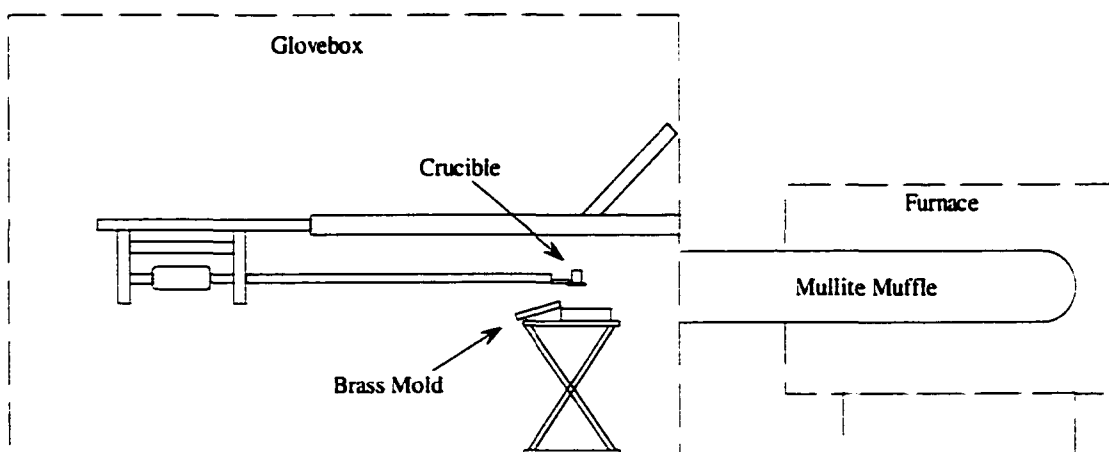


Figure (1-7). Schematic of furnace and casting system.

samples were allowed to soak in the mold for thirty minutes and then cooled at 5°C/min to room temperature. The purpose of the soak and slow cool is to allow the glass to anneal which reduces the residual stresses that are always present in cast glass.

1.4.2. Sample Characterization

Several techniques including scanning electron microscopy (SEM), x-ray diffraction (XRD), differential scanning calorimetry (DSC), density, infrared absorption spectroscopy (IR), Raman spectroscopy, neutron diffraction, nuclear magnetic resonance (NMR), and impedance spectroscopy (IS) and were used during this study.

1.4.2.1. Scanning Electron Microscopy

Scanning Electron Microscopy (SEM) is extremely useful in characterizing materials. By using a highly focused electron beam, surface features on the order of 4 nm can be distinguished. The instrument used for this study is a Hitachi S-2460N "Environmental" or "low-vacuum" SEM. It has a resolution of 4 nm allowing for magnifications of tens of thousands of times. Attached to this instrument is a Link Isis energy-dispersive x-ray system with a high-resolution, light-element Ge detector. This allowed for elemental characterization of the samples and the detection and characterization of impurity phases.

1.4.2.2.X-Ray Diffraction

X-Ray diffraction is based in upon the measurement of emission, absorption, scattering, fluorescence, and diffraction of electromagnetic energy¹⁷. X-Rays are short wavelength electromagnetic radiation, approximately 0.1 Å to 25 Å, produced by the deceleration of high-energy electrons or by electronic transitions involving electrons in the inner orbitals of atoms. Diffraction occurs as a result of radiation being scattered by a regular array of scattering centers whose spacing is approximately the same as the wavelength of the radiation. Interatomic distances are generally on the order of 1 Å which allows a atomic array to act as a diffraction grating for x-rays¹⁴. Since interatomic relationships are unique, if an exact x-ray diffraction match can be found between an unknown and an authentic sample, a chemical identity can be assumed.

In glassy materials where the atomic array is disordered, it is much more difficult to use XRD to identify an unknown. Instead of the very sharp peaks that are indicative of a crystalline structure, an amorphous structure produces broad humps that are related to the short-range order of the glassy material. The presence of these broad humps instead of the sharp peaks can be used to determine the crystallized fraction present in a sample.

X-Ray diffraction work was performed using a Scintag X-Ray Diffractometer with an excitement voltage of 45 kV and a Cu source. The samples were scanned using uncovered polycarbonate sample holders.

1.4.2.3. Differential Scanning Calorimetry

Differential scanning calorimetry (DSC) measures the temperatures and heat flows that are associated with transitions in materials as a function of time and temperature in a controlled atmosphere. The measurements provide quantitative and qualitative information about physical and chemical changes that involve endothermic or exothermic processes, or changes in heat capacity¹⁵.

DSC works by heating a sample and a known reference at the same heating rate and measuring the heat flow required to the sample to keep it at the same temperature as the reference. If the sample undergoes an exothermic transition, the heat flow needed to keep the sample at the same temperature as the reference is reduced. If the sample undergoes an endothermic transition, the heat flow needed to keep the sample at the same temperature as the reference is increased. Examples of these transitions would include glass transition, crystallization, and melting temperatures as well as thermal relaxation.

The differential scanning calorimeter used for this study is a Perkin-Elmer Pyris 1 DSC running Pyris software version 3.01. This DSC works under the power compensation temperature null principle. This means that the DSC has two separate furnaces, one for the sample and one for the reference, and measures the power supplied to each furnace to maintain the specified heating rate. It has a temperature range of -170 to 750°C and a sensitivity of 0.2 μ W. The calorimetry accuracy is $> \pm 1\%$ at a precision of $> \pm 0.1\%$. The temperature accuracy is $\pm 0.1^\circ\text{C}$ at a precision of $\pm 0.01^\circ\text{C}$.

The Pyris 1 DSC also has a new feature called Dynamic Differential Scanning Calorimetry, DDSC. This technique applies a sinusoidal (dynamic) rate of temperature

change. This greatly enhances the instruments sensitivity to weak transitions and allows for the resolution of transitions that occur close in temperature.

1.4.2.4. Density Measurements

Density measurements are used to help give a basic idea of the structure. When combined with the structure of the glass, density trends can be used to determine free space within a material. The method performed for this investigation used Archimedes' principle. Equation (1-24) gives the

$$\rho_s = \frac{\rho_k w_a}{w_a - w_m} \quad (1-24)$$

formula used to calculate the density of a sample where ρ_k is the density of the suspending liquid (kerosene), w_a is the weight of the sample in air, and w_m is the weight of the sample suspended in the liquid.

1.4.2.5. Infrared Absorption Spectroscopy

The infrared region of the electromagnetic spectrum covers from frequencies just below visible frequencies to just above the highest microwave and radar frequencies. Common infrared spectrometers operate in the middle of this region. from 2.5 μm to 25 μm . Although infrared photons do not have enough energy to cause electronic transition, they can cause groups of atoms to vibrate with respect to the bonds that connect them. Like electronic

transitions, these vibrational transitions correspond to distinct energies, and molecules absorb infrared radiation only at certain wavelengths and frequencies¹⁶. This allows for the unique identification and assignment of infrared absorption peaks.

The infrared spectrometer used for this investigation is a Bio-Rad FTS-40 Fourier Transform Infrared Spectrometer. It has a spectral range of 4400 to 450 cm^{-1} at a maximum resolution of 0.5 cm^{-1} .

1.4.2.6. Raman Spectroscopy

Raman spectroscopy is complementary to infrared spectroscopy in that they provide similar information. When radiation passes through a medium, the species present scatter a fraction of the radiation in all directions. The wavelength of a small fraction of the scattered radiation differs from that of the incident radiation and is shifted in wavelength in a manner that is dependent on the chemical structure of the molecules responsible for the scattering¹⁷. This allows for the unique identification and assignment of Raman scattering peaks

The instrument used for this study was a Brüker RFS 200/S FT-Raman Spectrometer. It uses an Nd:YAG Laser operating at 1064 nm as the excitation source. This instrument has a useful Stokes shift spectral range of 120 to 3600 cm^{-1} .

1.4.2.7. Neutron Diffraction

Neutron diffraction allows the user to probe the sample's structure from interatomic correlations to the intermediate range order on an intermediate length scale¹⁸. The instrument used for this study is located at the LAD (Liquid and Amorphous Diffractometer) at the ISIS

spallation source, Rutherford Appleton Laboratory, UK and were performed in collaboration with A. Matic, J. Swenson, and L. Börjesson from the Department of Applied Physics, Chalmers University of Technology, Göteborg, Sweden. The samples were in the form of fine powders placed in 8mm diameter thin-walled cylindrical vanadium cans. The time of flight spectra obtained in the 14 detectors (at 5°, 10°, 20°, 60°, 90°, and 150°) were individually corrected for background and container scattering, absorption, self shielding, and inelasticity effects and normalized to a vanadium standard to obtain the static structure factor $S(Q)$ following the procedure described by Howe *et al.*¹⁹

1.4.2.8. Nuclear Magnetic Resonance

The energy of a magnetic moment, μ , in a magnetic field, H_0 , is $-\mu H_0$ so that a positive moment will always want to line up parallel with the field. Such a moment that is already parallel to the field, in a lower energy state, can undergo a transition to a higher energy state by receiving an appropriate amount of energy.

Every nucleus has a spin; the number of discrete energy states is dependent on the individual spin of each nucleus. In the simplest case, a spin of $1/2$, there are two energy states: one aligned and one opposite to the applied field. The work required to reverse the orientation of the moment is equal to \hbar times the angular velocity of an applied rf field. The frequency of the rf irradiation needed to cause such a transition is equal to the Larmor velocity, ω_0 . If the frequency of the applied radiation is too low or too high, the nucleus will not undergo the transition. The environment of the nucleus acts to either shield or enhance

the magnetic field seen by the nucleus. This allows unique structural information about the sample to be determined.

A different type of NMR measurement can be performed called the Nuclear Spin Lattice Relaxation (NSLR) measurement. This gives a relaxation time that can be correlated to the ionic conductivity results as determined from impedance spectroscopy. It allows for the interpretation of a picture of the dynamics involved in ion hopping.

The instrumentation used for this study was used through collaboration with B. Meyer and F. Borsa at the Iowa State University Physics NMR Laboratory.

1.4.2.9. Impedance Spectroscopy

The determination of the d.c. conductivity of glass samples using d.c. techniques is inhibited by space charge polarization that is a result of the limited motion of the ions at the boundary of the glass. Application of a d.c. electric field results in the ions migrating towards and piling up at the electrode that is biased opposite to the charge of the ions. This polarization of the ions produces an electric field that is opposite to the applied electric field and acts to reduce further ionic conduction as well as reducing the possibility of measuring the true ionic conductivity. By applying an a.c. electric field at frequencies that are greater than the inverse of the relaxation time of the space charge polarization process reduces the magnitude of this effect and allows the true conductivity of the glass to be accurately determined¹².

Impedance spectroscopy involves the application of an a.c. voltage to a sample over a range of frequencies and then measuring the resulting current that is produced and the phase difference between the current and the voltage signals.

The impedance spectrometer used for this investigation was a Solartron 1260 Impedance/Gain Phase Analyzer. It has a measurable frequency range of 10 μ Hz to 32 MHz at a resolution of 1 in 65 million (0.015 ppm). It can measure impedances from 10 mohm to greater than 100 Mohm, and can create polarization voltages up to ± 40.95 volts.

A new sample cell holder was needed to interface between the sample and the Solartron. The holder needed to have very good electrical characteristics, such as minimal resistance and stray capacitance, -190°C to 500°C controlled temperature range, hands free operation over the entire temperature range, the ability to scan from -190°C to 500°C in one step, and the ability to handle air sensitive samples. Figures (4-2) and ((4-3) are schematic drawings of the new cell. The cell works by passing nitrogen gas through liquid nitrogen cooled copper coils, through a process tube heater, then finally into the sample compartment. The gas is then re-circulated back into the cold copper coils. The sample temperature is controlled by controlling the duty cycle of the tube furnace; the higher the duty cycle the higher the sample temperature. Nitrogen flow rate of 12 L/min is necessary to obtain stable temperature control within the desired temperature range of -190°C to 500°C.

The impedance spectrometer is computer controlled using software that was jointly developed by the Hahn-Tel Company and the author. This software controls all functions of the impedance spectrometer as well as the temperature control of the sample cell.

The raw data gathered from the impedance experiment must be transformed in order to determine the dc conductivity. Equation (1-25) can be used to determine the real

conductivity where k_o is the cell constant defined as the thickness of the sample divided by the area of the electrode. This can then be plotted as shown in Fig. (4-4) as a function of

$$\sigma' = \frac{k_o}{|Z|} \cdot \cos(-\theta) \quad (1-25)$$

frequency and temperature. This shows the frequency dependence of the conductivity and how it changes as temperature is increased. The large frequency independent region where the conductivity is constant is known as the “dc plateau” and can be used to determine the dc conductivity. An alternate and more precise method is to use an impedance plane plot. This is constructed by plotting the imaginary impedance (Z'') versus the real impedance (Z') and an example is shown in Fig. (4-5). The real impedance is calculated using Eq. (1-26) and the imaginary impedance is calculated using Eq. (1-27). The arc at high frequency represents the

$$Z' = |Z| \cdot \cos(\theta) \quad (1-26)$$

$$Z'' = |Z| \cdot \sin(\theta) \quad (1-27)$$

bulk response of the glass to an applied ac electric field, by determining where the arc intersects with the Z' axis the dc conductivity is determined²⁰.

1.5. References

- ¹ Tuller, H., Barsoum, M., *J. Non-Crystalline Solids*, **73**, 331-350 (1985)
- ² Fusco, F. A., Tuller, H. L., *Fast Ion Transport in Glasses*; p. 43: Superionic Solids and Solid Electrolytes; Academic press, (1989)
- ³ Kinss, J., Martin, S. W., *Phys. Rev. Let.*, **76**, 70-73 (1996)
- ⁴ Martin, S.W., Bloyer, D.R., *J. Am. Ceram. Soc.*, **73**(11), 3481-5 (1990)
- ⁵ Varshneya, A.K., Fundamentals of Inorganic Glasses, Academic Press, Inc. 1994
- ⁶ Zachariasen, W.H., *J. Chem. Soc.*, **54**, 3841-3851 (1932)
- ⁷ Porter, D.A., Phase Transformations in Metals and Alloys, Van Nostrand Reinhold (UK) Co. (1981)
- ⁸ Anderson, O. L., Stuart, D. A., *J. Am. Ceram. Soc.*, **37**, 573-580 (1954)
- ⁹ McElfresh, D. K., Howitt, D. G., *J. Am. Ceram. Soc.*, **69**, C-237-C-238 (1986)
- ¹⁰ Macdonald, J. R., *J. Appl. Phys.*, **84**, 812-827 (1998)
- ¹¹ Ngai, K. L., Rzos, A. K., *Phys. Rev. Let.*, **76**, 1296-1299 (1996)
- ¹² Kinss, J., Masters Thesis, Iowa State University (1994)
- ¹³ Martin, S.W., Bloyer, D., *J. Am. Ceram. Soc.*, **74**, 1003 (1991)
- ¹⁴ Shackelford, J.F., Introduction to Materials Science for Engineers, 4th ed., Prentice Hall. (1996)
- ¹⁵ Seminar and training course offered by TA Instruments (1999)
- ¹⁶ Wade, L.G. Jr., Organic Chemistry, 2nd Ed., Prentice Hall (1991)
- ¹⁷ Skoog, D.A., Leary, J.J., Principles of Instrumental Analysis, 4th ed., Saunders College Publishing, 1992
- ¹⁸ Matic, A., Swenson, J., Börjesson, L., Akai, T., Schrooten, J., Martin, S.W., to be published
- ¹⁹ Howe, M, Howells, W.S., McGreevy, R.L., *J. Phys.: Cond. Mat.*, **1** 3343 (1989)
- ²⁰ Mcdonald, J.R., Impedance Spectroscopy: Emphasizing Solid Materials and Systems, John Wiley & Sons (1987)

2. Preparation and Characterization of Boron Oxysulfide Glasses

By

J. Schrooten^{1,2}, B. Meyer^{2,3}, S. W. Martin^{2,4}, F. Borsa³

A paper submitted to the Journal of Non-Crystalline Solids, November 2001

2.1. Abstract

Stable, homogeneous $x \text{B}_2\text{O}_3 + (1-x) \text{B}_2\text{S}_3$ glasses were prepared between $0 \leq x \leq 0.80$ and at $x = 1.0$. It was not possible to prepare homogeneous, stable glasses of compositions $0.85 \leq x \leq 0.95$ due to a strong exothermic enthalpy of mixing between the B_2S_3 and B_2O_3 phases. Raman spectroscopy and ^{11}B NMR were used to characterize the structure of the glasses and to show that the peak intensities for the oxide structures, particularly those of the six-membered rings, quickly diminish with increasing sulfide content whereas the peaks for the sulfide structures remain relatively intense as the oxide content is increased. Differential scanning calorimetry (DSC) and density measurements were used to characterize the physical properties of the glasses and show that the physical properties of these mixed boron oxysulfides heavily favor the B_2S_3 properties regardless of the amount of B_2O_3 added to the system. This is possibly due to the high robustness of the B_2S_3 thioboroxol ring structure which remains relatively untouched in the glass network

¹ Primary researcher and author

² Department of Materials Science & Engineering, Iowa State University, Ames, IA 50011

³ Ames Laboratory – U.S. Department of Energy, Iowa State University, Ames, IA 50011

⁴ Author to whom correspondence should be directed

through compositions of $x = 0.6$. A structural model is proposed where the cause for the large heat of mixing is associated with the formation of new mixed boron oxysulfide structures of composition BS_iO_{3-i} where $0 < i < 3$. The characterization methods used support this model.

2.2. Introduction

Boron oxysulfide glasses are prepared from any combination of thioborate (B_2S_3) and borate (B_2O_3) glasses. Borate and thioborate glasses have been extensively studied and characterized as separate materials; see for example ref. ²¹ and ²². B_2S_3 -based glasses have been shown to exhibit fast ionic conductivity, an important property for use as an electrolyte in batteries or fuel cells^{23,24}. While most B_2S_3 -based glasses are known to be highly reactive with water and oxygen²⁵ it has been shown that the addition of other materials can stabilize the resulting glass²³. In contrast to the thioborates, the stability of many borate glasses has been well documented²⁶; however, their conductivity is quite low²⁷. The combination of sulfide and oxide glasses into boron oxysulfide glasses hold potential as chemically durable fast ion conducting (FIC) glasses for use in fuel cells and solid-state batteries. The addition of B_2O_3 to B_2S_3 may allow for a glass composition that is both stable in air and water as well as exhibiting fast ionic conduction.

Oxysulfides are not unique to boron systems. The concept of oxysulfide materials is well known and extensively studied where examples include $MoS_{2-x}O_x$, V_2O_4S , and $TiO_{0.3}S_{1.5}$.^{28,29,30}

Another motivation for this study is that during preparation sulfide glasses are often contaminated with oxygen³¹. The physical property effect that this oxide contamination has on bulk thioborate glasses was previously unknown. This study has allowed for the investigation of the relative effect of the sulfur for oxide substitution upon the physical properties of these glasses. This study shows that the physical properties of the material are mostly dominated by the sulfide material and show little dependence on oxygen concentration.

Boron trioxide and boron trisulfide glasses are found to be isostructural, excepting bond distance differences³². The base unit is a trigonal boron unit that is independent, loose, or arranged into six-membered ring structures^{33,33,34,35}. In B_2O_3 , the rings are known as boroxol rings and in B_2S_3 , the rings are known as thioboroxol rings. In pure B_2S_3 and B_2O_3 , 25% of the boron atoms are found in trigonal units and 75% of the boron is found in six-membered rings. This results in an equal number of six-membered rings and trigonal units.

The combination of B_2S_3 and B_2O_3 into an oxysulfide glass may cause a sulfur for oxygen substitution resulting in new structural units of the form of BS_iO_{3-i} . A hypothesis is presented that suggests that thioboroxol rings have an inherent chemical stability in the presence of added B_2O_3 over that of the loose trigonal units. For this reason, it is thought that the oxygen first substitutes for the sulfur in the loose triangles breaking up the oxide network, and allowing the sulfide network to endure to high oxygen concentrations.

2.3. Preparation

B_2S_3 was prepared through the reaction of stoichiometric amounts of amorphous boron (Cerac, 99.9+%) and sulfur (Cerac, 99.999%) powders. This investigation used a modified version of the method reported by Martin and Bloyer³⁶. The modified version increased the size of the batch from 3 grams to 40 grams by using a larger quartz ampoule that could hold more starting material. The interior of a large quartz ampoule (~500 ml) was coated with pyrolytic carbon through the anaerobic decomposition of acetone. The appropriate amounts of boron and sulfur powders were placed inside of the ampoule that was then evacuated and sealed. The ampoule was then heated slowly to 850°C for eight hours and air cooled to room temperature.

The B_2O_3 that was used for the boron oxysulfide preparation was prepared through the decomposition of boric acid according to the reaction:



Boric acid was placed into an alumina crucible, heated at 850°C for 1 hour, and then allowed to air quench. The temperature at which water is released from B_2O_3 is 300°C³⁷ and was confirmed by the NMR results that all residual H_2O had been released from the H_3BO_3 due to the lack of tetrahedral boron resonance. The B_2O_3 was then immediately placed into a water- and oxygen-free glovebox. There was no evidence of crucible attack by the boric acid.

The boron oxysulfide samples were prepared inside a water- and oxygen-free (<2 ppm H_2O , O_2) glovebox. They were heated to 900°C in a vitreous carbon crucible in a box furnace for 20 minutes after which the crucible was removed from the furnace and allowed to air cool to room temperature in the glovebox. Samples of $0 \leq x \leq 0.80$, and $x = 1$ where x is

mole fraction B_2O_3 were all glass forming by allowing the glass melt to air quench to room temperature in the crucible. The glasses were generally a dark brown color and had a viscosity similar to maple syrup (~ 0.15 Pa·s) when heated to 900°C . For values of x between 0.85 and 0.95, the melts appeared to “explode” completely coating the interior of the box furnace.

2.4. Experimental Techniques

2.4.1. Raman Spectroscopy

Raman spectroscopy was performed using Brüker RFS-200/S FT-Raman Spectrometer. It uses an Nd:YAG Laser operating at 1064 nm as the excitation source. This instrument has a useful Stokes shift spectral range of 120 to 3600 cm^{-1} . Powder samples weighing less than 10 mg were used in a 180° backscatter experiment at powers of typically <100 mW to collect the Raman spectra.

2.4.2. Differential Scanning Calorimetry

Glass transition temperature measurements were performed using a Perkin-Elmer Pyris 1 DSC running Pyris software version 3.01. It has a temperature range of $-170 - 750^\circ\text{C}$ and a sensitivity of $\pm 0.2\ \mu\text{W}$. The calorimetry accuracy is $> \pm 1\%$ at a precision of $> \pm 0.1\%$. The temperature accuracy is $\pm 0.1^\circ\text{C}$ at a precision of $\pm 0.01^\circ\text{C}$. All calorimetric measurements were performed by initially heating the sample above the glass transition temperature ($\sim 300^\circ\text{C}$), cooling at $10^\circ\text{C}/\text{min}$ to 100°C , then reheating at $10^\circ\text{C}/\text{min}$. This was

done to ensure all samples had a comparable thermal history. All thermal measurements were determined by measuring the onset temperature of the thermal event. Typical sample sizes were 30 mg and were hermetically sealed into aluminum sample pans.

The Pyris 1 DSC has an advanced feature called Dynamic Differential Scanning Calorimetry, DDSC. This technique applies a sinusoidal (dynamic) rate of temperature change as compared to the linear temperature change used in traditional DSC. A typical method for DDSC would be to heat the sample at 50°C/min for 5 degrees then cool at 5°C/min for 4 degrees. This greatly enhances the instruments sensitivity to weak transitions and allows for the resolution of transitions that occur close in temperature. The drawback is that DDSC scans have a very slow overall heating rate, which greatly increases the time necessary to perform calorimetric measurements, but the increased resolution may be worth the effort. This technique was used in the current investigation where many of the transitions had very small ΔC_p values.

2.4.3. Density Measurements

Density measurements were performed using Archimedes' method inside the water- and oxygen-free glovebox using kerosene as the suspending liquid³⁸. These measurements are accurate to ± 0.01 g/cc.

2.4.4. Nuclear Magnetic Resonance

^{11}B static and Magic Angle Spinning (MAS) NMR experiments were performed at 4.7 Telsa (64.179 MHz) to yield structural information about the $x \text{B}_2\text{O}_3 + (1-x) \text{B}_2\text{S}_3$ glass forming series. The effective $\pi/2$ pulse length was determined to be $3.0 \mu\text{s}$ using HBO_3 saturated in H_2O as a reference. Since ^{11}B is a quadrupolar nucleus with spin $I=3/2$, a shorter pulse length ($\pi/8$) was used in order to avoid non-central line transitions. A spinning speed of 9.0 KHz in the MAS experiments was sufficient to separate out the spinning sidebands from the spectra. In both the static and MAS experiments the data was acquired from the FID directly following a single pulse with five seconds delay between scans.

2.5. Results

Figure (2-1) shows the Raman spectra for the boron oxysulfide glasses. Royle et al.³⁵ has identified and assigned the peaks in the B_2S_3 spectrum. The broad, asymmetric peaks at 1042 and 919 cm^{-1} arise from six-membered rings in B_2S_3 and the symmetric peaks at 498 and 439 cm^{-1} are also assigned to six-membered rings. The peaks at 388 and 771 cm^{-1} are assigned to trigonal BS_3 units.

Several investigators have identified and assigned the peaks in Raman spectra of B_2O_3 ^{39,40}. The weak peaks at 471 and 599 cm^{-1} and the very strong peak at 808 cm^{-1} are all assigned to six-membered ring units. The remaining weak peak at 664 cm^{-1} is assigned to loose trigonal units.

As B_2O_3 is added to B_2S_3 , the trigonal B_2S_3 peak at 771 cm^{-1} decreases in intensity and two new peaks grow in at 533 and 637 cm^{-1} . These peaks are tentatively assigned as B_2S_2O at 533 cm^{-1} and B_2SO_2 at 637 cm^{-1} . This assignment is made by considering that the increased mass of the sulfur atom results in a lower vibrational frequency causing the sulfur rich unit to appear in the Raman spectra at lower wavenumbers. Table (2-1) summarizes the peak assignments. Notice that in the table, certain peaks listed as not present for the $x = 0.5$ glass maybe present for other compositions. For example, the peak at 771 cm^{-1} is listed as high intensity for B_2S_3 and systematically decreases until there is no evidence of it in the $x = 0.5$ sample.

Figure (2-2) shows a DDSC scan of one of the compositions. Due to the extremely sensitive nature of DDSC, very small thermal events can be resolved. Since the B_2S_3 and B_2O_3 glass transition temperatures differ by 40°C , it would be expected that if the samples were phase separated into two separate regions that the presence of two distinct T_g signatures would be present. Since only one transition is seen, it is probable that the samples are homogeneous.

Figures (2-3) and (2-4) show the density and T_g trends for the glasses. Notice that there is very little dependence on the presence of B_2O_3 . The properties definitely appear to favor the B_2S_3 values.

In the density data, there may be a shallow, broad minimum centered on $x = 0.5$ which only amounts to a density difference of 0.1 g/cc . For the glass transition data, the T_g slowly decreases by 20°C at $x = 0.3$ and then slowly increases again by 20°C at $x = 0.7$.

The ^{11}B NMR static spectra of pure glassy B_2S_3 and pure B_2O_3 are shown in Fig. (2-5). Due to the large dipolar broadening, the static spectra shown in Fig. (2-6) did not yield any significant information about the structure of the oxythioborate glasses over the entire $x \text{B}_2\text{O}_3 + (1-x) \text{B}_2\text{S}_3$ compositional range. Since the chemical shift values were masked by the dipolar broadening, the static spectra were ambiguous in determining whether the glass structure was comprised of a simple combination of pure B_2O_3 and B_2S_3 trigonal units or of additional new trigonal structures such as $\text{B}_2\text{O}_1\text{S}_2$ and $\text{B}_2\text{O}_2\text{S}_1$.

For this reason, MAS NMR experiments were used to remove the dipolar effects to reveal the structural characteristics of the glasses. Figure (2-7) shows the ^{11}B MAS spectra for both pure glassy B_2O_3 and B_2S_3 . In both cases, the quadrupolar split line shape is characteristic of ^{11}B in trigonal coordination⁴¹. The double peak arises from quadrupolar splitting of the central line transition when ^{11}B is in the trigonal coordination as isolated triangles and as boroxol rings. Thus, on the short-range order, pure B_2O_3 is comprised of BO_3 units and pure B_2S_3 is comprised of BS_3 units as expected.

If the B_2O_3 and B_2S_3 components were to separate into separate phases, it would be expected to see NMR spectra that would resemble the addition of the pure B_2S_3 and pure B_2O_3 spectra in corresponding ratios. However, Fig. (2-8) shows that four new peaks appear for the $x \text{B}_2\text{O}_3 + (1-x) \text{B}_2\text{S}_3$ glasses. Due to the lack of alkali modifier in these borate and thioborate glasses, it is unlikely that the new sites would be tetrahedral boron³⁸. This suggests two new trigonal boron units (each trigonal site accounts for two peaks), BOS_2 and BO_2S .

S. J. Hwang³¹ performed ^{11}B MAS experiments to determine the oxide contamination found in pure $\nu\text{-B}_2\text{S}_3$. It was found that the oxygen contamination appeared in the form of BOS_2 and BO_2S units. Table (2-2) shows the isotropic chemical shift values for these structural units. This allows for the assignment of P1 to the BOS_2 unit and P2 to the BO_2S unit. Analyzing the quadrupolar splitting width of all the possible peak combinations suggests that P1 and P3 belong to BOS_2 and likewise P2 and P4 belong to the BO_2S unit. Table (2-3). Any other combination yields values that differ significantly from the splitting width of 2.659 kHz and 2.842 kHz for pure B_2S_3 and pure B_2O_3 , respectively.

2.6. Discussion

Homogeneous mixed boron oxysulfide glasses were prepared over the ranges of $0 \leq x \leq 0.8$ and $x = 1$ where x is the mol fraction of B_2O_3 . For the compositions where $x = 0.85$, 0.90, and 0.95 the samples were not glass forming. By simple observation of the condition of the furnace, it was obvious that an extremely exothermic event had occurred causing the sample to boil and splatter, completely coating the inside of the furnace. Perhaps there is a strong enthalpy of mixing between B_2S_3 and B_2O_3 and is released upon the formation of the proposed structural groups $\text{B}_2\text{S}_2\text{O}$ and B_2SO_2 , this is discussed in detail below.

DSC and density measurements show that the physical properties of these mixed boron oxysulfides favor the B_2S_3 properties regardless of the amount of B_2O_3 added to the system. The NMR and Raman results show that the peak intensities for the oxide structures, particularly the six-membered rings, quickly diminish with increasing sulfide content, whereas the peaks for the sulfide structures remain relatively intense as the oxide content is

increased. It appears that the six-membered rings of the oxide structure (boroxol rings) are broken up first by the sulfur atoms but that the loose trigonal units in B_2S_3 are the ones first targeted by oxygen atoms. Comparing these observations leads to the conclusion that the B_2S_3 six-membered ring (thioboroxol ring) is more chemically robust to increasing oxygen impurities than the boroxol ring is to increasing sulfide impurities.

Assuming that one sulfur atom will destroy one boroxol ring, then the addition of 14.3% B_2S_3 to B_2O_3 would destroy all of the boroxol rings. Glass samples of 0-15% B_2S_3 could not be made due to the exothermic nature of the glass melt. Perhaps the destruction of the boroxol rings is an exothermic event that releases a sufficient amount of energy to boil the glass melt. The addition of 20% B_2S_3 may add sufficient mass to the melt to adequately absorb the exothermic heat without boiling, explaining the behavior seen in compositions of less than 20% B_2S_3 .

A possible explanation to the increased robustness of the thioboroxol rings may be a sort of pi-orbital stabilization by the sulfur atoms. Since sulfur is a larger atom with more electrons than oxygen, perhaps there is sufficient overlap of the pi-orbitals of the sulfur and boron in the 6-membered ring to allow for stabilization. A similar effect is seen in alkali thioborates²² where the alkali ion attacks the loose trigonal units of the thioborate before the six-membered rings are attacked.

A second possible explanation for the robustness thioboroxol rings may be due to the deformation ability of a thioboroxol ring compared to that of a boroxol ring. Perhaps a thioboroxol ring can accept the strain induced when one of the sulfur atoms is replaced with an oxygen atom. If this were the case, it would be expected that there would be a shift in the

Raman spectra for the thioboroxol rings. Since this shift is not observed, this hypothesis is unlikely.

The density and T_g trends may also be explained by the robustness of the thioboroxol rings. The density of a thioboroxol ring is going to be less than the density of three trigonal units due to the open structure of a ring. Since 75% of the boron atoms are in thioboroxol rings, the density of pure B_2S_3 should be determined primarily by the density of the thioboroxol ring. If the trigonal units are the structures that the oxygen first reacts with, then the density of the oxysulfide glass would favor the density of pure B_2S_3 . The same should be true for the glass transition trend. This investigation is proposing that the thioboroxol rings are the more stable part of the B_2S_3 network and as such would determine the glass transition temperature of the glass. This improved stability of the thioboroxol ring would be the reason for the higher glass transition temperature compared to B_2O_3 . Since these structures are the last targeted by the oxygen, then the glass transition temperature of the oxysulfide glass should be similar to that of B_2S_3 .

2.7. Conclusions

Glasses in the $x B_2O_3 + (1-x) B_2S_3$ (boron oxysulfide) system were prepared and characterized for the first time. Homogeneous glasses could be prepared for $0 < x < 0.8$ where the compositions are strongly glass forming. The density and glass transition temperatures were measured and found to vary little with composition; and is attributed to the robustness of B_2S_3 six-membered rings. Unexpected behavior is observed for compositions of $0.8 < x < 0.95$ where the samples appear to exhibit a strong exothermic

reaction on mixing. The cause for the extra heat of mixing is associated with the formation of new mixed boron oxysulfide structures, which is supported by observed new spectral features in the Raman and NMR spectra of these glasses.

2.8. Acknowledgements

Special thanks goes to Chad Martindale and Michael Royle for their assistance in preparation and characterization of the glasses in this study. This work supported in part by NSF-DMR 00-1766

2.9. References

-
- ²¹ Feller, S., *Phys. Chem. Glasses*, **41**(5), 211-215 (2000)
- ²² Cho, J., Masters Thesis, Iowa State University (1992)
- ²³ Kinoss, J., Martin, S.W., *Phys. Rev. Lett.*, **76**, 70-73 (1996)
- ²⁴ Schrooten, J. Meyer, B., Martin, S.W., to be published
- ²⁵ Bloyer, D., Masters Thesis, Iowa State University (1989)
- ²⁶ Gol'dshtein, L. M. Orenbakh, M. S. Gorpinenko, M. S., *Izv. Akad. Nauk SSSR, Neorg. Mater.*, **16**(11), 1975-7 (1980)
- ²⁷ Martin, S.W., *J. Am. Ceram. Soc.*, **71**(6), 438-45 (1988)
- ²⁸ Meunier, G., Dormoy, R., Levasseur, A., *Thin Solid Films*, **205**, 213-217 (1991)
- ²⁹ Lince, J., *J. Mater. Res.*, **5**(1), 218-222 (1990)
- ³⁰ Tchangbedji, G., Prouzet, E., Ouvrard, G., *Materials Science Forum* Vols. 152-153, 319-322 (1994)
- ³¹ Hwang, S. J., Fernandez, C. *Solid State Nucl. Magn. Reson.*, **8**(2), 109-121 (1997)
- ³² Royle, M., Cho, J., Martin, S.W., *J. Non-Cryst. Sol.*, in press
- ³³ Royle, M., Martin, S.W., Write, A.C., Sinclair, R.N., *J. Non-Cryst. Sol.*, in press
- ³⁴ Zarzycki, J. *Glasses and the Vitreous State*, Cambridge University Press (1991)
- ³⁵ Royle, M., Cho, J., Martin, S. W. *J. Non-Cryst. Solids*, **279**(2-3), 97-109 (2001)
- ³⁶ Martin, S. W., Bloyer, D., *J. Am. Ceram. Soc.*, **74**, 1003 (1991)
- ³⁷ CRC Handbook of Chemistry and Physics., **72**, (1992)
- ³⁸ Varshneya, A., *Fundamentals of Inorganic Glasses*, Academic Press, Inc. (1994)
- ³⁹ Windisch, C.F., Risen, W.M., *J. Non-Cryst. Solids*, **48**, 307-323 (1982)
- ⁴⁰ Galeener, F.L., Lucovsky, G., Mikkelsen, J.C., *Phys. Rev. B*, **22**(8), 3983-3990 (1980)
- ⁴¹ Sills, J.A., Martin, S.W., *J. Non-Cryst. Solids*, **175**(2,3), 270-7 (1994)
- ⁴² H. Norh and B. Wrackmeyer, Nuclear Magnetic Resonance Spectroscopy of Boron Compounds, in P. Diehl, E. Fluck and R. Kosfeld(Eds.), NMR Basic Principles and Progress, Vol 14, Springer-Verlag, Berlin (1978)

2.10. Captions

Table (2-1). Raman peak assignments for B_2S_3 , B_2O_3 , and $x = 0.5$.

Table (2-2). Isotropic Chemical shift (ppm) values for trigonal boron units.

Table (2-3). Comparison of possible quadrupolar splitting values.

Figure (2-1). Raman spectroscopy of the boron oxysulfides. The bottom trace is pure B_2S_3 and the top trace is pure B_2O_3 . The remaining traces increment by 10 mole percent, omitting the 90 mole percent B_2O_3 composition.

Figure (2-2). Example of a DDSC scan on $0.35 B_2O_3 + 0.65 B_2S_3$. This data supports the conclusion that the sample is not phase separated as only one glass transition temperature can be seen.

Figure (2-3). Density measurements for the boron oxysulfides.

Figure (2-4). Glass transition data for the boron oxysulfides.

Figure (2-5). ^{11}B NMR static spectra at 4.7 Tesla of pure glassy B_2O_3 and pure glassy B_2S_3

Figure (2-6). ^{11}B NMR static spectra at 4.7 Tesla of $50\%B_2O_3 + 50\%B_2S_3$ glass.

Figure (2-7). ^{11}B MAS NMR at 4.7 Tesla of $x B_2O_3 + (1-x) B_2S_3$ glasses.

Figure (2-8). ^{11}B MAS NMR spectra showing the presence of four new peaks, P1 – P4.

Table (2-1)

Wavenumber	Intensity	Assignment	Peaks present for $x=0.5$
321	Med.	6-membered ring B_2S_3	318
388	Med.	Trigonal units B_2S_3	Not present
439	Med.	6-membered ring B_2S_3	442
471	Low	6-membered ring B_2O_3	Not present
498	Med.	6-membered ring B_2S_3	506
533	Med	Proposed 6-membered ring $B_2O_1S_2$	533
599	Low	6-membered ring B_2O_3	Not present
637	Low	Proposed 6-membered ring $B_2O_2S_1$	637
664	Low	Trigonal units B_2O_3	Not present
771	High	Trigonal units B_2S_3	Not present
808	High	6-membered ring B_2O_3	811
919	Med.	6-membered ring B_2S_3	Not present
1042	Med.	6-membered ring B_2S_3	Not present

Table (2-2)

Structural Unit	$x \text{ B}_2\text{O}_3 + (1-x) \text{ B}_2\text{S}_3$ glass	Literature reference
BS_3	63	63.6^{42}
BOS_2	48	45.8^{42}
BO_2S	31	30.3^{42}
BO_3	17	17.4^{31}

Table (2-3)

Combination	Pair 1	Width (KHz)	Pair 2	Width (KHz)
1	P1 & P2	1.054	P3 & P4	1.131
2	P1 & P4	3.850	P2 & P3	1.680
3	P1 & P3	2.735	P2 & P4	2.814

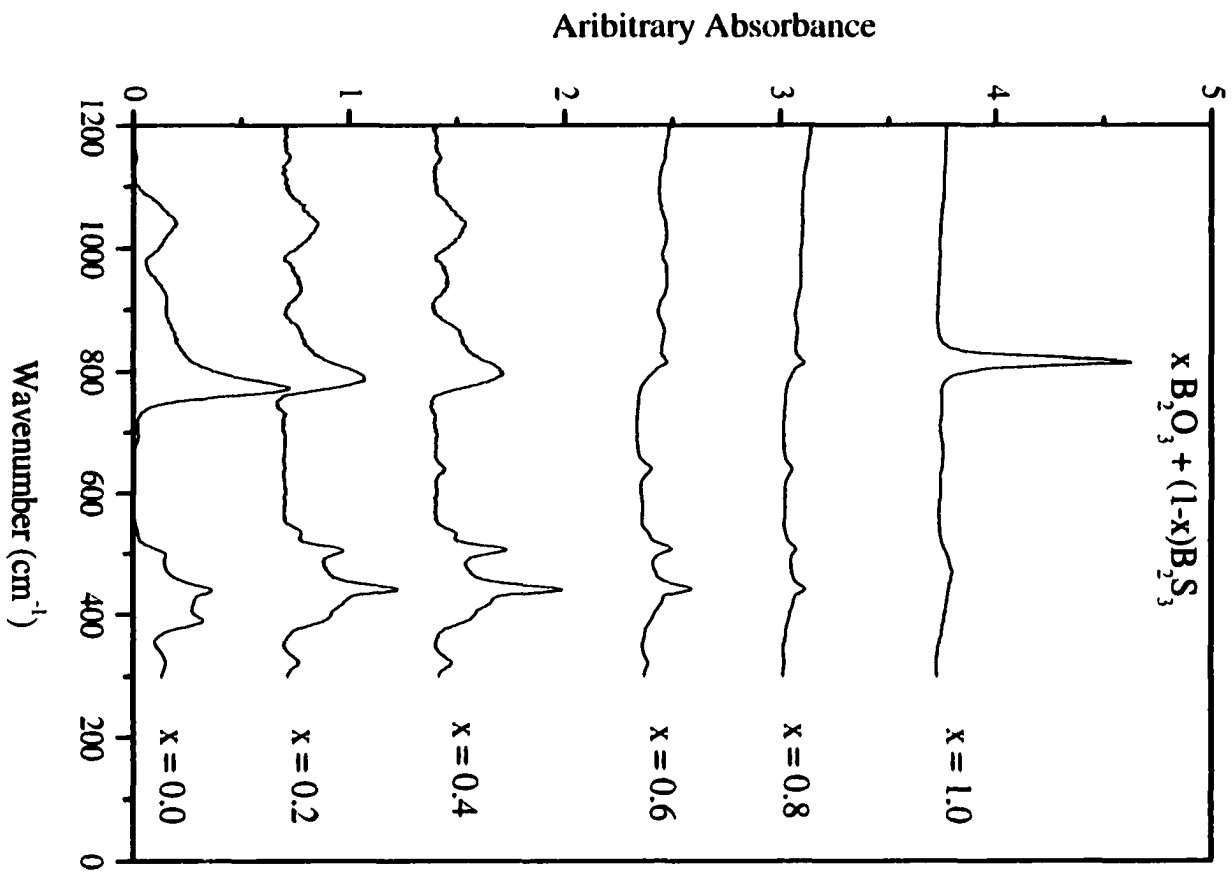


Figure (2-1)

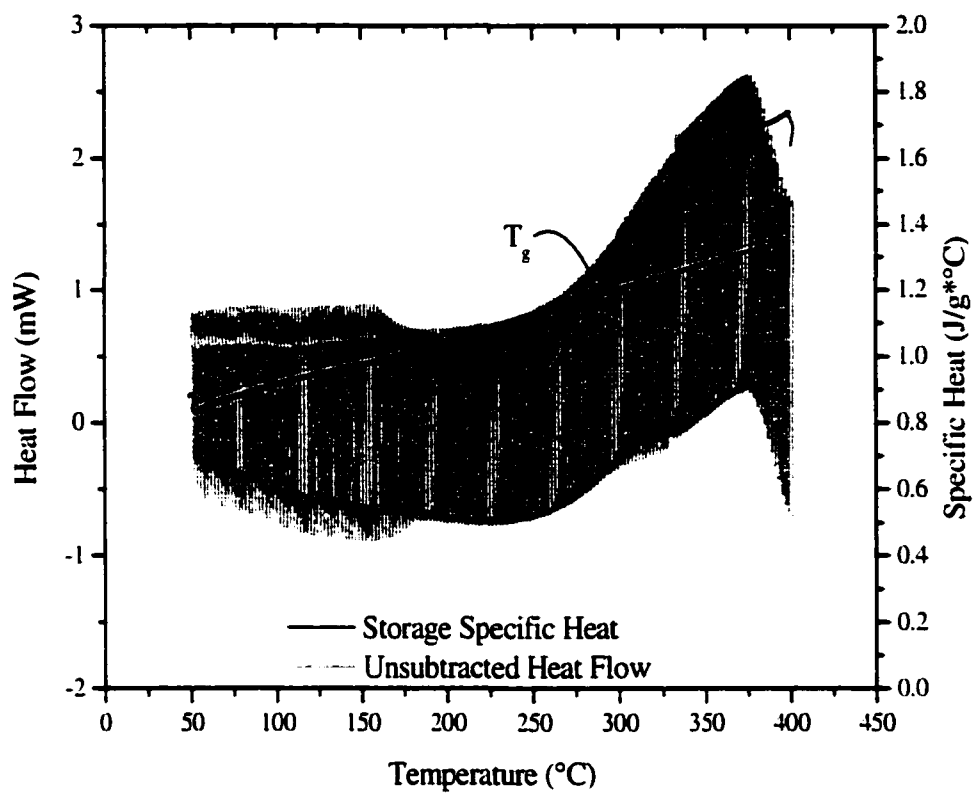


Figure (2-2)

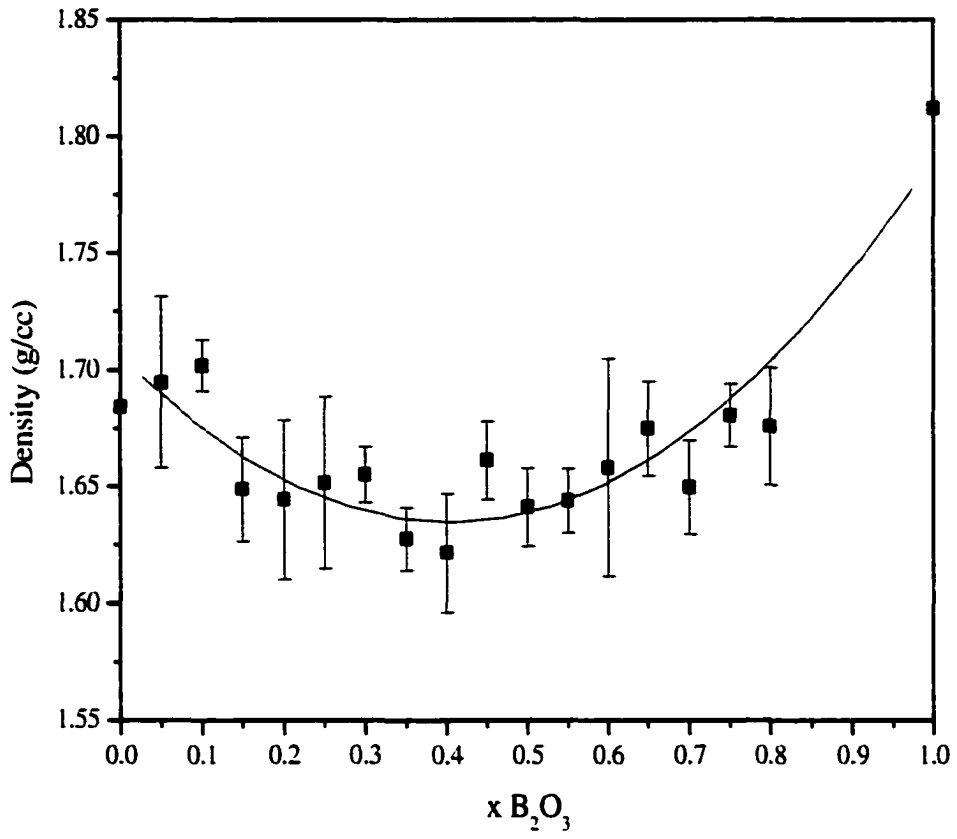


Figure (2-3)

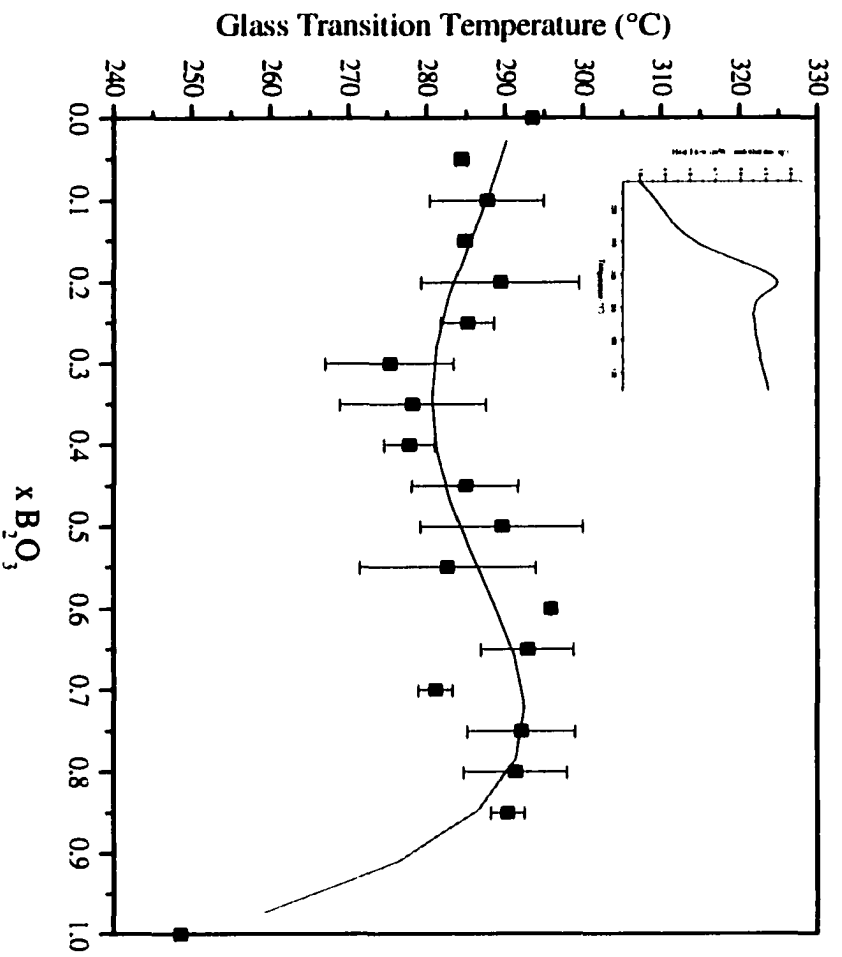


Figure (2-4)

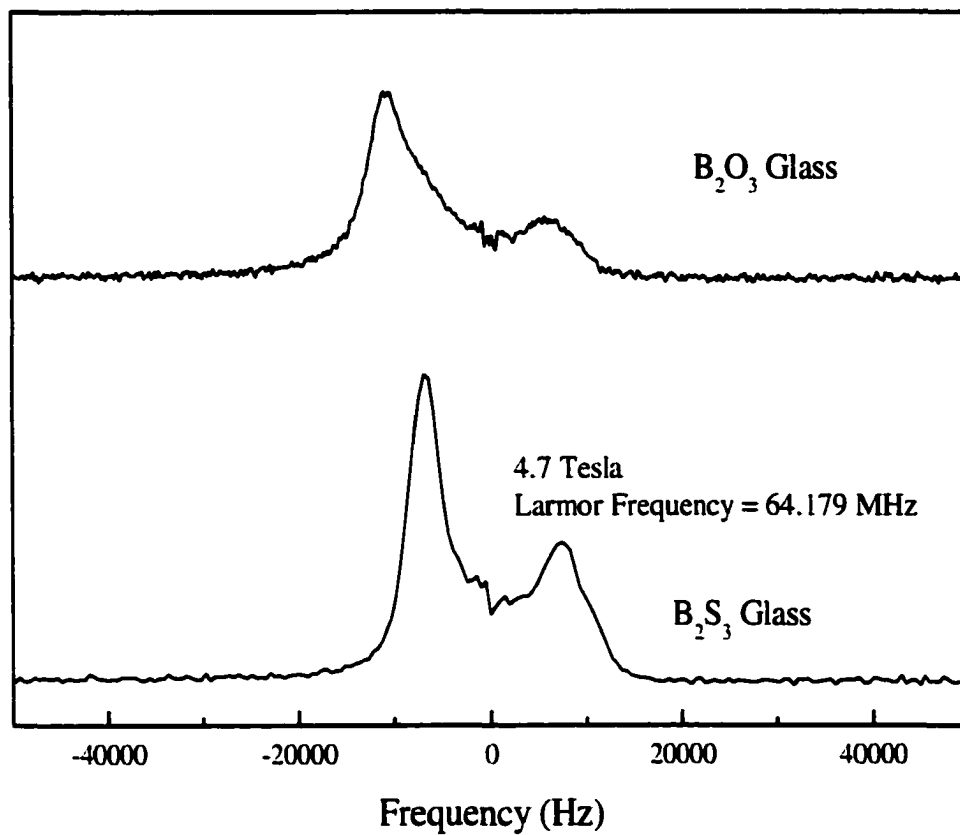


Figure (2-5)

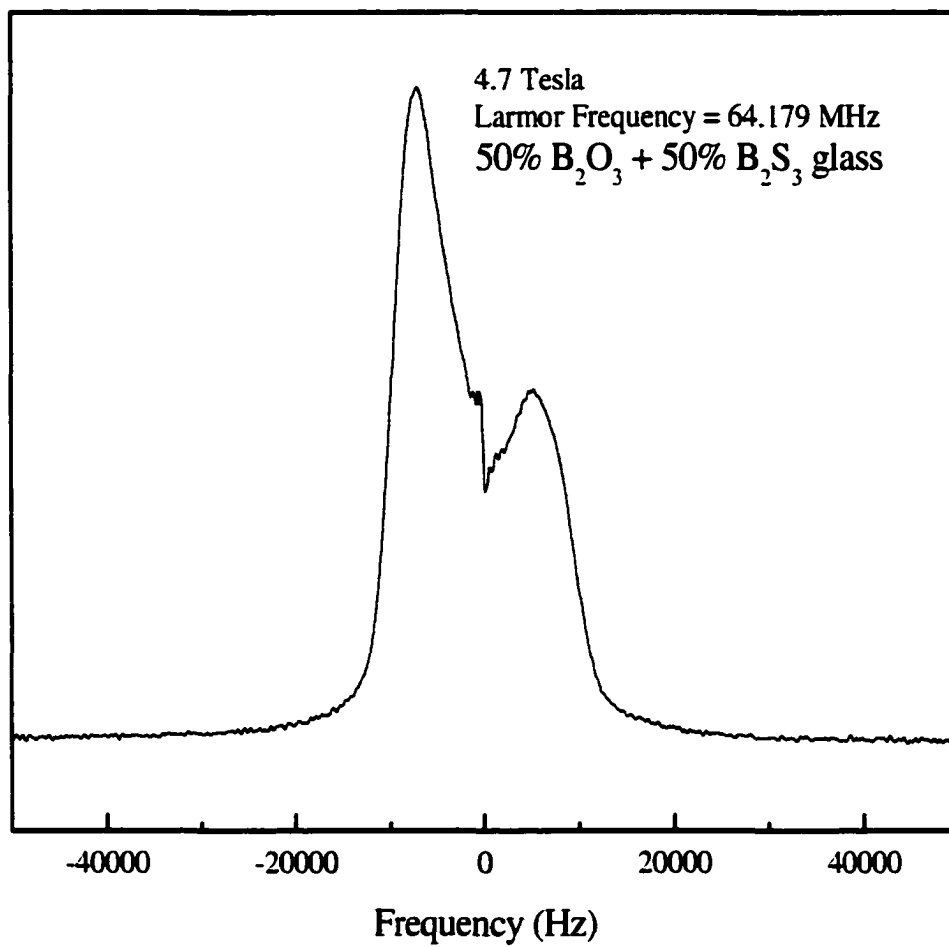


Figure (2-6)

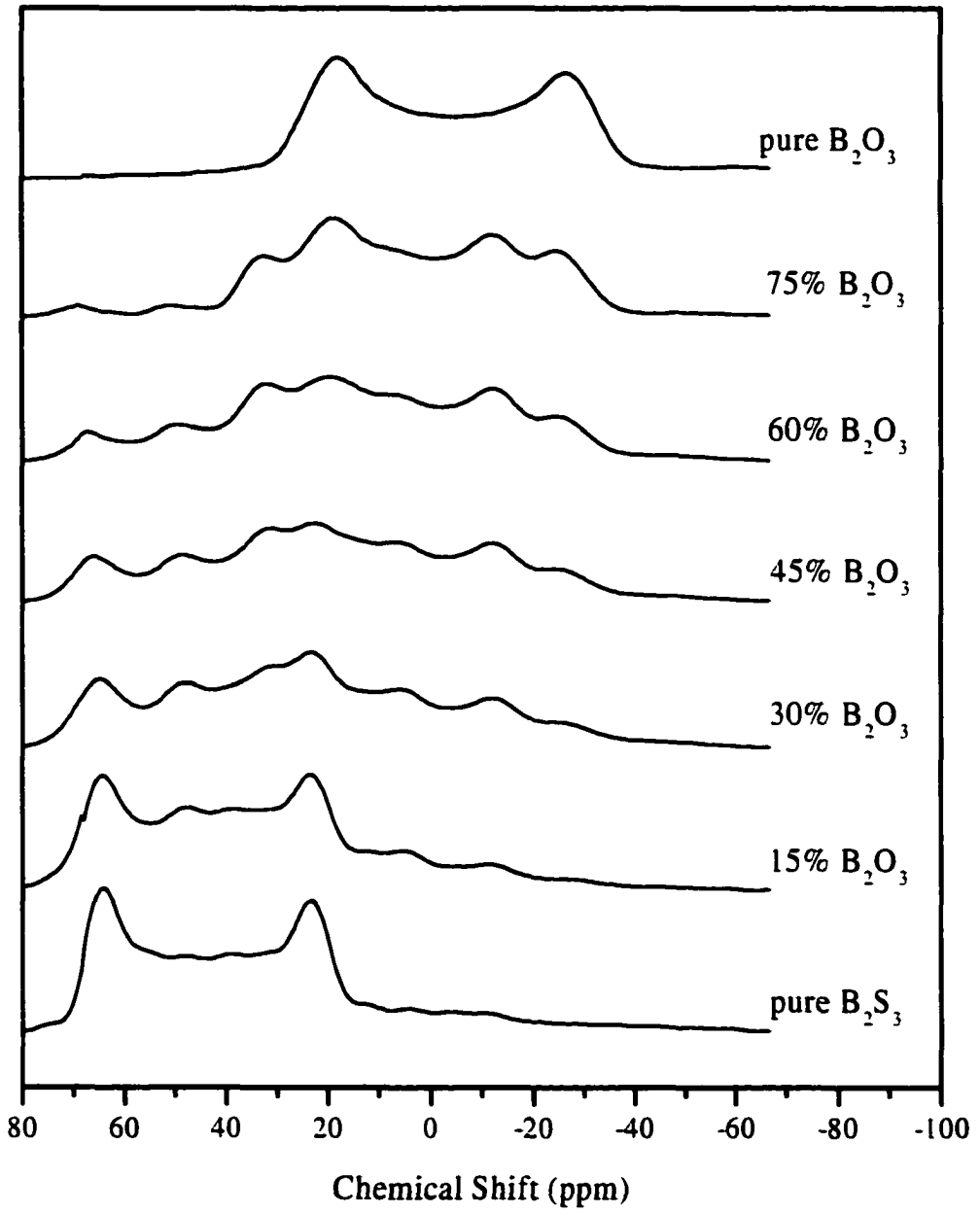


Figure (2-7)

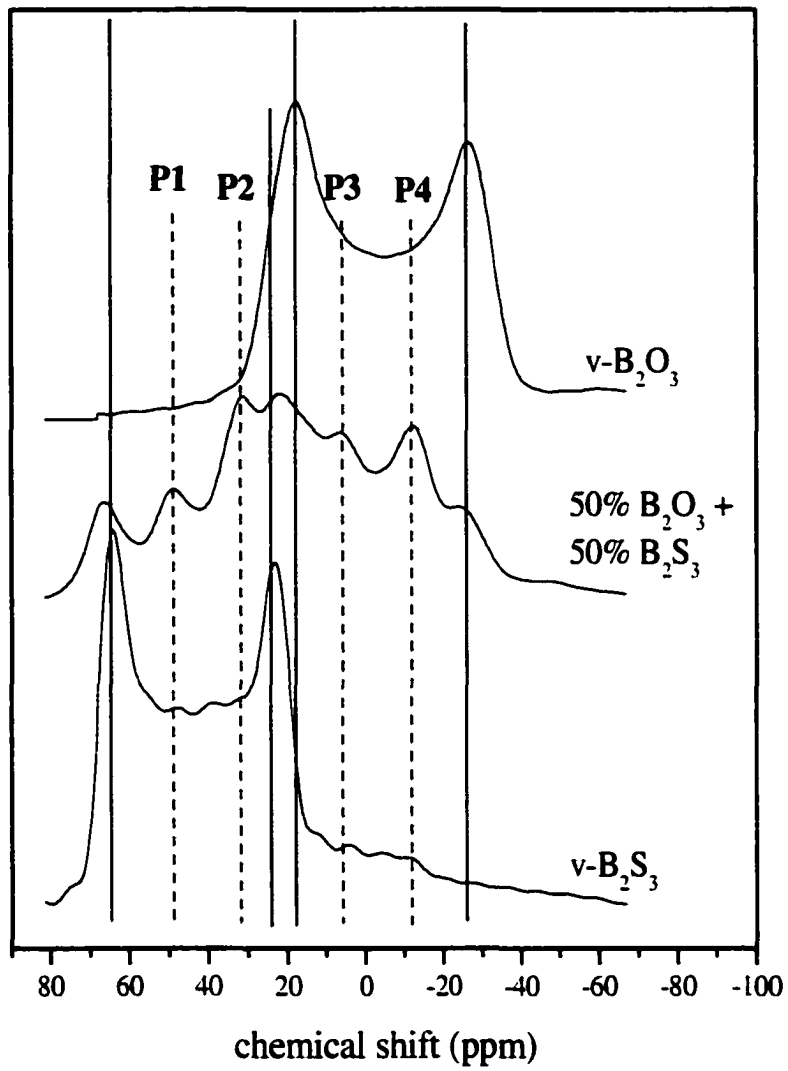


Figure (2-8)

3. Structural Characterization of Silver Thioborosilicate Glasses

By

J. Schrooten^{1,2}, B. Meyer^{2,3}, S.W. Martin^{2,4}

A paper submitted to the Journal of Non-Crystalline Solids, November 2001

3.1. Abstract

Fast Ion Conducting (FIC) glasses of composition $z \text{ AgI} + (1-z)[0.525 \text{ Ag}_2\text{S} + 0.475(0.5 \text{ B}_2\text{S}_3 + 0.5 \text{ SiS}_2)]$ where $0.0 \leq z \leq 0.4$ have been studied using Scanning Electron Microscopy (SEM), X-Ray Diffraction (XRD), Differential Scanning Calorimetry (DSC), Nuclear Magnetic Resonance (NMR), Raman spectroscopy, and Infrared (IR) spectroscopy to investigate their short-range order structure. These glasses are of significant interest due to the observation that they exhibit significant non-Arrhenius behavior in their ionic conductivity³. NMR, Raman and IR spectra show that the glasses of the above compositions are comprised primarily of silicon sulfide and boron sulfide tetrahedra with small amounts of B_2S_3 six-membered rings and B_2S_3 trigonal units as the glassy matrix. The addition of AgI appears to open up the glassy network without significant modification of the short-range order of the glassy matrix. SEM experiments show the samples are homogenous with little oxide contamination and the XRD experiments show that the samples are glassy with no evidence of crystallization.

¹ Primary researcher and author

² Department of Materials Science and Engineering, Iowa State University

³ Ames Laboratory – U.S. Department of Energy, Iowa State University, Ames, IA 50011

⁴ Author to whom correspondence should be directed

3.2. Introduction

Ion conducting glasses are of high interest due to their potential use as solid electrolytes in fuel cell or battery applications⁴². Glasses are of interest also because they have several advantages over their crystalline counterparts. These materials offer isotropic conductivity with an absence of grain boundaries. They offer wide compositional flexibility that allows for the optimization of electrolyte properties and can easily be fabricated into complex shapes. Thin-film batteries using ion-conducting glasses can be made and would enable new applications in microelectronics⁴³.

Recently, Kincs and Martin⁴⁴ reported the discovery of a fast ion conducting (FIC) glass in the AgI, Ag₂S, B₂S₃, and SiS₂ (silver thioborosilicate) system. This system was chosen using known relationships for the compositional dependence on ionic conductivity in an effort to develop the highest ionically conducting glass to date⁴⁵. As a result, the glasses produced in this system have exhibited record high room temperature ionic conductivities as well as good chemical stability, a known problem for chalcogenide systems.

Ionic conductivities as high as $10^{-2} (\Omega\text{-cm})^{-1}$ at room temperature have been measured in this system³. Unfortunately, while this is very high for a glassy material, strong non-Arrhenius temperature dependence was observed that decreased the conductivity several orders of magnitude lower than that predicted by the extrapolated low temperature Arrhenius behavior. An example of this behavior is shown in Fig. (3-1). This behavior is not exclusive to the silver thioborosilicate system; it has also been observed in glassy Ag₇L₄AsO₄⁴⁶ and in the AgI, Ag₂O, B₂O₃ systems⁴⁷. Several possible explanations for this dependence are that it is the result of coulombic interactions between the silver ions at higher temperatures⁴⁸. The non-Arrhenius behavior may also be explained by the coupling model where it is suggested

that this behavior indicates an upper limit for the ionic conductivity in a glass⁴⁹. However, it is also possible that this behavior is not an inherent property, but is instead the result of partially crystallized or perhaps phase separated materials.

In order to more completely understand the cause of the non-Arrhenius behavior, it is necessary to develop an accurate model of the structure of these glasses. This work uses Scanning Electron Microscopy (SEM), X-Ray Diffraction (XRD), Differential Scanning Calorimetry (DSC), Nuclear Magnetic Resonance (NMR), Raman spectroscopy, and Infrared (IR) spectroscopy in an attempt to elucidate the structure.

3.3. Experimental

3.3.1. Sample Preparation

In preparing the FIC samples, $z \text{ AgI} + (1-z)[0.525 \text{ Ag}_2\text{S} + 0.475(0.5 \text{ B}_2\text{S}_3 + 0.5\text{SiS}_2)]$, the commercially available starting materials AgI, Ag₂S, and SiS₂ are used in pure form. B₂S₃ is not commercially available and was prepared in the laboratory by the stoichiometric reaction of boron and sulfur powder in a carbon coated and evacuated silica ampoule⁵⁰.

All FIC glasses were prepared in an oxygen- and water-free (<1 ppm O₂, <1 ppm H₂O) glovebox from stoichiometric amounts of AgI (Cerac, Inc. 99.999%), Ag₂S (Cerac, Inc. 99.9%), B₂S₃, and SiS₂ (Cerac, Inc. 99.5%). Appropriate amounts of these powders were weighed into a vitreous carbon crucible and melted at 850°C for ten minutes. The samples were then checked for weight loss and were reheated for an additional five minutes. Weight losses were always less than 1%. The liquid was poured into a brass mold at the anneal temperatures listed in Table (3-1), allowed to anneal for thirty minutes, and then cooled at

5°C/min to room temperature. The careful annealing of the glass samples was performed to remove the possibility of sub- T_g annealing at elevated temperatures as a possible source of the non-Arrhenius conductivity.

3.3.2. Scanning Electron Microscopy

A Hitachi S-2460N "Environmental" or "low-vacuum" SEM was used at 10kV in a vacuum of 10^{-5} Torr in conjunction with a Link Isis energy-dispersive x-ray system with a high-resolution, light-element Ge detector on uncoated samples that were fractured just prior to examination.

3.3.3. X-Ray Diffraction

XRD work was performed using a Scintag X-Ray Diffractometer with an excitement voltage of 45 kV and a Cu source. The samples were scanned using uncovered polycarbonate sample holders.

3.3.4. Differential Scanning Calorimetry

A Perkin-Elmer Pyris 1 DSC running Pyris software version 3.01 was used. The calorimetry accuracy is $> \pm 1\%$ at a precision of $> \pm 0.1\%$. The temperature accuracy is $\pm 0.1^\circ\text{C}$ at a precision of $\pm 0.01^\circ\text{C}$.

Approximately 30 mg of glass powder was sealed in a hermetic aluminum pan and was heated at a rate of $10^\circ\text{C}/\text{min}$ through the glass transition temperature. The sample was

then cooled at 10°C/min to 50°C below the glass transition temperature (T_g) and again heated at 10°C/min to 500°C.

3.3.5. Infrared Spectroscopy

A Bio-Rad FTS-40 Fourier Transform Infrared Spectrometer was used. It has a spectral range of 4400 to 450 cm^{-1} at a maximum resolution of 0.5 cm^{-1} . Potassium bromide – glass powder pellets were used at a 1:10 volume ratio of glass to KBr to collect the IR spectra.

3.3.6. Raman Spectroscopy

A Brüker RFS 200/S FT-Raman Spectrometer was used. It uses an Nd:YAG Laser operating at 1064 nm as the excitation source. This instrument has a useful Stokes shift spectral range of 120 to 3600 cm^{-1} . Powder samples weighing less than 10 mg were used in a 180° backscatter experiment at powers of typically <100 mW to collect the Raman spectra.

3.3.7. Nuclear Magnetic Resonance

A homebuilt phase coherent pulse NMR with a field of 4.7 T (64.179 MHz) was used⁵¹. This was done through collaboration with B. Meyer and F. Borsa at the Iowa State University Physics NMR Laboratory.

3.4. Results

3.4.1. Scanning Electron Microscopy

SEM was used to check for the presence of either liquid-liquid or liquid-solid phase separation. Figure (3-2) shows the backscattered electron SEM micrograph for 0.0 AgI+1.0[0.525 Ag₂S+0.475(0.5 B₂S₃+0.5 SiS₂)]. This image is taken of a cast sample broken in half to expose an internal fracture surface and shows one of the edges. From this micrograph, it can be seen that there is either a second phase or that the sample may be porous. The size and concentration of this second phase increases from the edge toward the center of the sample. Figure (3-3) shows a magnified view of the center of the sample where it can be seen that the size of the second phase is on the order of 1 to 10 μm. Also present in this micrograph, is what looks like a particle inside of one of the holes. This indicates that the sample is indeed partially phase separated and not porous. Figure (3-4) is SEM image showing the location of the Energy Dispersive Spectroscopy (EDS) analysis shown in Figs. (3-5) and (3-6). Notice that EDS spectra taken of the bulk sample, Fig. (3-5), indicates that the bulk has very little oxygen contamination, but that the second phase, Fig. (3-6), shows a high concentration of oxygen. For this composition, the volume fraction of the oxide phase is estimated at approximately 6%.

Figure (3-7) is a SEM micrograph of 0.2 AgI+0.8[0.525 Ag₂S+0.475(0.5 B₂S₃+0.5 SiS₂)]. EDS was also performed at several points in the sample with the results the same as for 0.0 AgI+1.0[0.525 Ag₂S+0.475(0.5 B₂S₃+0.5 SiS₂)] where the black regions contained very high amounts of oxygen and the bulk material contained very little oxygen. The oxide

phase constitutes 1.5% volume fraction of the sample. The addition of AgI vastly decreases the amount of phase separation as well as decreases the average size of the oxide phase.

Finally, Fig. (3-8) is a SEM micrograph of 0.4 AgI+0.6[0.525 Ag₂S+0.475(0.5 B₂S₃+0.5 SiS₂)]. EDS was also performed at several points in the sample; the results were again the same as for the other two compositions where the black regions contained very high amounts of oxygen and the bulk material contained very little oxygen. The oxide phase has decreased to a volume fraction of only 0.5% for this composition.

The result of the SEM analysis is that the samples do contain a very small amount of oxide contamination. With zero AgI there is a volume fraction of 6% oxide in the glass; this decreases to 0.5% at 0.4 AgI. Figure (3-9) directly compares the composition of the bulk material for $z = 0.0$ and $z = 0.4$. The amount of oxygen contamination of the bulk remains constant as AgI concentration is increased. This indicates that the AgI acts to “fine” the glass melt allowing the oxygen contamination to separate out of the melt. Such a process is well known in oxide glasses where the metal halide NaCl is added to the glass batch to remove OH contamination.

3.4.2. X-Ray Diffraction

XRD was used to check for the presence of crystallization. Figure (3-10) shows the results after allowing the samples to anneal for 90 minutes at their respective anneal temperatures as given in (3-1). The only two features are the broad humps centered at $\sim 13^\circ$ and $\sim 32^\circ$. The fact that these features are very broad, approximately 15° , indicates that there is no detectable amount of crystallization. Figure (3-11) shows the powder pattern for a

crystallized sample. There are now a number of very sharp, well-defined peaks at 28.9° , 33.7° , 43.9° , and 48.1° as well as the broad hump at 13° . The contrast between Figs. (3-10) and (3-11) further illustrates that after annealing for 90 minutes there is no crystallization present in the samples. XRD was performed on samples after several different anneal times; Fig. (3-12) shows the results. As the anneal time is increased, the broad humps at 13° and 32° decrease in intensity indicating that the structure may be becoming less ordered as it is allowed to anneal, not crystallizing.

3.4.3. Differential Scanning Calorimetry

The results of the DSC analysis are summarized in (3-1) and shown in Fig. (3-13). The glass transition temperature is 358°C for the $z = 0.0$ samples and decreases to 255°C for the $z = 0.4$ sample. In general, the glass stability also decreases as AgI is added as is evident by the decreasing temperature difference between the glass transition and the glass crystallization temperatures, as shown in (3-1).

3.4.4. Raman Spectroscopy

The Raman spectra are given in (3-2) and are shown in Fig. (3-14). The first feature of interest occurs at 375 cm^{-1} and corresponds to the symmetric vibration of S in edge sharing tetrahedral (bitetrahedral) units⁵². The main mode in these spectra occurs at 400 cm^{-1} , which corresponds to S vibration in SiS_2 tetrahedra⁵². At 450 and 500 cm^{-1} are two small peaks that indicate the presence of B_2S_3 rings⁵³. The second most prominent mode is a broad mode centered at 725 cm^{-1} and corresponds to S vibration in tetrahedral BS_4 units⁵³.

The final peak is very small and occurs at 800 cm^{-1} which corresponds to the stretching of S in trigonal BS_3 units⁵³. Notice that as the amount of AgI present in the samples is increased, there are no new modes seen in the spectra. The addition of AgI has the effect of slightly shifting the peaks to higher wavenumbers as well as slightly sharpening up the peaks.

3.4.5. Infrared Spectroscopy

The infrared spectra support the findings of the Raman analysis. These results are summarized in (3-2) and shown in Fig. (3-15). The two main features of these spectra are the vibration of tetrahedral SiS_2 units at ~ 500 wavenumbers⁵⁴ and the vibration of BS_4^- units at 680 and 780 wavenumbers⁵⁵. The intensity for trigonal or six-membered rings of B_2S_3 is very weak and barely visible over the noise level in the spectra. As in the Raman spectra, the addition of AgI appears to have little effect on the IR spectra, and hence upon the structure of the glass, only a slight shift to higher wavenumbers and a slight sharpening of the peaks.

3.4.6. Nuclear Magnetic Resonance

The NMR spectrum of ^{11}B for pure B_2S_3 is shown in Fig. (3-16)⁵⁴. The data was collected on a homebuilt phase-coherent pulsed NMR with the ^{11}B resonance centered at 22.000 MHz. The two large peaks at 22.025 MHz and 21.99 MHz are attributed to trigonal boron. While Ag is not an alkali metal; it does carry a +1 charge and behaves similar to alkali metals in borate glass systems⁵⁶ so comparing the Ag data to alkali data should allow for peak assignments. The effect of the addition of 70 mole percent Li is shown in Fig. (3-17)⁵⁴. This data was collected on a homebuilt phase-coherent pulsed NMR with the ^{11}B

resonance centered at 22.050 MHz. The large peak at 22.01 MHz is attributed to tetrahedral boron. The results of the NMR analysis on the $z \text{ AgI} + (1-z)[0.525 \text{ Ag}_2\text{S} + 0.475(0.5 \text{ B}_2\text{S}_3 + 0.5 \text{ SiS}_2)]$ system are shown in Fig. (3-18). There are three features of interest, a main peak at -1.392 MHz and two very small peaks at -5.655 MHz and 7.961 MHz . The main peak is due to tetrahedral BS_2 units; both small peaks are due to B_2S_3 trigonal units. This is known due to boron being a $3/2$ -spin nucleus and due to the asymmetry of a trigonal site; there is a splitting of the resonance peak as a result of quadrupolar interactions. As with the Raman and the IR results, the addition of AgI has no significant effect on the structure of the glass. The relative area under the peaks is 72.7% for the 4-fold coordinated boron and 27.3% for the 3-fold coordinated boron units.

3.5. Discussion

The SEM analysis shows that the samples contain a small amount of oxide contamination, but that this oxide contamination decreases as AgI content increases. This is in contrast to the observed conductivity result where the non-Arrhenius deviation becomes more pronounced as AgI content is increased³. Since the glasses become less contaminated as AgI is increased, it is unlikely that the small amount of oxide contamination is the cause of the observed non-Arrhenius behavior.

Likewise, the XRD analysis shows that the samples contain very little if any amount of crystallinity. This is in agreement with results obtained from neutron diffraction that found negligible amounts of crystallinity⁵⁷.

Spectroscopic analysis concludes that the glasses are comprised primarily of SiS_2 and BS_2 tetrahedra with small amounts of B_2S_3 six-membered rings and trigonal units.

Compositionally, if the glass were only composed of B_2S_3 and SiS_2 , it would be expected that spectroscopic analysis would reveal the glass to be comprised of only SiS_2 tetrahedra and B_2S_3 six-membered rings and trigonal units. The addition of a modifier has the possibility of changing the structure in several ways. If the modifier was only associated with the B_2S_3 , then the presence of BS_4 units would be expected as the modifier transforms the trigonal boron into tetrahedral boron. Assuming that Ag_2S behaves similar to Li_2S in the silver thioborosilicate glasses, then this conversion occurs until a modifier mole fraction of approximately 0.3 where the boron starts to be converted back to trigonal boron with one non-bridging sulfur^{58,59}. At this modifier concentration, the tetrahedral boron concentration is approximately 80% of the boron with the remaining 20% being trigonal boron. If the modifier ions were only associated with the SiS_2 , then no tetrahedral boron would be expected.

The NMR results showed that approximately 71% of the boron is in four-fold coordinated structures. Since 0.525 mole fraction of Ag_2S is present in the glass, half of that is 0.2625, just slightly under the 0.3 mole fraction required for the highest boron conversion to four-fold coordination. The observation of nearly all the boron in four-fold coordinated structures indicates that the modifying Ag_2S appears to be shared equally between the silicon and boron structural units.

Spectroscopically, the addition of AgI appears to have very little effect on the structure of the glass and this result is also corroborated by the NMR results. An explanation of this effect would be that the AgI causes an expansion of the structure of the glass possibly by dissolving into voids in the glass matrix. This hypothesis is supported by neutron

diffraction data where the lengths from the intermediate range order of the glass are increased⁵⁷.

DSC measurements show a pronounced crystalline exotherm after the glass transition temperature indicating the glassy nature of the materials at temperature below the glass transition. The addition of AgI decreases the stability of the glass, which is in agreement with the hypothesis that the AgI causes a network expansion of the glass.

3.6. Conclusions

This investigation studied the physical structure of silver thioborosilicate glass using SEM and XRD techniques to determine phase purity and amount of crystallization present in the samples. It looked at several analytical techniques to determine the structure of the glass and the effect changing AgI concentration had on that structure.

The samples are shown to be free of significant amounts of oxidation or crystallization. The structure of the glass is primarily composed of SiSi_2 and BS_2 tetrahedra with small amounts of B_2S_3 six-membered rings and trigonal units. These structural units appear to intermix with the Ag_2S adding equally to the B_2S_3 structures and to the SiSi_2 structures. The addition of AgI has very little effect on the structure of the glass due to AgI dissolving into voids in the glass causing a network expansion. This occurs without disrupting the short-range order of the glass.

3.7. Acknowledgements

This work was conducted by support of National Science Foundation grant number DMR-99-72466.

3.8. References

-
- ⁴² Fusco, F. A., Tuller, H. L., *Fast Ion Transport in Glasses*; p. 43; Superionic Solids and Solid Electrolytes; Academic press; 1989
- ⁴³ Balkanski, M., *Physics World*, 29-33 (1990)
- ⁴⁴ Kincss, J., Martin, S. W., *Phys. Rev. Lett.*, **76**, 70-73
- ⁴⁵ Kincs, J., Masters Thesis, Iowa State University (1994)
- ⁴⁶ Ingram, M.D., Grant, R.J., Turner, L.D.S., Vincent, C.A., *J. Phys. Chem.* 82, B26B (1978)
- ⁴⁷ Shaju, K.M., Chandra, S., *Phys. Stat. Sol (b)* **181**, 301 (1994)
- ⁴⁸ Maass, P., Meyer, M., Bunde, A., Dieterich, W., *Phys. Rev. Lett.* **77**, 1528 (1996)
- ⁴⁹ Ngai, K.L., Rizos, A.K., *Phys. Rev. Lett.* **76**, 1296 (1996)
- ⁵⁰ Martin, S.W., Bloyer, D., *J. Am. Ceram. Soc.*, **74**, 1003 (1991)
- ⁵¹ The NMR Spectrometer employed a programable pulse sequencer: Adduci, D.J., Gerstein, B.C., *Rev. Sci. Instrum.*, **50**, 1403 (1979); a double side band r.f. switch design by Torgeson, D.R. and Adduci, D.J. (unpublished) and a fast recovery receiver following the design of Adduci, D.J., Hornung, P.A., Torgeson, D.R., *Rev. Sci. Instrum.*, **47**, 1503 (1976)
- ⁵² Tenhover, M., Hazle, M.A., Grasselli, R.K., *Phys. Rev. B*, **29**, 12 (1984)
- ⁵³ Royle, M., Cho, J., Martin, S.W., submitted *J. Non-Cryst. Sol.*
- ⁵⁴ Sills, J., Masters Thesis, Iowa State University (1990)
- ⁵⁵ Cho, J., Ph.D. Thesis, Iowa State University (1995)
- ⁵⁶ Kim, K.S., Bray, P.J., *J. Nonmetals*, **2**, 95 (1974)
- ⁵⁷ Matic, A., Swenson, J., Börjesson, Akai, T., Schrooten, J., Martin, S.W., submitted *J. Non-Cryst. Sol.*
- ⁵⁸ Suh, K.S., Hojjaji, A., Velleneuve, G., Ménérier, M., Levasseur, *J. Non-Cryst. Sol.*, **128**, 13 (1991)
- ⁵⁹ Zhang, Z., Kennedy, J.H., Thompson, J., Anderson, S., Lathrop, D.A., Eckert, H., *Appl. Phys. A*, **49**, 41 (1989)

3.9. Captions

Table (3-1). Summary of glass transition and crystallization temperatures.

Table (3-2). Peak assignments for Raman and IR spectroscopy.

Figure (3-1). Plot of the d.c. conductivity showing the transition from Arrhenius behavior at low temperatures to non-Arrhenius behavior at higher temperatures for a glass of composition $0.3 \text{ AgI} + 0.7[0.525 \text{ Ag}_2\text{S} + 0.475(0.5 \text{ B}_2\text{S}_3 + 0.5 \text{ SiS}_2)]$.

Figure (3-2). SEM backscattered micrograph of $0.0 \text{ AgI} + 1.0[0.525 \text{ Ag}_2\text{S} + 0.475(0.5 \text{ B}_2\text{S}_3 + 0.5 \text{ SiS}_2)]$

Figure (3-3). Secondary electron image of $0.0 \text{ AgI} + 1.0[0.525 \text{ Ag}_2\text{S} + 0.475(0.5 \text{ B}_2\text{S}_3 + 0.5 \text{ SiS}_2)]$

Figure (3-4). Backscattered SEM image of $0.0 \text{ AgI} + 1.0[0.525 \text{ Ag}_2\text{S} + 0.475(0.5 \text{ B}_2\text{S}_3 + 0.5 \text{ SiS}_2)]$ at a magnification of 500x. The numbered crosshairs correspond to points where EDS spectra were taken.

Figure (3-5). EDS spectra taken at point 5, the bulk of the sample, of Fig. (3-4).

Figure (3-6). EDS spectra taken at point 1, part of the second phase, of Fig. (3-4).

Figure (3-7). Backscattered SEM image of $0.2 \text{ AgI} + 0.8[0.525 \text{ Ag}_2\text{S} + 0.475(0.5 \text{ B}_2\text{S}_3 + 0.5 \text{ SiS}_2)]$ at a magnification of 1500x. The numbered crosshairs correspond to points where EDS spectra were taken.

Figure (3-8). Backscattered SEM image of $0.4 \text{ AgI} + 0.6[0.525 \text{ Ag}_2\text{S} + 0.475(0.5 \text{ B}_2\text{S}_3 + 0.5 \text{ SiS}_2)]$. The numbered crosshairs correspond to points where EDS spectra were taken.

Figure (3-9). EDS comparison showing that bulk oxygen contamination remains constant as AgI concentration is increased.

Figure (3-10). XRD powder patterns of compositions $z = 0.0, 0.1, 0.2,$ and 0.3 after annealing at their respective anneal temperature as given in (3-1) for 90 minutes.

Figure (3-11). XRD powder pattern of glass with of $z = 0.1$ AgI after crystallizing at 370°C .

Figure (3-12). XRD powder pattern of glass with $z = 0.2$. This plot looks at the effect of anneal time. As the anneal time is increased, the counts per second decrease, indicating that the structure may be becoming more disordered as it is allowed to anneal, and not crystallizing.

Figure (3-13). Results of the DSC analysis.

Figure (3-14). Results of the Raman spectroscopy analysis.

Figure (3-15). IR spectra of z AgI + $(1-z)[0.525 \text{ Ag}_2\text{S} + 0.475(0.5 \text{ B}_2\text{S}_3 + 0.5 \text{ SiS}_2)]$ samples.

Figure (3-16). ^{11}B NMR of pure B_2S_3 (from ref. 54).

Figure (3-17). ^{11}B NMR of $0.7 \text{ Li}_2\text{S} + 0.3 \text{ B}_2\text{S}_3$ (from ref. 54).

Figure (3-18). Results of NMR analysis

Table (3-1)

Composition	Anneal	Glass Transition	Crystallization	$T_x - T_g$
$z \text{ AgI} + (1-z)[0.525$	Temperature	Temperature, T_g	Temperature, T_x	
$\text{Ag}_2\text{S} + 0.475(0.5\text{B}_2\text{S}_3$	(°C)	(°C)	(°C)	
$+0.5\text{SiS}_2)]$		($\pm 0.5^\circ\text{C}$)	($\pm 0.5^\circ\text{C}$)	
$z = 0.0$	245	358	-	-
$z = 0.1$	240	288	355	67
$z = 0.2$	230	269	329	60
$z = 0.3$	210	252	283	31
$z = 0.4$	200	255	285	30

Table (3-2)

Structural Unit	Raman (cm^{-1})	Infrared (cm^{-1})
	($\pm 2 \text{ cm}^{-1}$)	($\pm 2 \text{ cm}^{-1}$)
SiS_2	375, 400	500
BS_2	725	680, 780
B_2S_3 6-membered rings	450, 500	900
Trigonal units	800	800

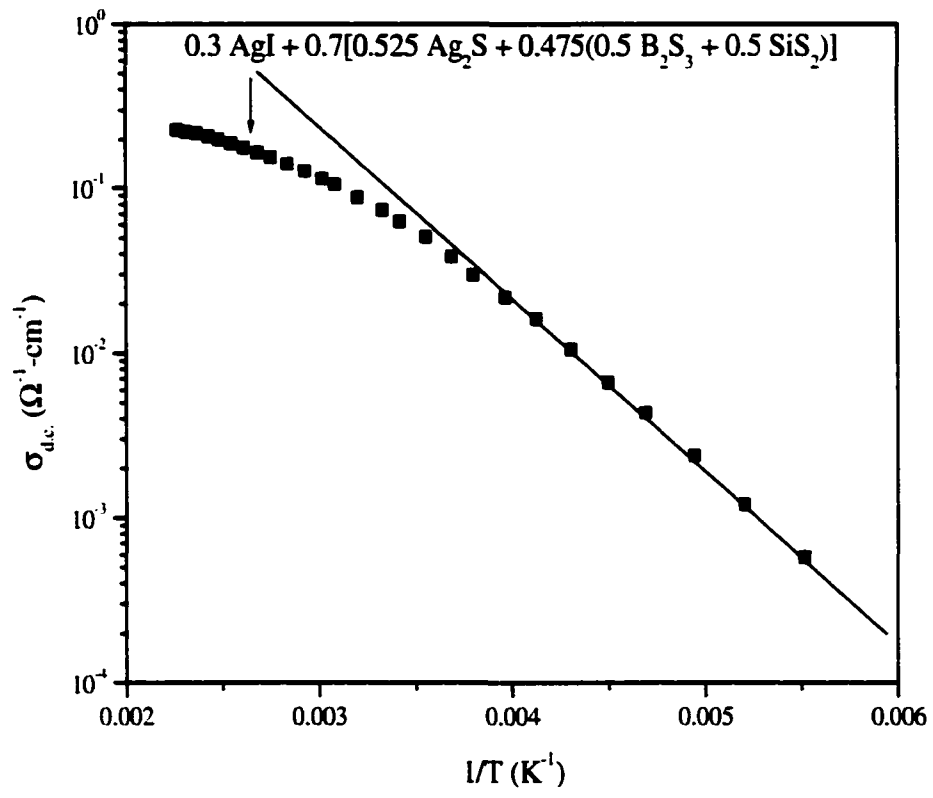


Figure (3-1)

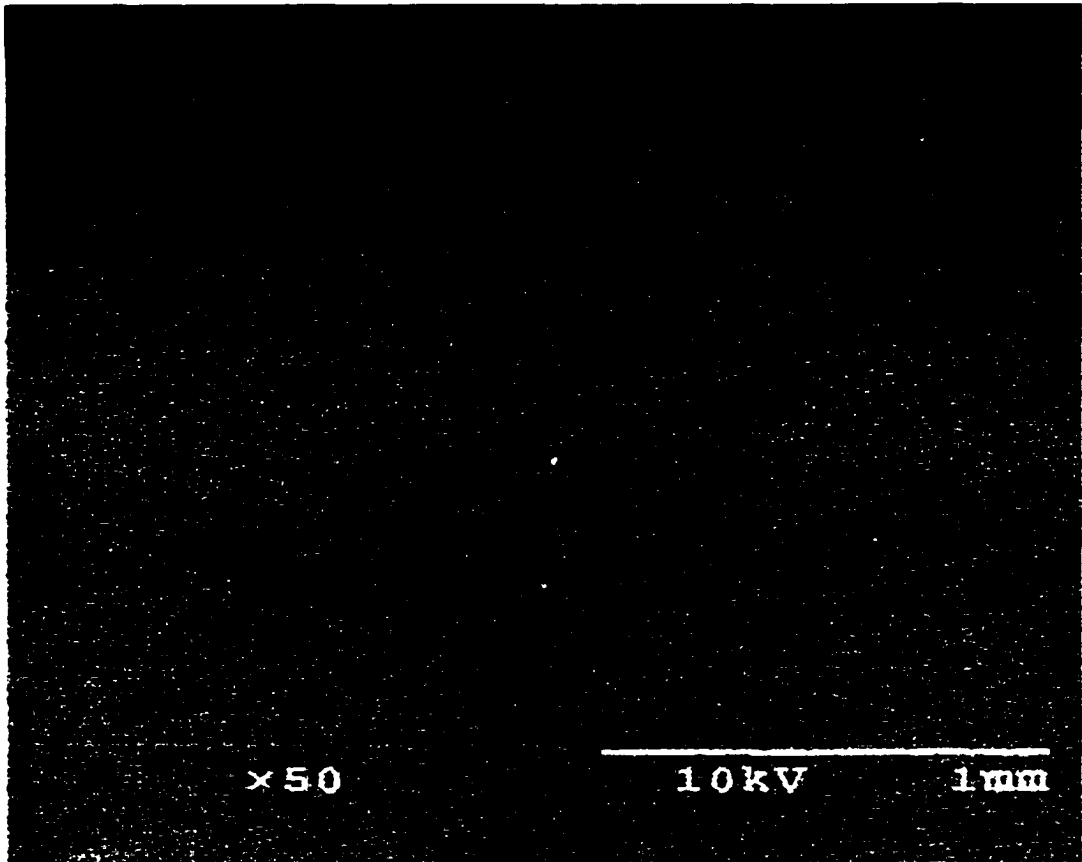


Figure (3-2)

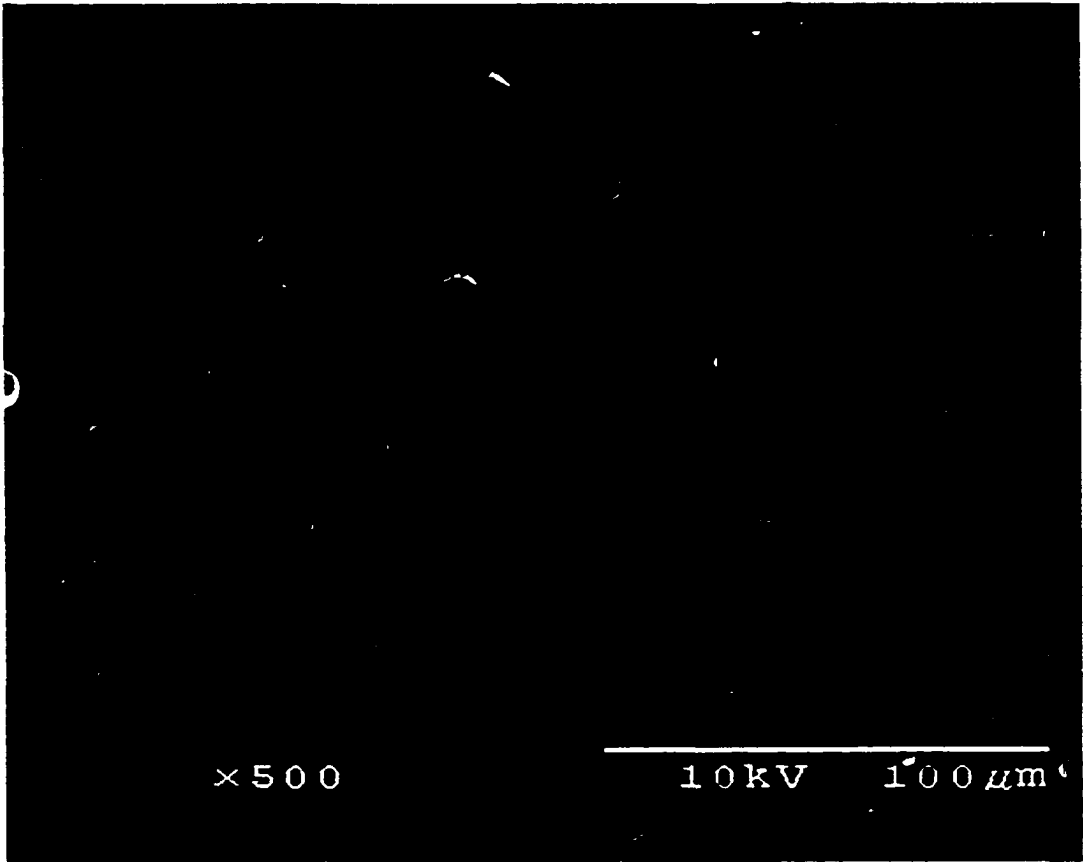


Figure (3-3)



Figure (3-4)

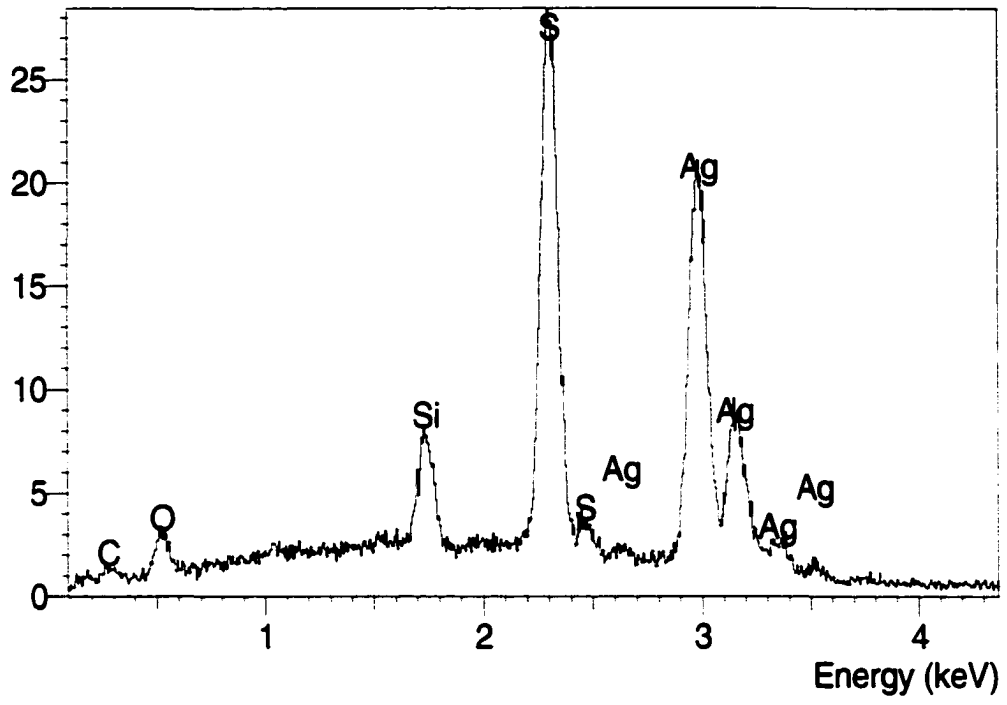


Figure (3-5)

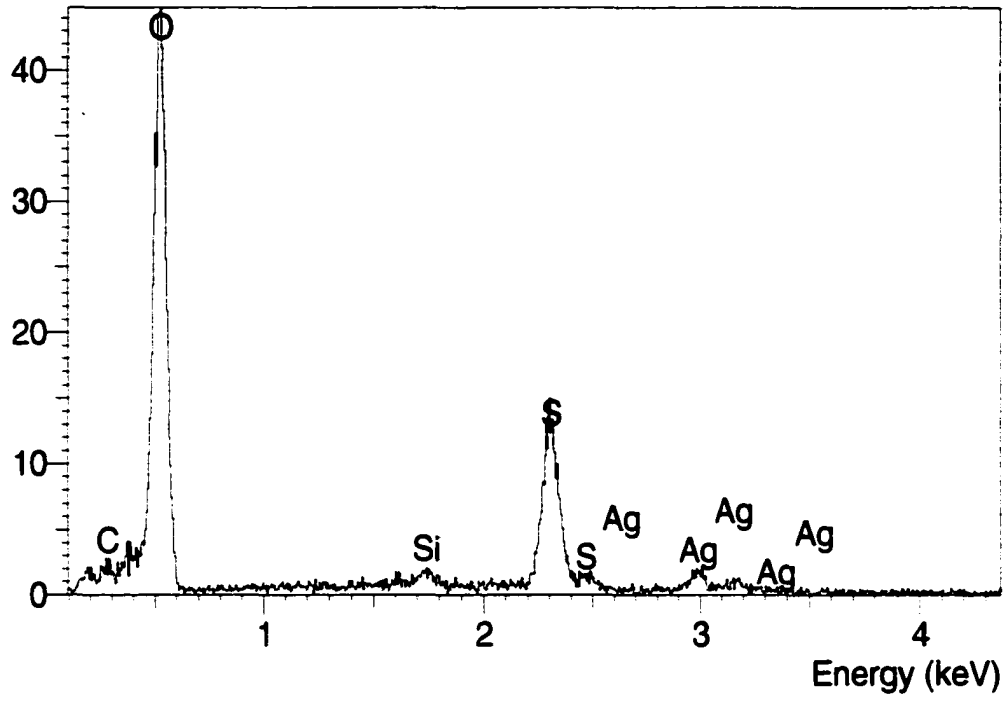


Figure (3-6)

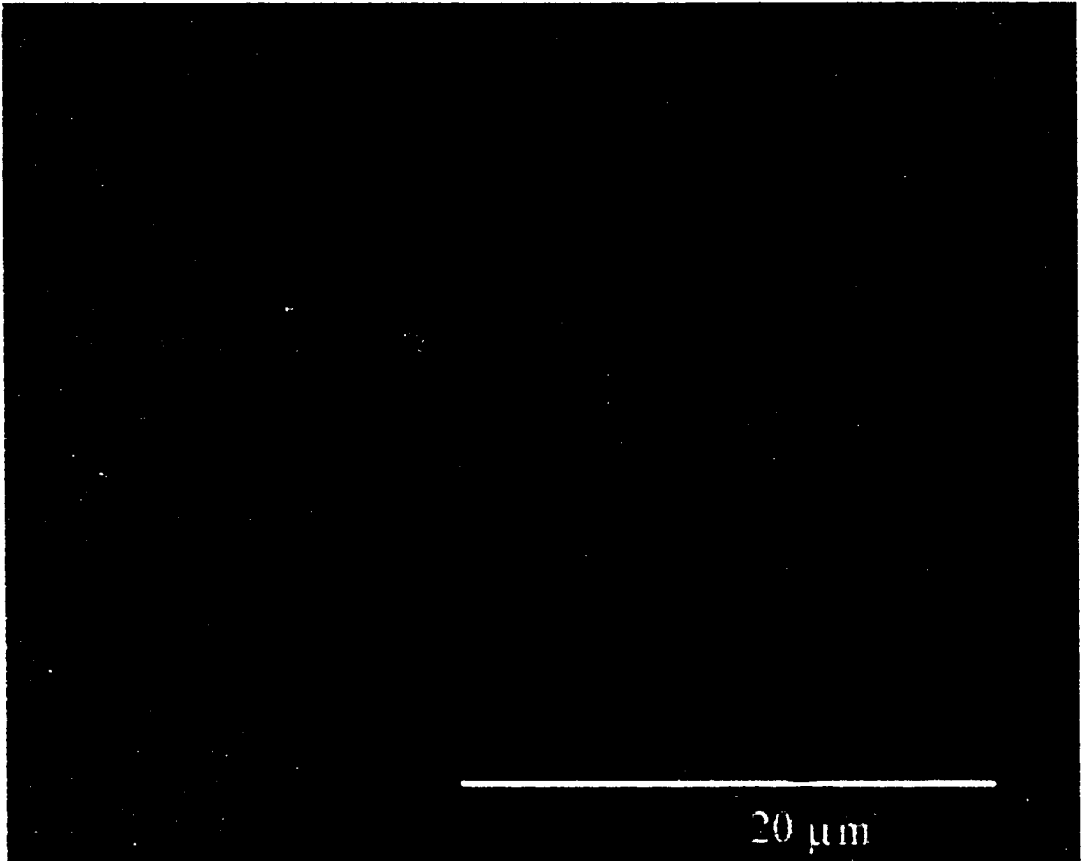


Figure (3-7)

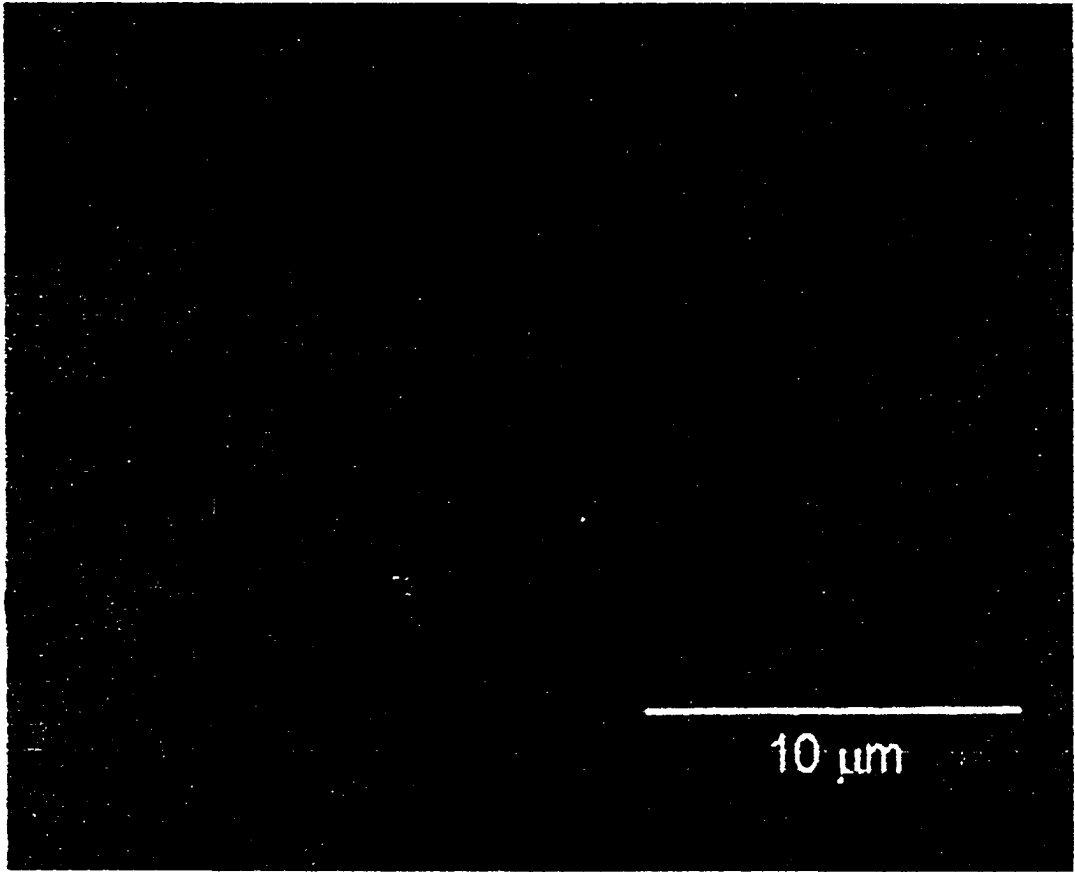


Figure (3-8)

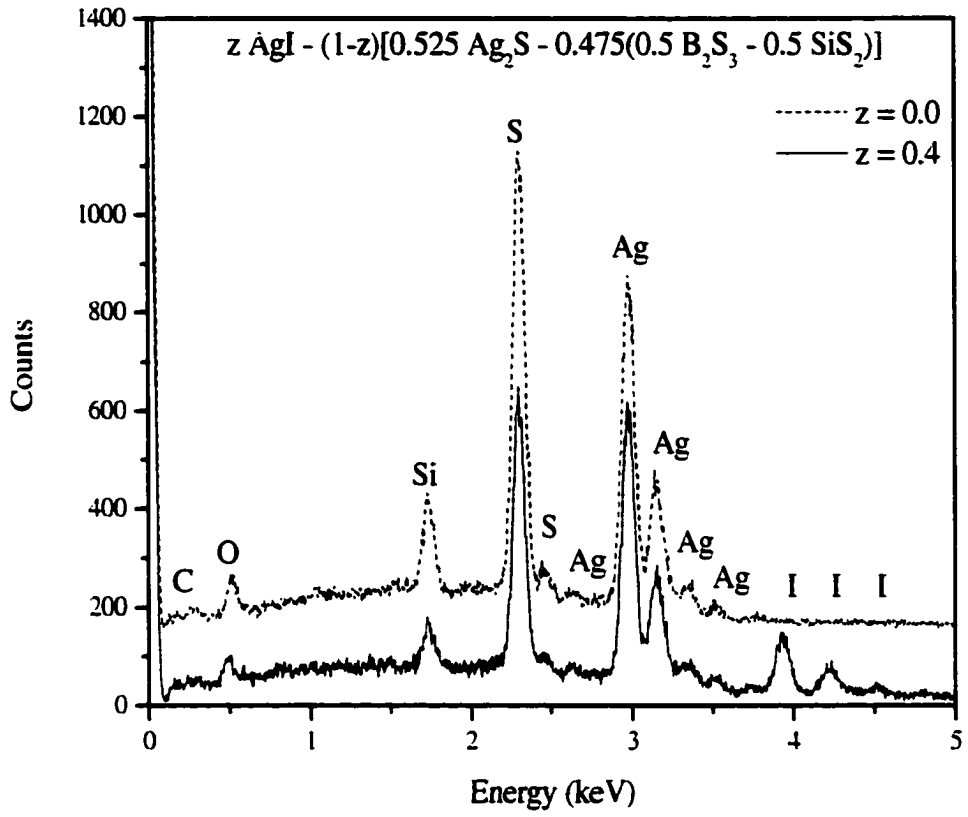


Figure (3-9)

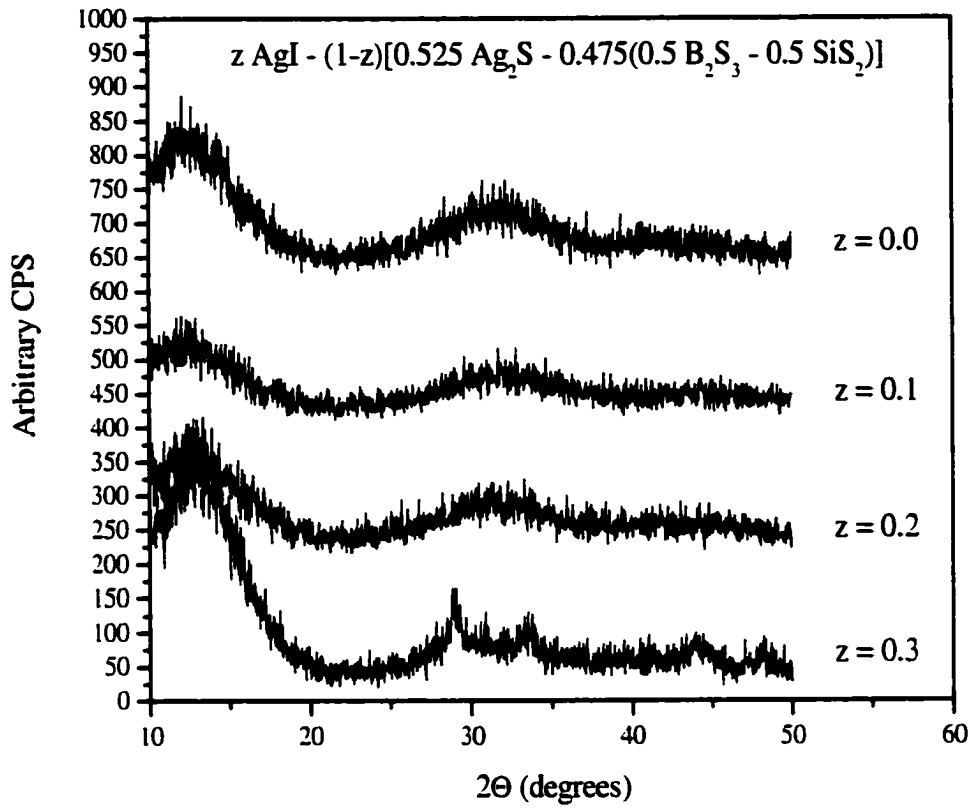


Figure (3-10)

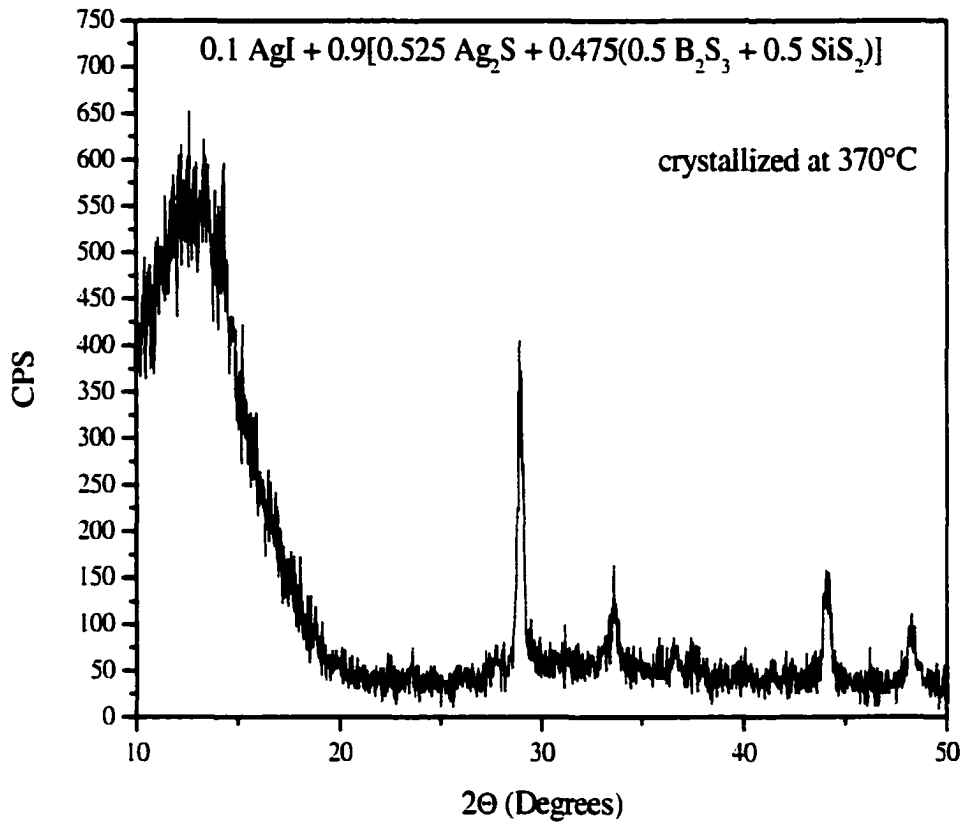


Figure (3-11)

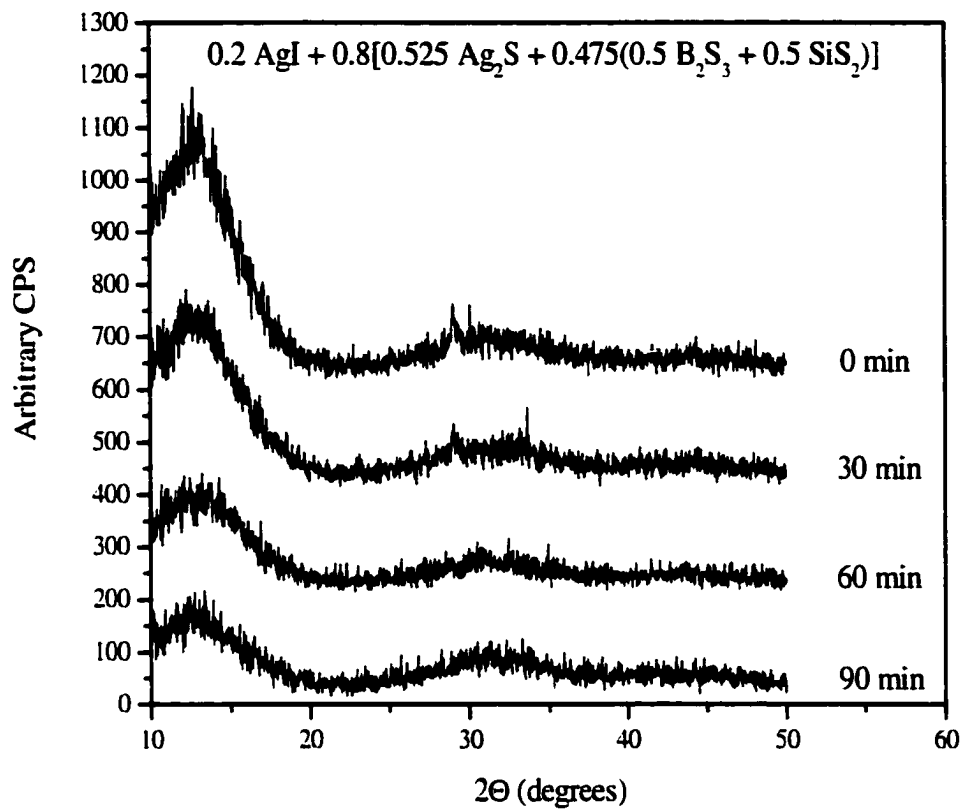


Figure (3-12)

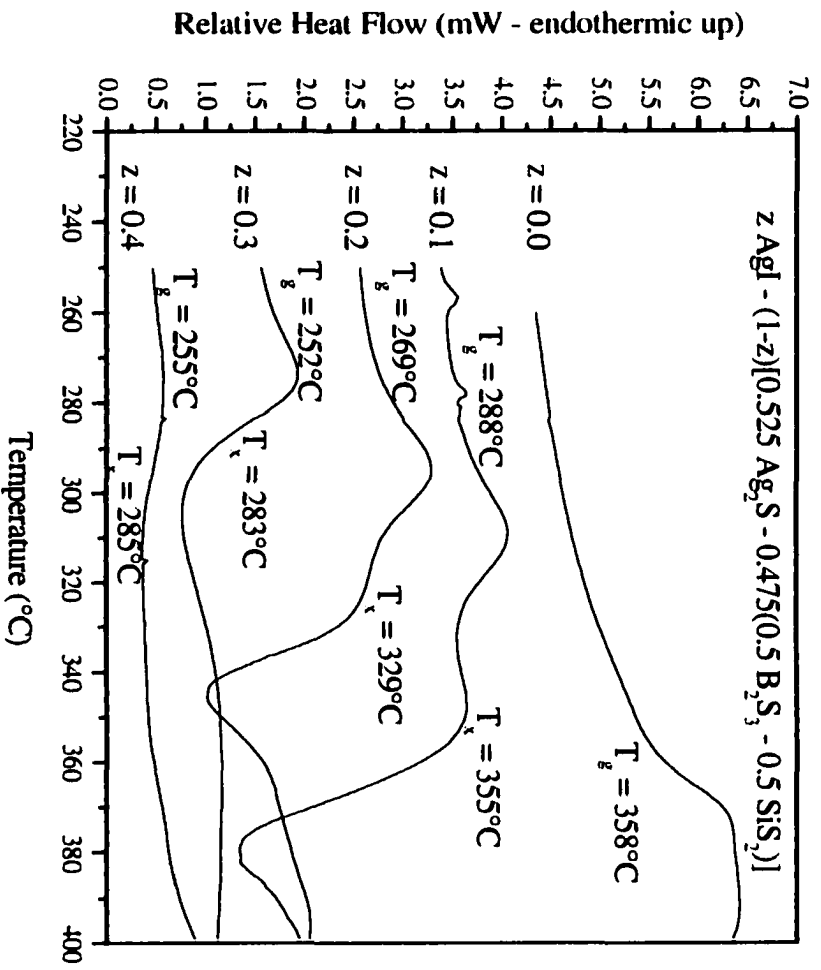


Figure (3-13)

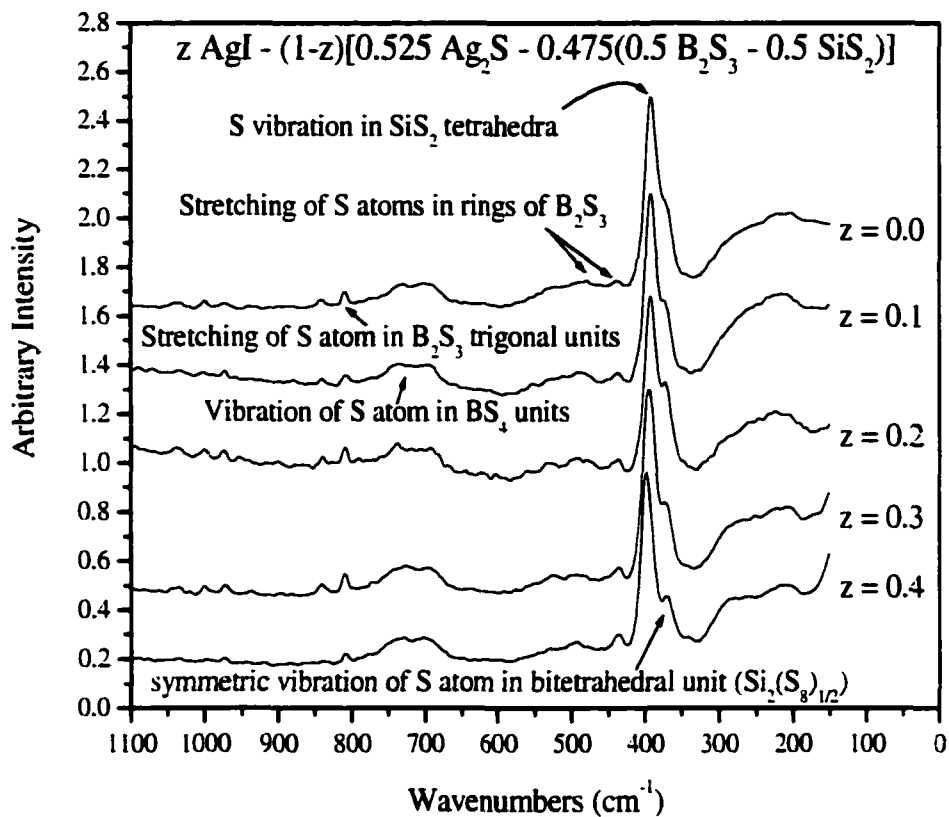


Figure (3-14)

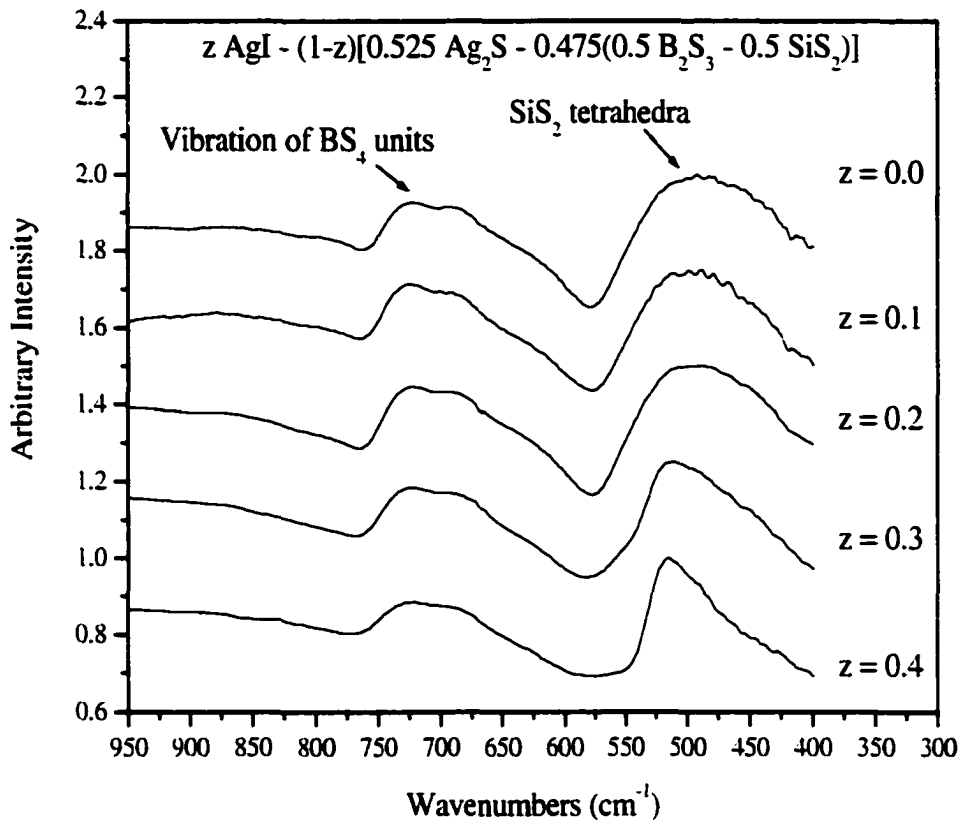


Figure (3-15)

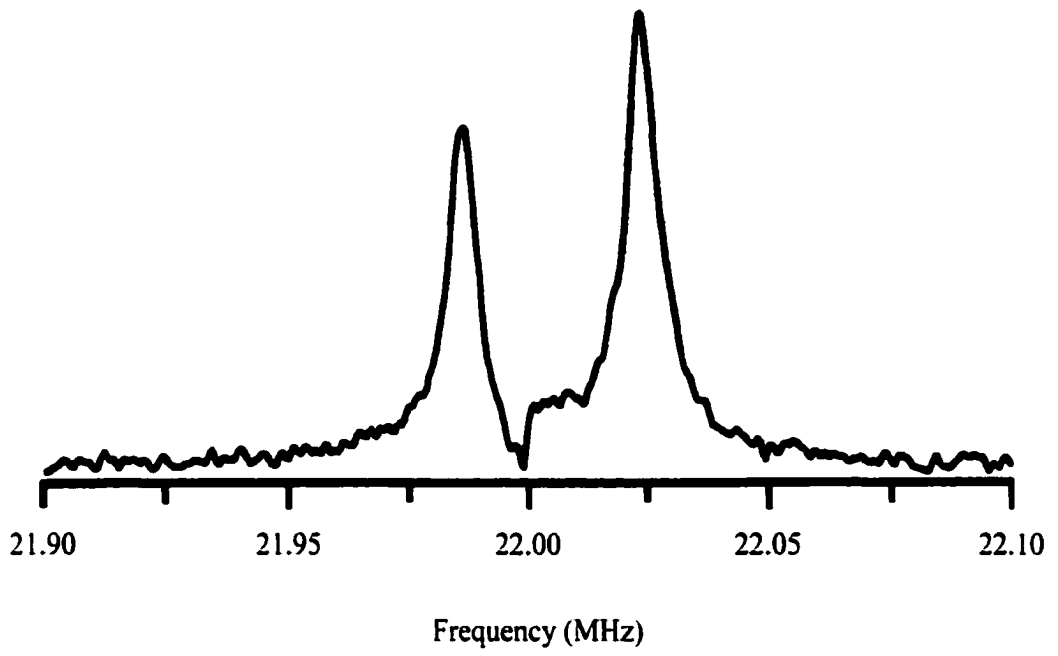


Figure (3-16)

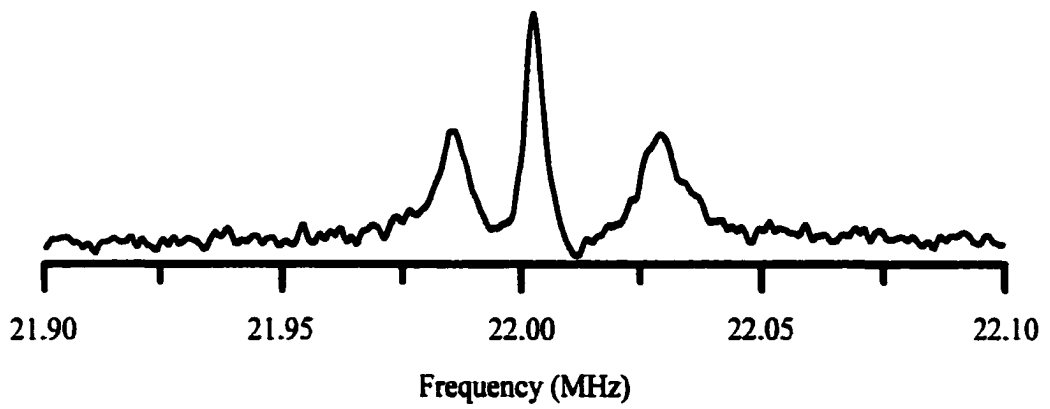


Figure (3-17)

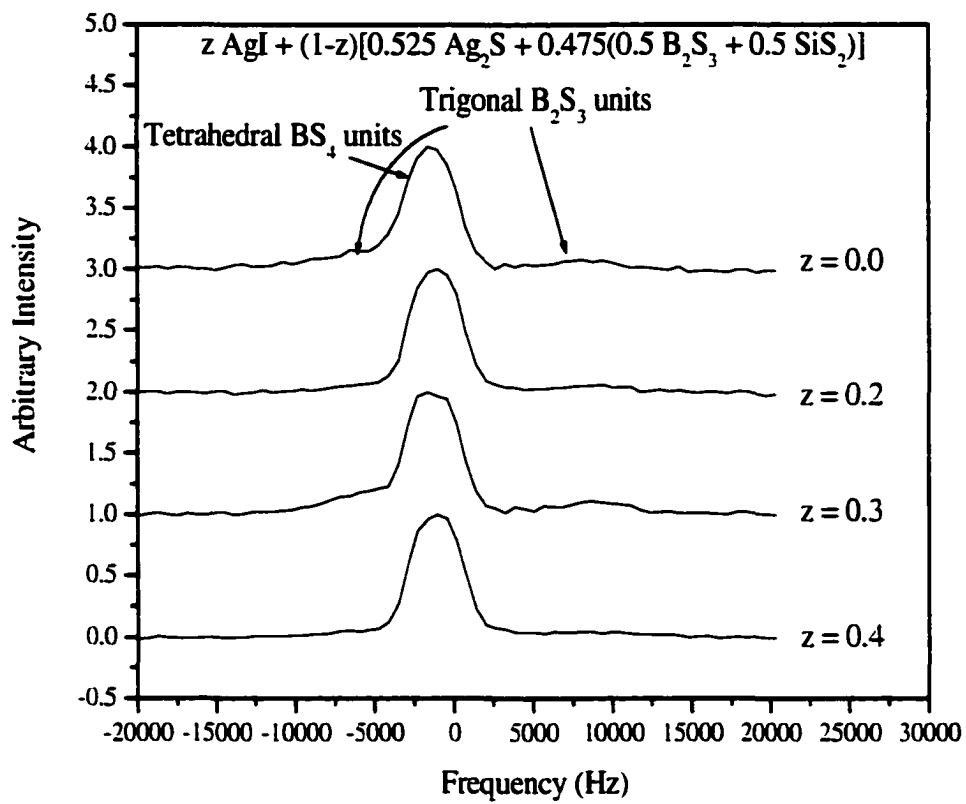


Figure (3-18)

4. Ion Scattering Model as an Explanation of Non-Arrhenius Ionic Conductivity

By

J. Schrooten^{1,2}, B. Meyer^{2,3}, S.W. Martin^{2,4}

Submitted to Physical Review B: Condensed Matter Physics, November 2001

4.1. Abstract

High temperature conductivity measurements of $z \text{ AgI} + (1-z)[0.525 \text{ Ag}_2\text{S} + 0.475(0.5 \text{ B}_2\text{S}_3 + 0.5 \text{ SiS}_2)]$ where $0 \leq z \leq 0.4$ fast ion conducting (FIC) glasses were performed to determine the conductivity behavior above room temperature. A distinct non-Arrhenius deviation is observed that causes the dc conductivity to be lower than is expected by extrapolating the low temperature results. This deviation becomes more pronounced and occurs at lower temperatures as AgI content is increased.

A new model is proposed, the Ion Scattering Model, which takes a physical approach to explain the cause of the non-Arrhenius deviation. By assuming the high temperature conductivity is limited by mobile ion scattering, good fits with experimental data was achieved in the non-Arrhenius region. As expected, due to the assumption that the ions do not conduct independently the low temperature conductivity is over-estimated.

¹ Primary researcher and author

² Department of Materials Science and Engineering, Iowa State University

³ Ames Laboratory – U.S. Department of Energy, Iowa State University, Ames, IA 50011

⁴ Author to whom correspondence should be directed

4.2. Introduction

Ion conducting glasses are of high interest due to their potential use as solid electrolytes in fuel cell and battery applications^{60,61}. Glasses are exciting as possible electrolytic materials because they have several advantages over their crystalline counterparts⁶¹. These materials offer isotropic conductivity with the absence of grain boundaries. They offer wide compositional flexibility that allows for the optimization of electrolyte properties and can easily be fabricated into complex shapes such as thin films. Very small batteries using ion-conducting thin film glasses can be made and would enable new applications in microelectronics⁶⁰. The variation in ionic conductivity with temperature, composition, and structure is the key to understanding transport phenomena in both glasses and crystals⁶¹.

Recently, Kincs and Martin⁶² reported the discovery of fast ion conducting (FIC) glasses in the AgI, Ag₂S, B₂S₃, and SiS₂ (silver thioborosilicate) system. This complex system was specifically chosen using known relationships for the compositional dependence on ionic conductivity in an effort to develop the highest ionically conducting glass to date⁶³. As a result, the glasses produced in this system have exhibited record high room temperature ionic conductivities as well as good chemical stability, a known problem for chalcogenide systems^{64,65}.

While ionic conductivities as high as $10^{-2} (\Omega\text{-cm})^{-1}$ at room temperature have been measured in this system³, a strong non-Arrhenius temperature dependence decreases the conductivity several orders of magnitude lower than that predicted by the low temperature

Arrhenius behavior. An example of this behavior is shown in Fig. (4-1). This behavior is not exclusive to the silver thioborosilicate system; it has also been observed in, for example, glassy $\text{Ag}_7\text{I}_4\text{AsO}_4$ ⁶⁶ and in the $\text{AgI}+\text{Ag}_2\text{O}+\text{B}_2\text{O}_3$ system⁶⁷.

Several researchers have postulated possible explanations for the non-Arrhenius behavior. Bunde and Maass believe this behavior arises as the result of coulombic interactions between the silver ions at higher temperatures⁶⁸. Ngai has suggested that his coupling model can interpret the data by suggesting that this behavior indicates an upper limit for the ionic conductivity in a glass⁶⁹. Unfortunately these models are unable to describe what physically is happening in the glass to cause the non-Arrhenius deviation. This paper suggests a new model where it is believed that the non-Arrhenius behavior is caused by frequent ion scattering events, scattering of both other mobile ions and lattice ions as well.

4.3. Experimental

4.3.1. Sample Preparation

In preparing the $z \text{AgI} + (1-z)[0.525 \text{Ag}_2\text{S} + 0.475(0.5 \text{B}_2\text{S}_3 + 0.5\text{SiS}_2)]$ FIC samples, the starting materials AgI , Ag_2S , and SiS_2 are commercially available in pure form. B_2S_3 , however, is not commercially available and was prepared in our laboratory by the stoichiometric reaction of boron and sulfur powder in a carbon coated, evacuated silica ampoule⁷⁰.

All FIC glasses were prepared in an oxygen- and water-free (<1 ppm O₂, <1 ppm H₂O) glovebox from stoichiometric amounts of AgI (Cerac, Inc. 99.999%), Ag₂S (Cerac, Inc. 99.9%), B₂S₃, and SiS₂ (Cerac, Inc. 99.5%). Appropriate amounts of these powders were weighed into a vitreous carbon crucible and were heated at 850°C for ten minutes. The samples were then checked for weight loss and were reheated for an additional five minutes. Weight losses were checked and were always less than 1%. The liquid was poured into a brass mold at the anneal temperatures listed in Table (4-1) and allowed to anneal for thirty minutes, then cooled at 5°C/min to room temperature. The glasses were carefully annealed so that they would not anneal at elevated temperatures and in so doing be a possible source of the non-Arrhenius conductivity.

4.3.2. Impedance Spectroscopy

Determining the d.c. conductivity of glasses using d.c. techniques is made more difficult by space charge polarization effects that result from the limited motion of the ions to the blocking electrodes of the glass. Application of a d.c. electric field results in the ions migrating towards and building up at the electrode that is biased opposite to the charge of the ions. This space charge polarization of the ions produces an electric field that is opposite to the applied electric field that acts to reduce further ionic conduction and thereby reduces the measured conductivity far below the true ionic conductivity. Applying an a.c. electric field at frequencies that are greater than the inverse of the relaxation time of the space charge polarization process reduces the magnitude of this effect and allows the true conductivity of the glass to be accurately determined⁷¹.

Impedance spectroscopy involves the application of an a.c. voltage to a sample over a range of frequencies and then measuring the resulting current that is produced and the phase difference between the current and the voltage signals. The data produced is in the form of impedance magnitude, $|Z|$, and phase angle, θ .

The impedance spectrometer used for this investigation was a Solartron 1260 Impedance/Gain Phase Analyzer. A frequency range of 0.01 Hz to 10 MHz was used with an amplitude of 0.05V. A time delay of two seconds between data points and a two second integration time also used to improve the accuracy of the data.

A new sample cell holder was needed to interface between the sample and the impedance analyzer. The holder needed to have very good electrical characteristics, with minimal resistance and stray capacitance, -190°C to 500°C controlled temperature range, hands-free operation over the entire temperature range, the ability to scan from -190°C to 500°C in a series of isothermal steps, and the ability to handle air-sensitive samples. Figures (4-2) and (4-3) are schematic drawings of the new cell. The cell works by passing nitrogen gas through copper coils that are submersed in liquid nitrogen, thus cooling the nitrogen gas to near 80 K. The cold nitrogen gas then passes through a temperature controlled process tube heater and then finally into the sample compartment. Re-circulating the nitrogen back into the cold copper coils thereby reducing its consumption recycles the gas. Controlling the duty cycle of the tube furnace controls the sample temperature; the higher the duty cycle the higher the sample temperature. Nitrogen flow rate of 12 L/min is necessary to obtain stable temperature control within the desired temperature range of -190°C to 500°C.

The impedance spectrometer is computer controlled using software that was jointly developed by the Hahn-Tel Company and the author. This software controls all functions of the impedance spectrometer as well as the temperature control of the sample cell.

4.4. Results

Figure (4-4) shows the real part of the conductivity as a function of frequency and temperature for $0.4\text{AgI}+0.6[0.525\text{Ag}_2\text{S}+0.475(0.5\text{B}_2\text{S}_3+0.5\text{SiS}_2)]$ glasses. This shows the frequency dependence of the conductivity and that the d.c. conductivity increases as temperature is increased. A representative impedance plane plot used to determine the d.c. conductivity of $0.1\text{AgI}+0.9[0.525\text{Ag}_2\text{S}+0.475(0.5\text{B}_2\text{S}_3+0.5\text{SiS}_2)]$ glasses is shown in Fig. (4-5). The arc at high frequency represents the bulk response of the glass to an applied a.c. electric field, by determining where the arc intersects with the Z' axis the dc conductivity is determined⁷². The beginning of a second arc can be seen at lower frequencies, this is believed to be due to polarization effects at the electrodes. As the temperature is increased, the conductivity is also increased, as can be seen in figures (4-4) and (4-6). Unfortunately, as the conductivity of the sample increases the more difficult it becomes to accurately determine the dc conductivity. In figures (4-6) and (4-7) it is seen that the bulk response arcs disappear with increasing temperature and this continues until the arc is completely absent leaving only the polarization arcs. The difficulty of this fact is that the dc conductivity can no longer be directly determined, but must be extrapolated from the polarization "spike" in the complex plane. Figure (4-8) shows several possible extrapolations of the polarization arcs to determine the dc conductivity. While only the middle extrapolation seems reasonable, using

the remaining two as error limits, this amounts to a change in the dc conductivity by only $0.04 \Omega^{-1}\text{-cm}^{-1}$ or 2%. Figure (4-9) shows the results for the dc conductivity so determined for all samples at all temperatures for all studied compositions. As the amount of AgI is increased, so does the deviation from Arrhenius behavior, as illustrated in Fig. (4-10). The activation energy is determined by measuring the slope in the Arrhenius regime.

4.5. Discussion

Ionic conductivity is generally thought to be a thermally activated process⁷³ that can be described by the Nernst-Einstein equation, presented as Eq. (4-1), where σ is the ionic conductivity, D is the diffusivity, n is the number of mobile cations, Z is the valence of the cation, e fundamental unit of charge, k_b is Boltzmann's constant, and T is absolute temperature.

$$\frac{\sigma}{D} = \frac{n \cdot (Z \cdot e)^2}{k_b \cdot T} \quad (4-1)$$

The random walk model gives us the expression for diffusivity⁷⁴, Eq. (4-2), where λ is the jump distance and Γ is the jump frequency. The jump frequency is a thermally activated process that can be determined from Eq. (4-3), where ν_0 is the vibrational frequency of an ion in a potential well and ΔS_m and ΔH_m are the entropy and enthalpy of

$$D = \frac{1}{6} \cdot \lambda^2 \cdot \Gamma \quad (4-2)$$

$$\Gamma = v_0 \cdot e^{\frac{-\Delta H_m}{k_b \cdot T} + \frac{\Delta S_m}{k_b}} \quad (4-3)$$

motion, respectively. Arranging Eq. (4-1) in a more useful form gives Eq. (4-4) and (4-5), where ΔE_A is the activation energy as determined from the slope of an Arrhenius plot and γ is a geometrical constant that describes the number of directions an ion can hop. Inherent in the

$$\sigma = \frac{n \cdot \gamma \cdot (Z \cdot e)^2 \cdot \lambda^2 \cdot v_0 \cdot e^{\frac{-\Delta H_m}{k_b \cdot T} + \frac{\Delta S_m}{k_b}}}{k_b \cdot T} \quad (4-4)$$

Nernst-Einstein equation is three important assumptions. First, it assumes that the activation energy for conductivity is the same as the activation energy for diffusion. Second, it requires that the field strength be sufficiently low so that the conductivity is field independent in order to be compatible with the random walk model⁶¹. Third, it assumes that all diffusive species are charge carries and; therefore, neglects the possibility of a neutral complex⁶¹.

$$\sigma = \frac{\sigma_0}{T} \cdot e^{\frac{-\Delta E_A}{k_b \cdot T}} \quad (4-5)$$

When Eq. (4-5) is plotted in an Arrhenius manner, E_a is equal to the slope. As can be seen in Fig. (4-9), the results of this investigation show that the data is linear in the low temperature region following Eq. (4-5) but deviates at a critical temperature, T_c ⁷¹, into a non-Arrhenius region. Table (4-1) summarizes these results and compares the T_c determined from this investigation to that determined from Kincs. Kincs acknowledges error in his determination of T_c due to the limited amount of data he had above T_c making this determination difficult.

There are several possible explanations for the observed non-Arrhenius behavior. First, a through investigation of the structure and microstructure of the glass was performed to determine that the behavior is inherent to the material and is not an artifact caused by crystallization or phase separation⁷⁵. Maass et al.⁶⁸ suggest that this behavior is the result of coulombic interactions between the silver ions at higher temperatures. Monte Carlo simulations were used and they showed that a model of charged particles moving between the sites of a lattice with random site energies that take into account coulombic interactions the simulation was able to accurately model the experimental data published by Kincs and Martin³. The drawback to this model is that it is successful because it uses several scaling parameters. In addition, it does not explain the nature of the coulombic interaction nor does it explain the differences in conductivity seen from one glass system to another

Ngai and Rizo⁶⁹ suggest that their coupling model explains the non-Arrhenius behavior as a result of an upper limit for the ionic conductivity in a glass. The coupling model was originally developed for dielectric polarization involving permanent dipoles or non-percolating charged particles⁷⁶. This model involves two coupled response equations; the first is applied at very short times and high frequencies and the second is for long times and low frequencies. A crucial assumption that the coupling model makes is that there exists a temperature independent microscopic time, t_c , before which interactions between ions has no effect on the dynamics of an ion. After t_c the interactions between ions do have an effect on the dynamics and would affect the conductivity.

The previous ionic conduction models all include adjustable parameters that allow the respective models to accurately fit experimental results. These parameters are artificial additions that have no physical meaning and are added to overcome the inherent shortcomings of the model. The next part of this investigation attempts to determine the cause of the non-Arrhenius behavior without having to resort to adjustable parameters. By examining what is known about ionic conduction and the structure of these glasses, a new model, the Ion Scattering Model (ISM) is proposed.

As discussed earlier, ionic conduction is the result of thermal hopping of the mobile cation. The ion conductivity of a material can be determined using Eq. (4-6)⁷³,

$$\sigma = n \cdot e \cdot \mu \quad (4-6)$$

where n is the concentration of the conducting species, e is the elementary charge (1.602×10^{-19} C), and μ is the ionic mobility. If the ions and the mobility are simply thermally activated, as would be the case if the conductivity behaved in an Arrhenius fashion, the resulting fit is shown in Fig. (4-1). The fit at low temperatures is quite good, but is very poor at high temperatures.

Examination of Eq. (4-6) shows there are two parameters that any model needs to address: the concentration of the conducting species and the mobility of those species. In determining the concentration of conducting ions, it is important to take into account what is known about the structure of the glass. Since a glass has an amorphous structure, it would be expected that the potential energy wells that the ions sit in would vary in size in shape causing the ions to see a distribution of activation energies. For a thorough discussion as to the presence of a distribution of activation energy (DAE) in FIC glasses, the reader is referred to ref. ⁷⁷. In summary, there is an energy profile in the glass where the conducting ions sit in energy wells. A simple representation of this is shown in Fig. (4-11). The energy barrier for conduction consists of two parts, a coulombic interaction between the conducting cation and the non-bridging sulfur (NBS), and a strain energy that is associated with the strain that occurs when the ion must “squeeze” through interstices in the structure in order to hop to adjacent sites. The total activation energy for conduction is the sum of these two contributions. An extension of this model is to treat the ions as residing in sites that are randomly distributed throughout the glass and are expected to have variations in the local bond distances, bond angles, and coordination numbers that will lead to these sites exhibiting a variation or distribution of activation energies for ionic conduction⁷⁷. The choice of the appropriate mathematical distribution to use for the DAE is subject to choice, however with a

few reasonable assumptions the choices narrow considerably. The DAE is assumed to be continuous, centered about a mean, and symmetrical to high and low values⁷⁷. These assumptions make the use of a Gaussian distribution obvious. A Gaussian distribution takes the form of Eq. (4-7), shown in Fig. (4-12), where E_m is the average activation energy and E_b is the activation energy standard deviation. In principle, the values of E_b and E_m can be experimentally determined by performing NMR experiments on the cation of interest. In the case of this investigation, difficulty in obtaining ^{109}Ag NMR data prohibited experimental determination of these parameters.

$$z(E_a) = \frac{1}{\sqrt{2 \cdot \pi \cdot E_b}} \cdot e^{-\frac{(E_m - E_a)^2}{2 \cdot E_b^2}} \quad (4-7)$$

Integrating Eq. (4-7) between 0 and E_p determines the fraction of ions that are available for conduction. E_p is the percolation limit to the DAE. The percolation theory for ion conducting glasses is well known^{78,79,80,81}. Percolation theory shows that in a simple cubic lattice there only needs to be connectivity of 25.7% of the cation sites with a coordination number of 6 for the energy wells to be connected in order for ionic conduction to occur⁸². This connectivity increases to 38.8% with a coordination number of 4 for the diamond lattice⁸². For this case, typical values obtained in the literature of $E_m = 0.310$ eV, $E_b = 0.040$ eV, and $E_p = 0.191$ eV were used.

To determine the temperature dependence of the DAE, a Boltzmann Distribution is used. At absolute zero, none of the ions have sufficient thermal energy to conduct, regardless of the depth of the potential energy well the ion sits in. At infinite temperature, all of the ions have sufficient energy to overcome their energy barrier to conduct. At intermediate temperatures, the probability depends exponentially on the magnitude of the energy barrier as to whether the ion will successfully make the jump out of the energy well. To determine the probability of an ion at a given energy barrier height will hop as a function of temperature. Eq. (4-8) is used.

$$y(E_a, T) = e^{\frac{-E_a}{k_B T}} \quad (4-8)$$

Multiplying the Boltzmann probability, Eq. (4-8), with the DAE, Eq. (4-7), yields Eq. (4-9), which describes the number density of conducting ions as a function of energy barrier and temperature: this is plotted in Fig. (4-13). When Eq. (4-9) is integrated over the energy barriers below the percolation threshold, the total fraction of conducting ions as a function of temperature is determined Eq. (4-10).

$$A_c(E_a, T) = z(E_a) \cdot y(E_a, T) \quad (4-9)$$

$$n(T) = n_0 \cdot \int_0^{E_p} A_c(E_a, T) dE_a \quad (4-10)$$

If the n as determined from Eq. (4-10) is inserted into Eq. (4-6) and the mobility is left as simply being thermally activated, a fit to the experimental data is determined as shown in Fig. (4-14). Again, the fit at low temperatures is fairly good, but at higher temperatures the fit is poor. Close examination reveals that the trend is actually opposite as that seen in the experimental data. As temperature is increased, the fit deviates in a positive direction from Arrhenius behavior.

Returning to Eq. (4-6), the mobility is the other term that needs to be addressed in order to model the ionic conductivity. If we assume the mobility is limited by mobile ion scattering, as described by the Drude Model⁸³, then Eq. (4-11) is used to determine the ionic mobility, where $\tau(T)$ is the time between collisions as a function of temperature and m is the mass of the ion. While the Drude model was long ago proven incorrect to explain the conduction mechanism for electrons^{83,73} which are quantum particles, in an ion conductor where the ions are not quantum particles the Drude model may be an appropriate model to use.

$$\mu(T) = \frac{\tau(T) \cdot e}{m} \quad (4-11)$$

The Drude Model states that an ion placed in an electric field will continue to accelerate until it encounters a collision. At the time of the collision, the ion will have acquired a velocity, v , which it may lose all or part of at the collision. The time between collisions can be determined if the distance and the velocity between collisions is known.

For each collision, the ion will regain $\frac{3}{2} \cdot k_b \cdot T$ thermal energy, which can be directly converted to kinetic energy using Eq. (4-12). Rearranging Eq. (4-12) to solve for velocity yields Eq. (4-13). The distance between collisions is assumed to be the distance between the silver ions, obtained by neutron scattering to be 3.1 \AA ³⁴.

$$E_{ke} = \frac{1}{2} \cdot m \cdot v^2 = \frac{3}{2} \cdot k_b \cdot T \quad (4-12)$$

$$v(T) = \sqrt{\frac{3 \cdot k_b \cdot T}{m}} \quad (4-13)$$

The time between collisions can now be determined using Eq. (4-14). Figure (4-15) is a plot that shows how the mobile ion concentration and the ion mobility are dependent on temperature. As temperature is increased the ion mobility decreases, but only slightly, compared to the large increase in mobile ion concentration.

$$\tau(T) = \frac{\lambda}{v(T)} \quad (4-14)$$

To see if a good fit and a good trend can be achieved, the results of the DAE model for the concentration of ions combined with the Drude model for the mobility. This combination is referred to as the Ion Scattering Model (ISM). Figure (4-15) shows and compares the temperature dependence of the concentration of mobile ions as well as their mobility. Figure (4-14) shows the resulting fit with experimental data. The fit is not very good, but the trend is very encouraging. As the temperature is increased, the conductivity increases, then at high temperature there is a negative deviation from Arrhenius behavior. The parameters used for the DAE are still the values obtained as typical values found in the literature. These values can be adjusted to improve the fit of the model, Fig. (4-16). Table (4-2) summarizes the values of E_m and E_p used for all compositions; E_b was left as 0.040 eV. It is interesting to note that as the amount of AgI is increased, the amount that E_m and E_p change with respect to the activation energy is nearly constant but results in a significant increase in the percolation fraction.

Notice in Fig. (4-16) that the ISM appears to have a good fit at high temperature where the experimental data is non-Arrhenius but that simple Arrhenius behavior is observed at low temperatures. The experimental data appears to be a combination of the two models. At low temperatures, it is believed that the infrequent thermal activation of only a small number of silver ions allows these ions to conduct independently. There are such a small

number of mobile ions, that the ions do not “see” any other ions; since they do not interact, they do not scatter. Because the ISM model assumes ion scattering is the limiting phenomenon for conduction, it assumes that an ion is never allowed to conduct independently, as would happen when very few ions are mobile. As a result it is not surprising that the low temperature fit of the ISM is poor. The next step for the advancement of this model would be to determine the nature of the changeover from Arrhenius to ion scattering. This changeover would define a scattering threshold above which the ions begin to interact. The addition of one scaling parameter that would switch the model from following Eq. (4-5) to the ISM would likely produce a good fit through all temperature regimes. Since a goal of this investigation was to understand the non-Arrhenius dependence without the use of scaling parameters, this was not performed.

4.6. Conclusions

High temperature conductivity measurements of $z \text{ AgI} + (1-z)[0.525 \text{ Ag}_2\text{S} + 0.475(0.5 \text{ B}_2\text{S}_3 + 0.5 \text{ SiS}_2)]$ where $0 \leq z \leq 0.4$ FIC glasses were performed to determine the conductivity behavior above room temperature. A distinct non-Arrhenius deviation is observed that causes the dc conductivity to be lower than is expected by extrapolating the low temperature results. This deviation becomes more pronounced and occurs at lower temperatures as AgI content is increased.

A new model is proposed, the Ion Scattering Model, which takes a physical approach to explain the cause of the non-Arrhenius deviation. By assuming the high temperature conductivity is limited by mobile ion scattering, good fits with experimental data was

achieved in the non-Arrhenius region. Due to the assumption that the ions do not conduct independently the low temperature conductivity is over-estimated.

4.7. Acknowledgements

This work was supported by the National Science Foundation grant number DMR-99-72466.

4.8. References

-
- ⁶⁰ Balkanski, M., *Physics World*, 29-33 (1990)
- ⁶¹ Fusco, F. A., Tuller, H. L., *Fast Ion Transport in Glasses*; p. 43; Superionic Solids and Solid Electrolytes; Academic press (1989)
- ⁶² Kincs, J., Martin, S. W., *Phys. Rev. Lett.*, **76**, 70-73
- ⁶³ Kincs, J., Masters Thesis, Iowa State University (1994)
- ⁶⁴ Uryanitsa, I.D., Khiminets, V.V., Timko, T.V., *Zh. Prikl. Khim.*, **48**(6) (1975)
- ⁶⁵ Funtikov, V., *Proc. Int. Congr. Glass*, 18th, 2781-2786 (1998),
- ⁶⁶ Ingram, M.D., Grant, R.J., Turner, L.D.S., Vincent, C.A., *J. Phys. Chem.* **82**, B26B (1978)
- ⁶⁷ Shaju, K.M., Chandra, S., *Phys. Stat. Sol (b)* **181**, 301 (1994)
- ⁶⁸ Maass, P., Meyer, M., Bunde, A., Dieterich, W., *Phys. Rev. Lett.* **77**, 1528 (1996)
- ⁶⁹ Ngai, K.L., Rzos, A.K., *Phys. Rev. Lett.* **76**, 1296 (1996)
- ⁷⁰ Martin, S.W., Bloyer, D., *J. Am. Ceram. Soc.*, **74**, 1003 (1991)
- ⁷¹ Kincs, J., Masters Thesis, Iowa State University (1994)
- ⁷² McDonald, J.R., Impedance Spectroscopy: Emphasizing Solid Materials and Systems, John Wiley & Sons (1987)
- ⁷³ Hummel, R.E., *Electronic Properties of Materials*, 2nd ed., Springer-Verlag (1993)
- ⁷⁴ Porter, D.A., Easterling, K.E., Phase Transformation in Metals and Alloys, Van Nostrand Reinhold (UK) (1981)
- ⁷⁵ Schrooten, J., Meyer, B., Martin, S.W., *J. Non-Cryst. Sol.*, to be published
- ⁷⁶ Macdonald, J. R., *J. Appl. Phys.*, **84**, 812-827 (1998)
- ⁷⁷ Martin, S.W., Borsa, F., Svare, I., to be published
- ⁷⁸ Blair, H.D., Milberg, M.E., *J. Am. Ceram. Soc.*, **57**, 257 (1974)
- ⁷⁹ Krogh-Moe, J., *Arkiv Kemi*, **14**, 553 (1959)
- ⁸⁰ Krogh-Moe, J., *Phys. Chem. Glasses*, **1**, 26 (1960)
- ⁸¹ Greaves, G.N., Fontain, A., Lagarde, P., Raux, D., Gurman, S.J., *Nature*, **293**, 611 (1981)
- ⁸² Svare, I., Borsa, F., Torgeson, D.R., Martin, S.W., *Phys. Rev. B.*, **48**, 13 (1993)
- ⁸³ Benson, H., University Physics, John Wiley & Sons (1991)
- ⁸⁴ Matic, A., Swenson, J., Börjesson, L., Akai, T., Schrooten, J., Martin, S.W., to be published
- ⁸⁵ Martin, S.W., *J. Am. Ceram. Soc.*, **74**, 1767 (1991)

4.9. Captions

Table (4-1): Summary of conductivity results

Table (4-2): Parameters used in the ISM

Figure (4-1). Plot of the d.c. conductivity showing the transition from Arrhenius behavior at low temperatures to non-Arrhenius behavior at higher temperatures for a glass of composition $0.3 \text{ AgI} + 0.7[0.525 \text{ Ag}_2\text{S} + 0.475(0.5 \text{ B}_2\text{S}_3 + 0.5 \text{ SiS}_2)]$.

Figure (4-2). Schematic drawing of the specialized conductivity cell used for temperature dependent impedance spectroscopy.

Figure (4-3). Schematic drawing of the sample compartment of the conductivity cell.

Figure (4-4). Plot showing the frequency dependence of the real conductivity for glass of composition $0.4 \text{ AgI} + 0.6[0.525 \text{ Ag}_2\text{S} + 0.475(0.5 \text{ B}_2\text{S}_3 + 0.5 \text{ SiS}_2)]$. The low frequency polarization data has been removed from this plot to facilitate easier reading.

Figure (4-5). Impedance plane plot at -127°C illustrating the method used to determine the d.c. conductivity.

Figure (4-6). Plot showing the low temperature dependence of the impedance data for glasses of composition $0.4 \text{ AgI} + 0.6[0.525 \text{ Ag}_2\text{S} + 0.475(0.5 \text{ B}_2\text{S}_3 + 0.5 \text{ SiS}_2)]$.

Figure (4-7). Plot showing the high temperature dependence of the impedance data for glasses of composition $0.4 \text{ AgI} + 0.6[0.525 \text{ Ag}_2\text{S} + 0.475(0.5 \text{ B}_2\text{S}_3 + 0.5 \text{ SiS}_2)]$.

Figure (4-8). Plot illustrating method of determining error in the d.c. conductivity results.

Figure (4-9). Plot of the temperature dependence of the d.c. conductivity for samples of composition $z \text{ AgI} + (1-z)[0.525 \text{ Ag}_2\text{S} + 0.475(0.5 \text{ B}_2\text{S}_3 + 0.5 \text{ SiS}_2)]$.

Figure (4-10). Plot emphasizing the deviation from Arrhenius behavior as AgI concentration increases.

Figure (4-11). Schematic representation of a possible potential energy surface for ion conduction in an FIC glass⁸⁵.

Figure (4-12). Plot of the distribution of activation energy as modeled for 0.3 AgI+0.7[0.525 Ag₂S+ 0.475(0.5 B₂S₃+0.5 SiS₂)]

Figure (4-13). Representation of the fraction of conducting ions as a function of energy barrier height and temperature.

Figure (4-14). Comparison between experimental data with different stages of the Ion Scattering Model.

Figure (4-15). Comparison plot showing the temperature dependence of mobile ion concentration and ion mobility.

Figure (4-16). Comparison between the optimized ISM and experimental data.

Table (4-1)

$z \text{ AgI} + (1-z)[0.525$ $\text{Ag}_2\text{S} + 0.475(0.5$ $\text{B}_2\text{S}_3 + 0.5 \text{ SiS}_2)]$	Activation energy for ionic conduction (eV) ($\pm 0.005 \text{ eV}$)	Critical Temperature, T_c (K)	Critical Temperature, T_c (K) (from ref 71)
$z = 0.0$	0.281	330	315
$z = 0.1$	0.285	301	300
$z = 0.2$	0.251	225	300
$z = 0.3$	0.217	208	258
$z = 0.4$	0.207	194	183

Table (4-2)

$z \text{ AgI} + (1-z)[0.525$ $\text{Ag}_2\text{S} + 0.475(0.5$ $\text{B}_2\text{S}_3 + 0.5 \text{ SiS}_2)]$	E_a ($\pm 0.005 \text{ eV}$)	E_m	E_p	Percolation Fraction
$z = 0.0$	0.281	$0.8 \cdot E_a$	$0.6 \cdot E_a$	1.4%
$z = 0.1$	0.285	$0.8 \cdot E_a$	$0.6 \cdot E_a$	1.3%
$z = 0.2$	0.251	$0.8 \cdot E_a$	$0.6 \cdot E_a$	2.2%
$z = 0.3$	0.206	$0.95 \cdot E_a$	$0.6 \cdot E_a$	2.5%
$z = 0.4$	0.207	$0.95 \cdot E_a$	$0.7 \cdot E_a$	7.0%

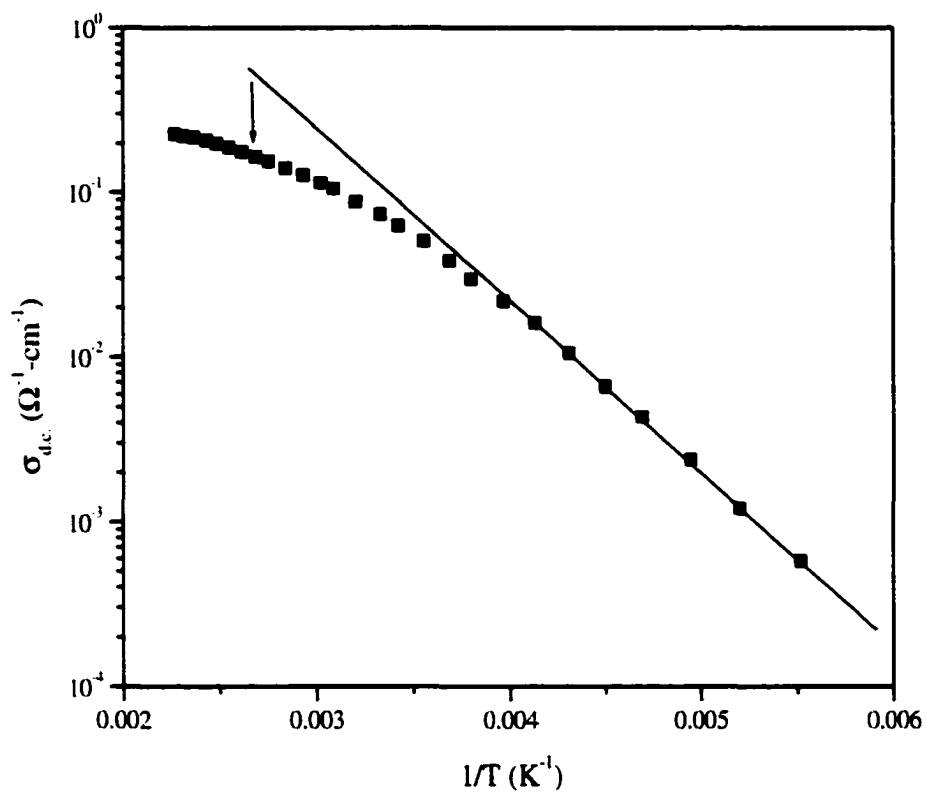


Figure (4-1)

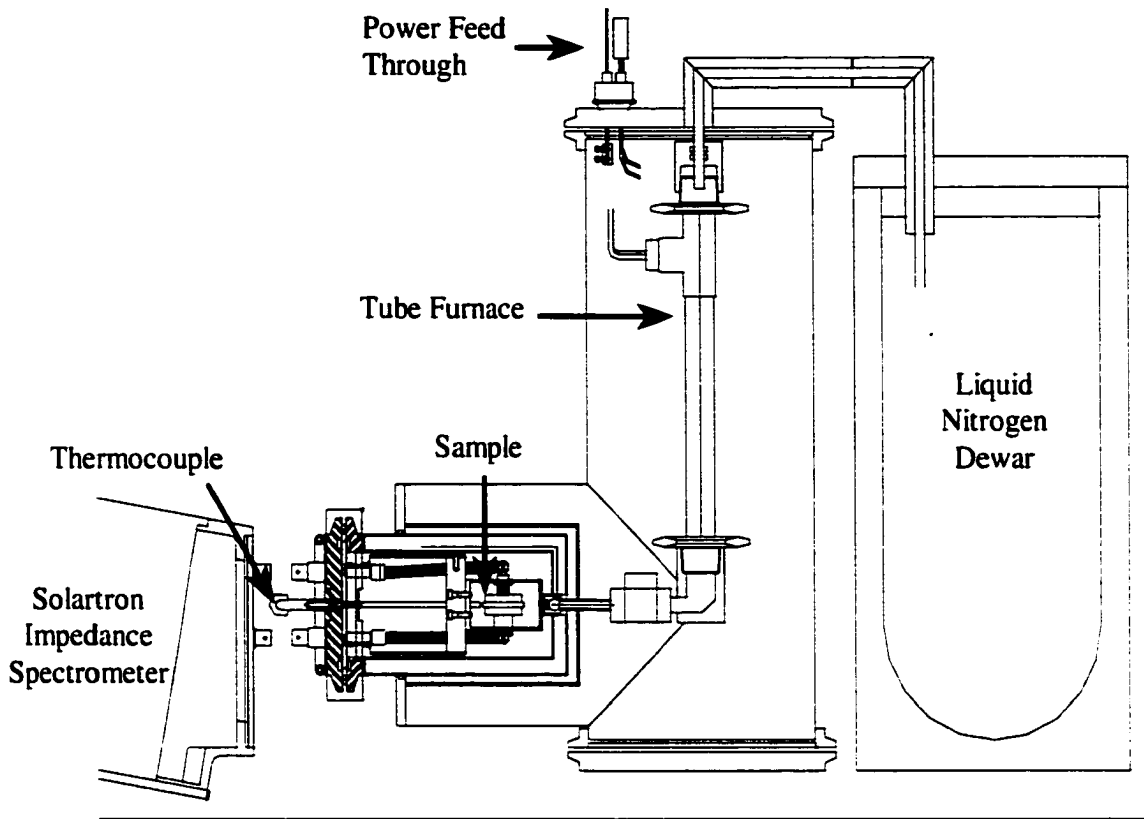


Figure 4-2

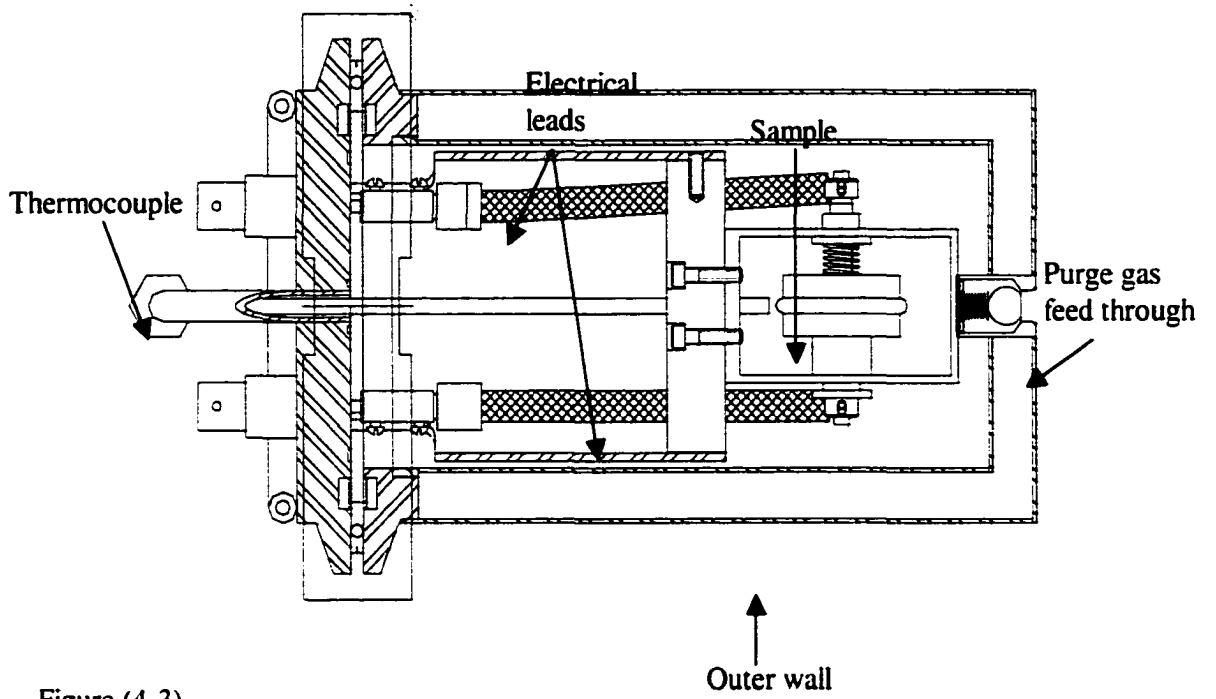


Figure (4-3)

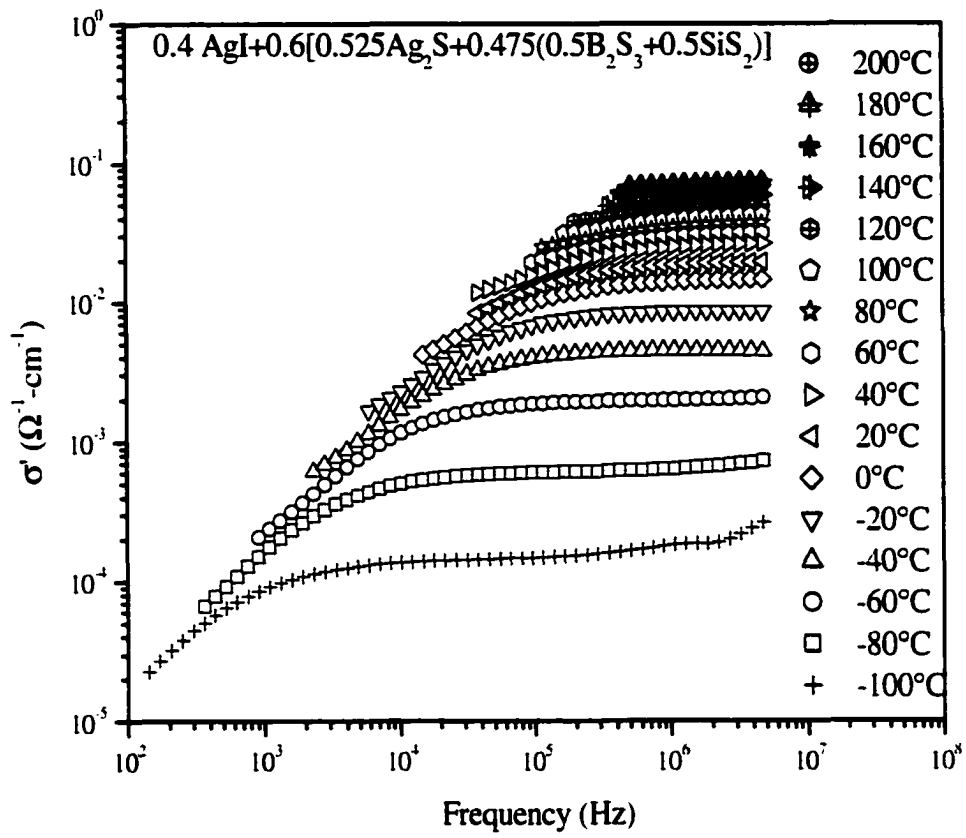


Figure (4-4)

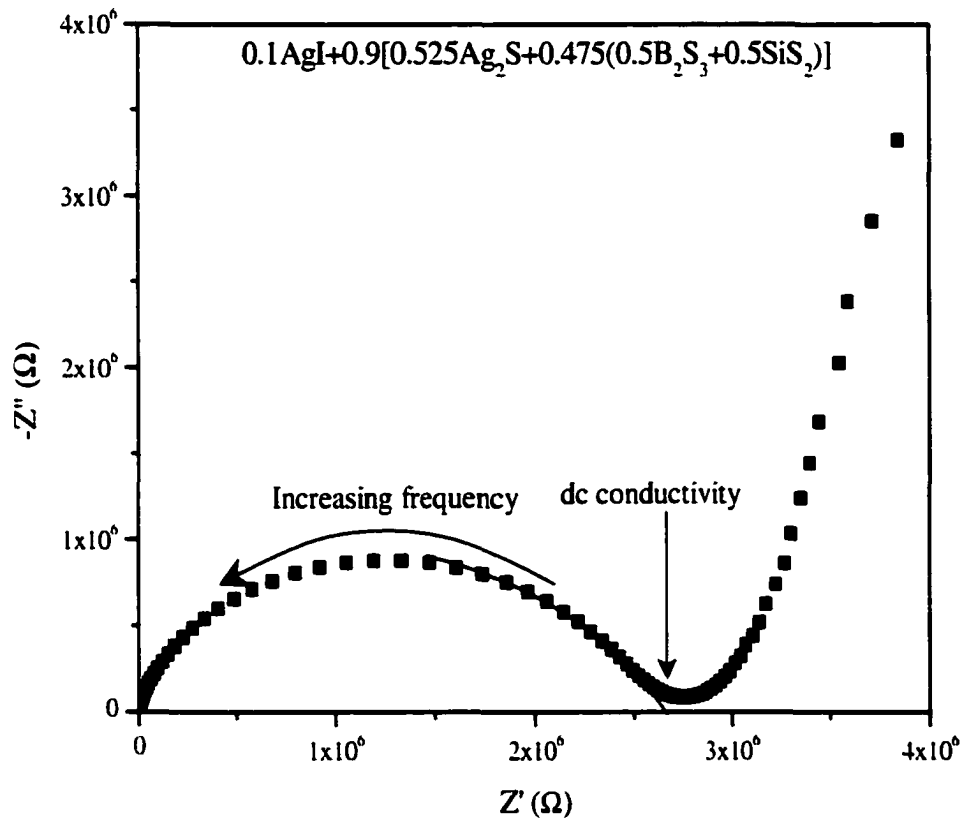


Figure (4-5)

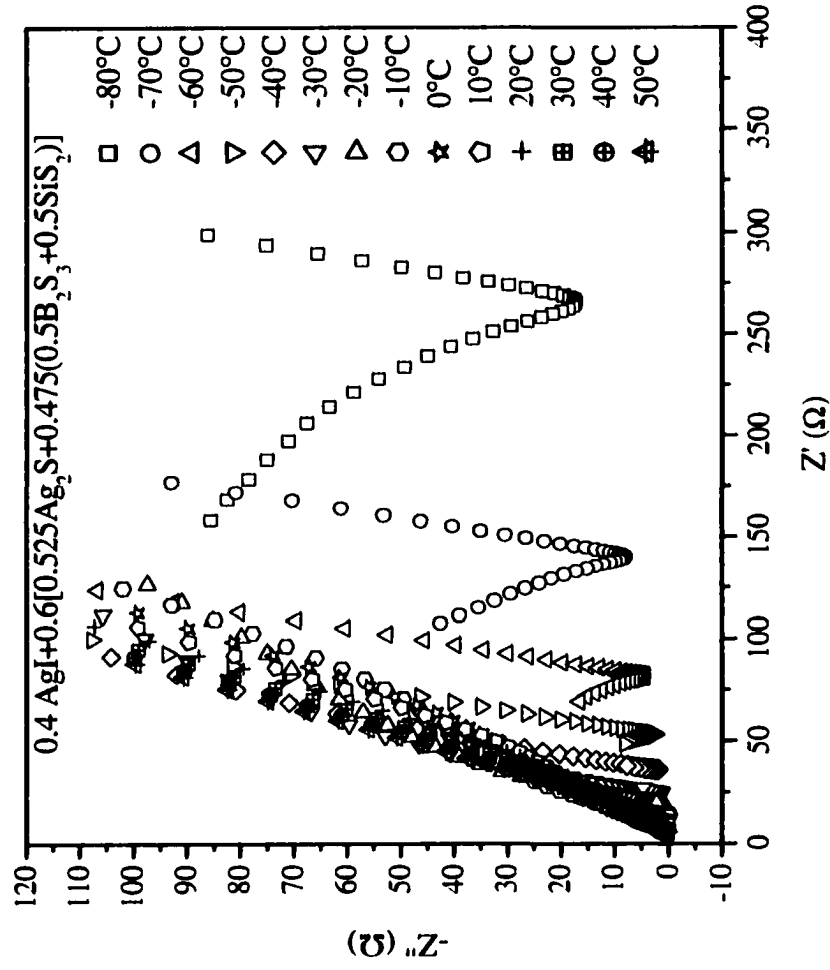


Figure (4-6)

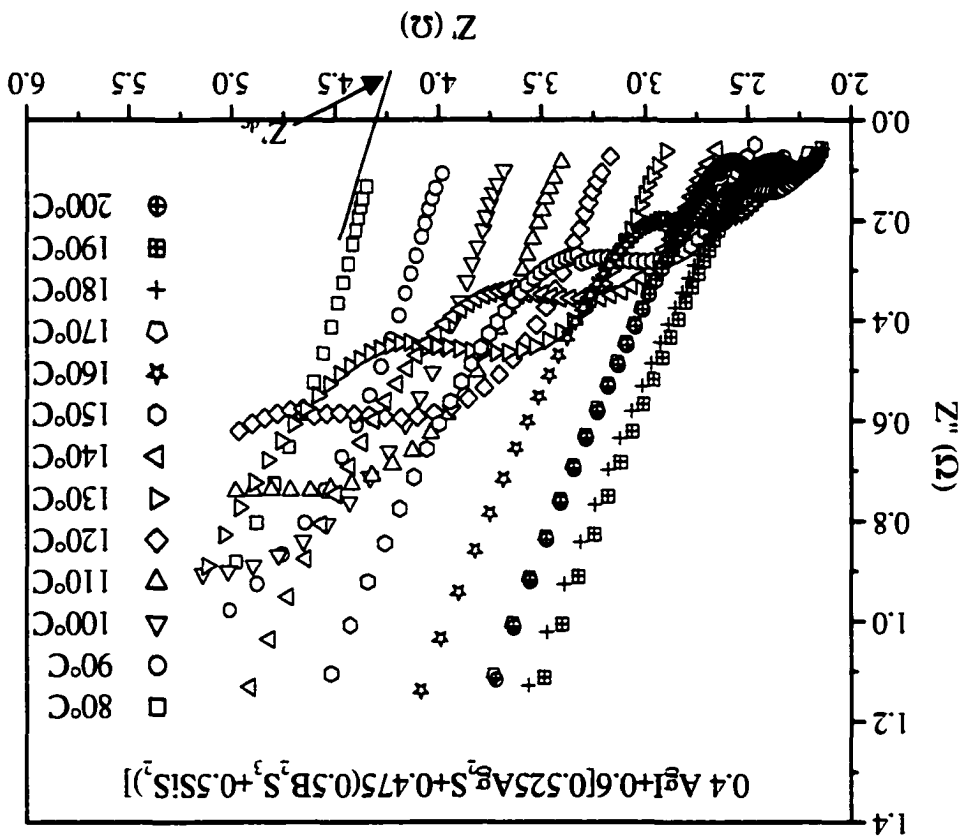


Figure (4-7)

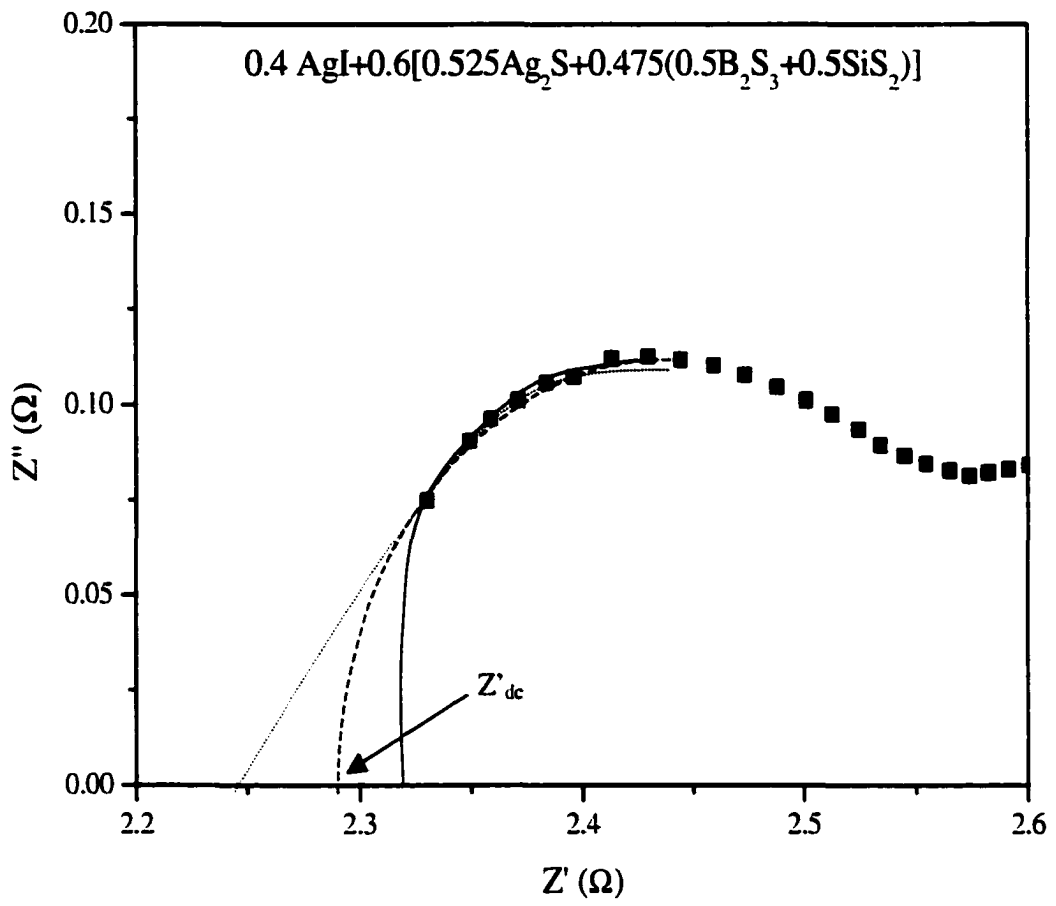


Figure (4-8)

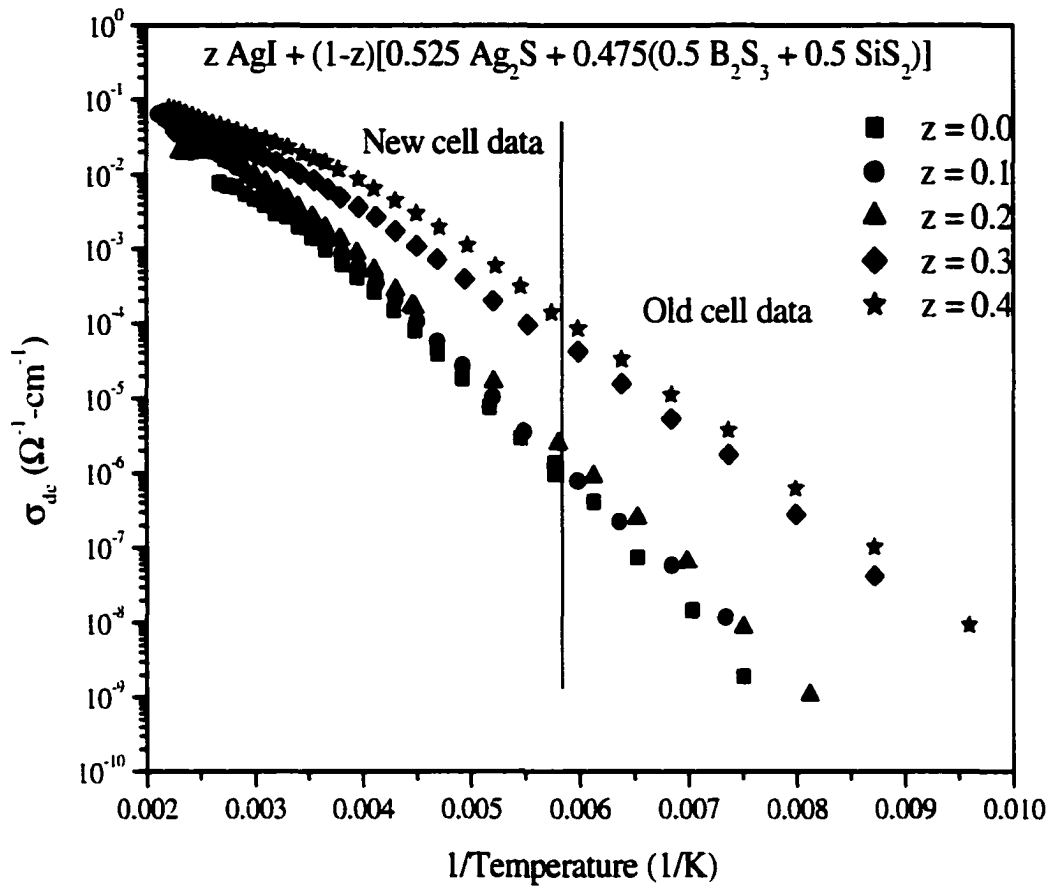


Figure (4-9)

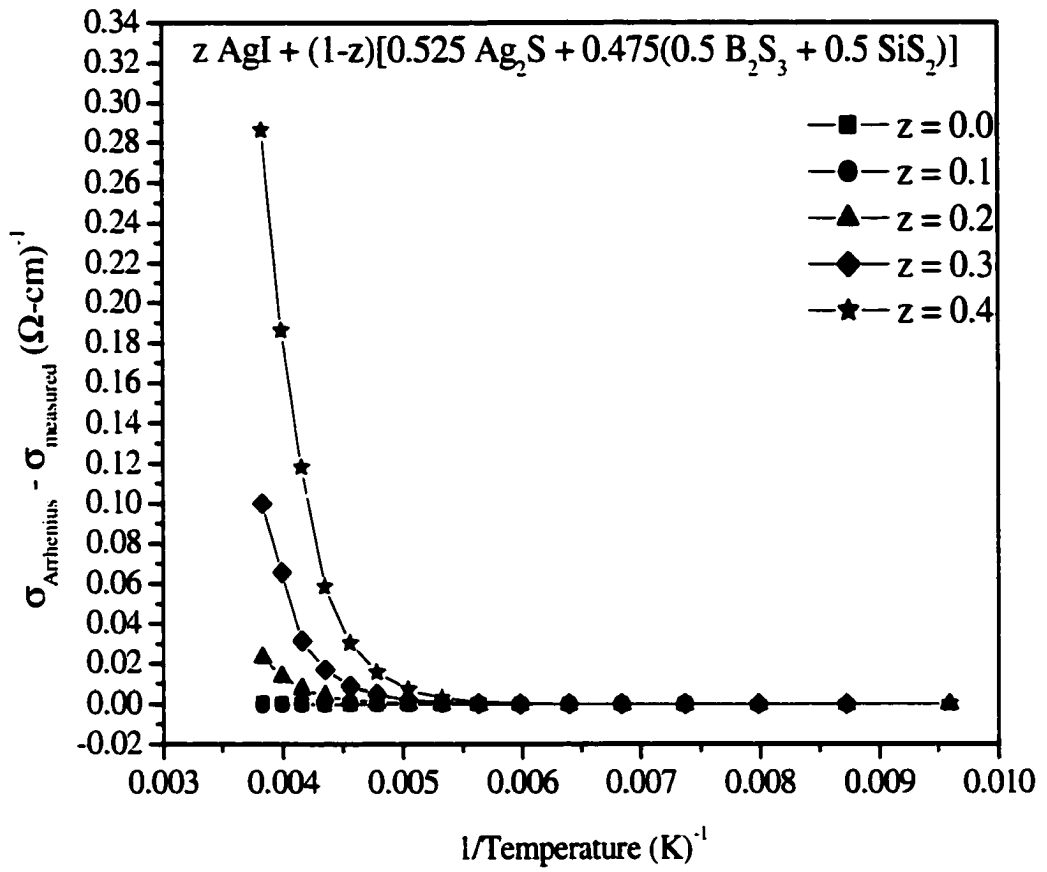


Figure (4-10)

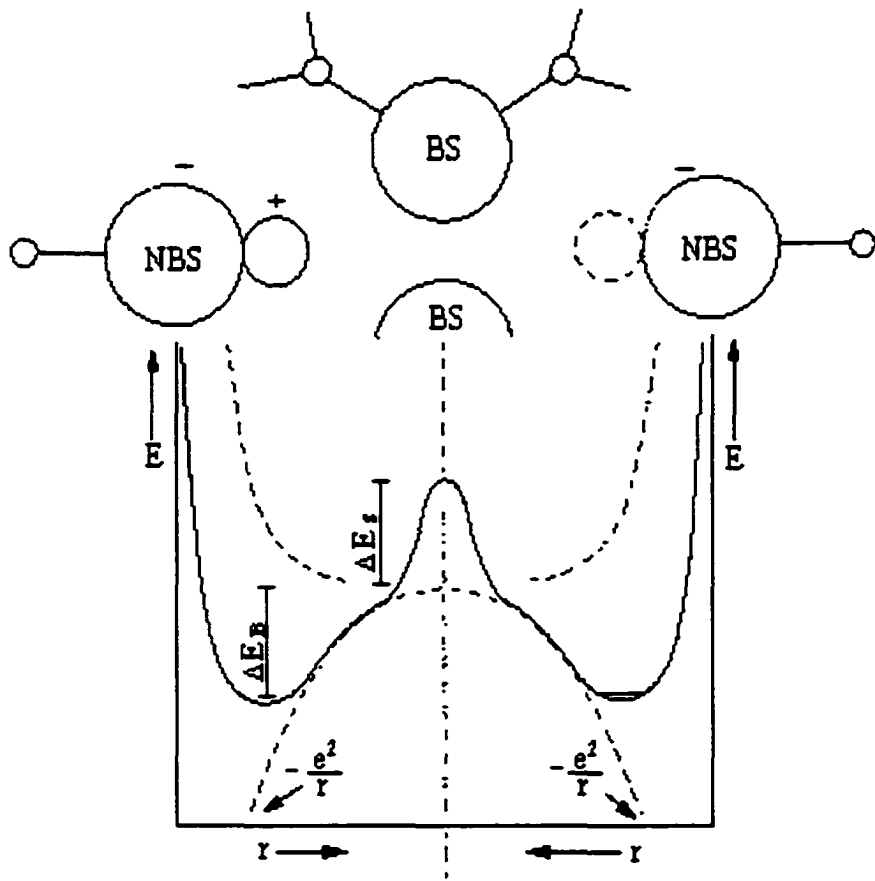


Figure (4-11)

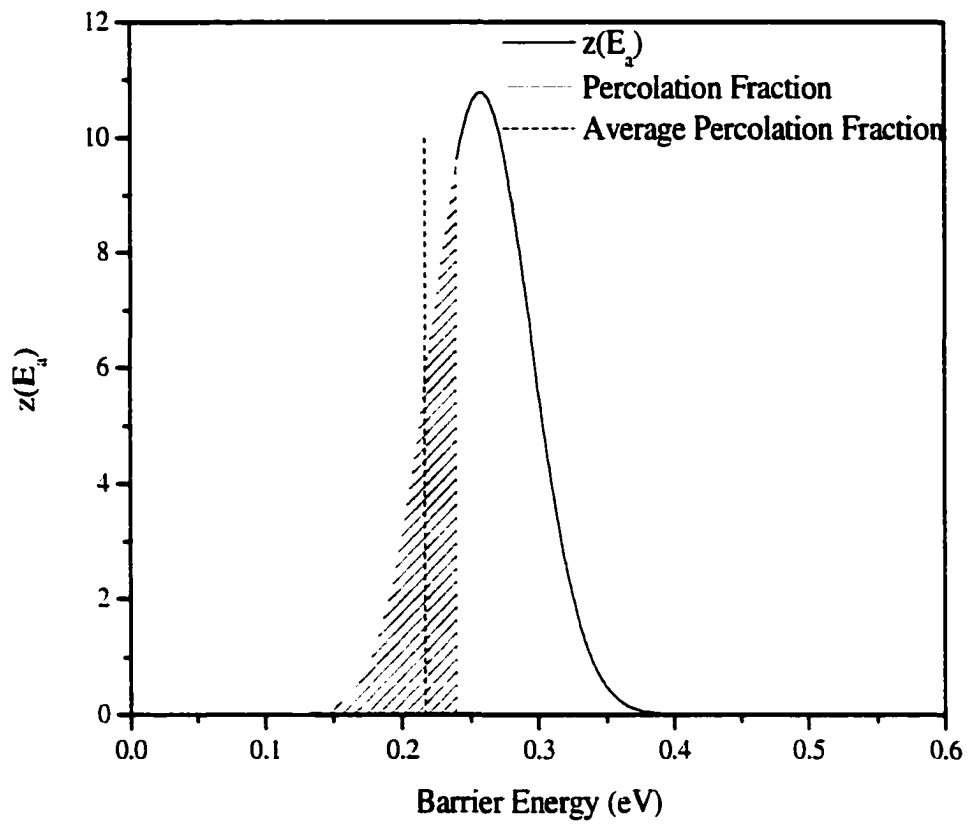


Figure (4-12)

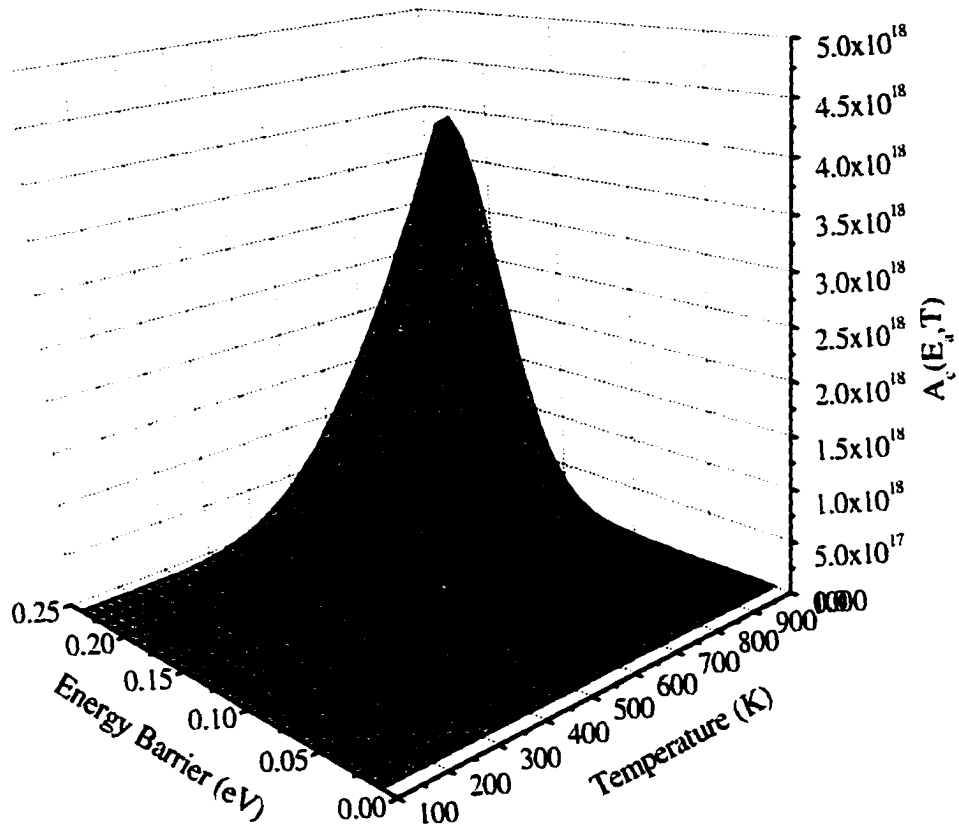


Figure (4-13)

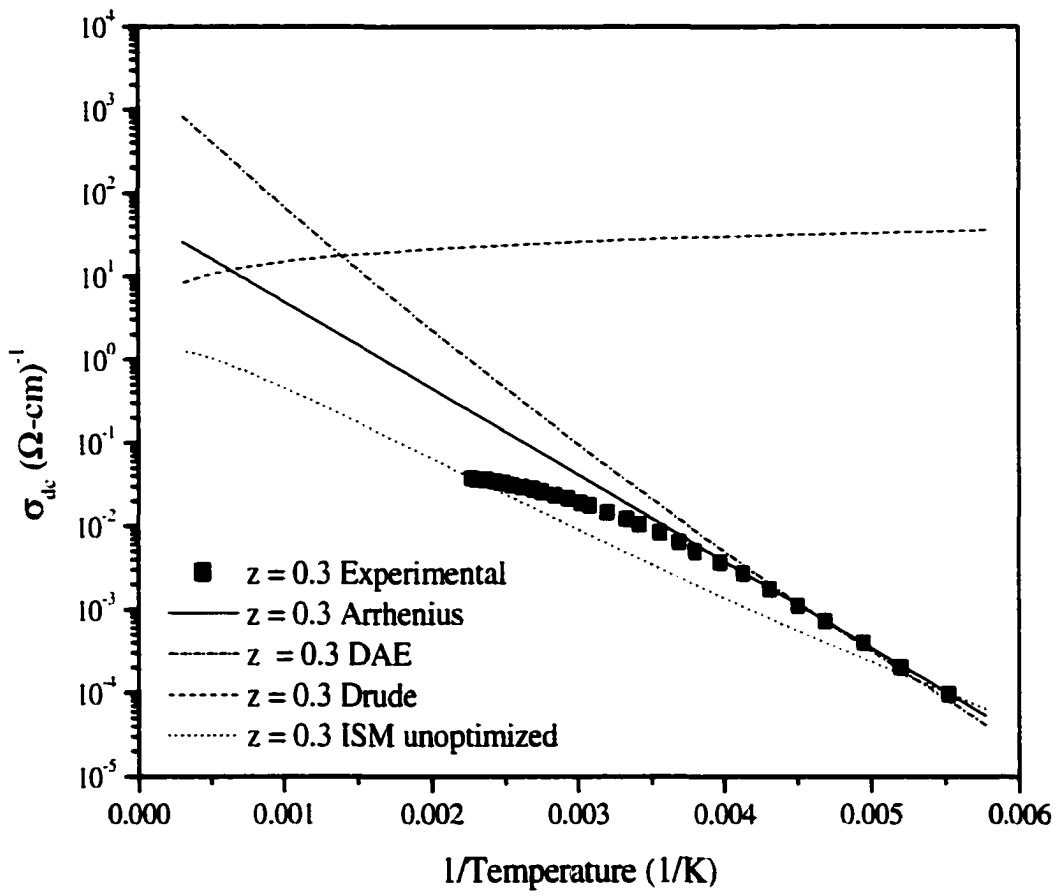


Figure (4-14)

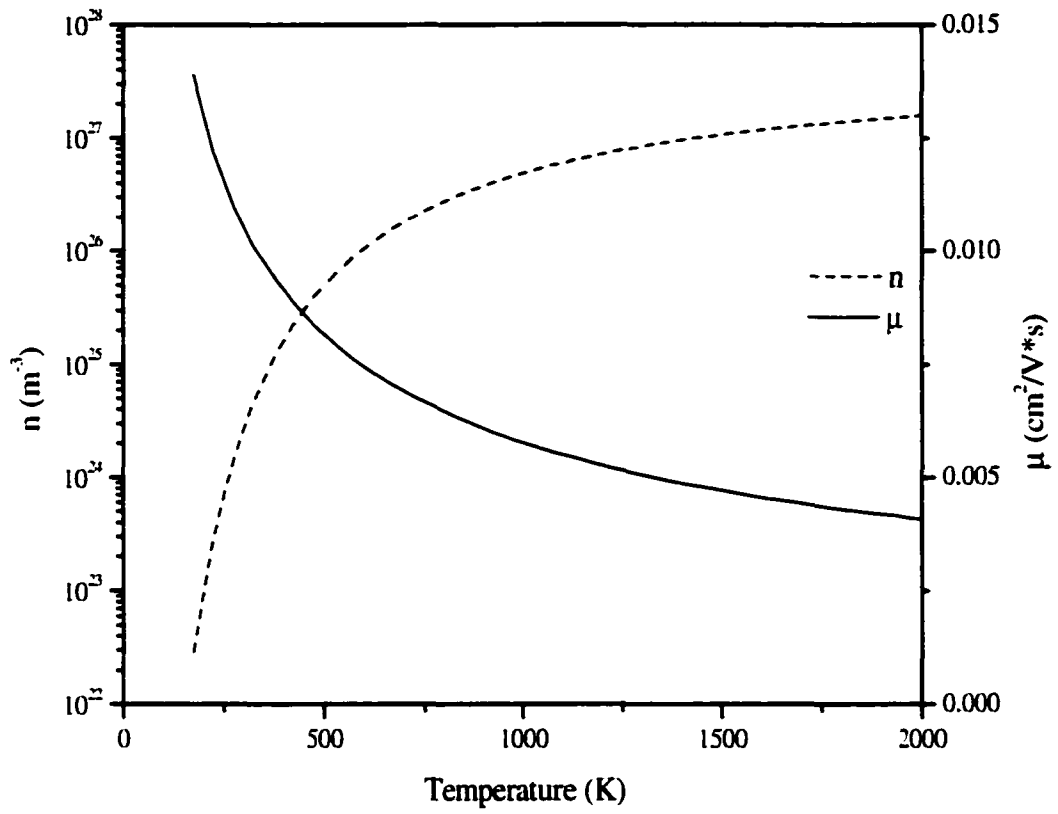


Figure (4-15)

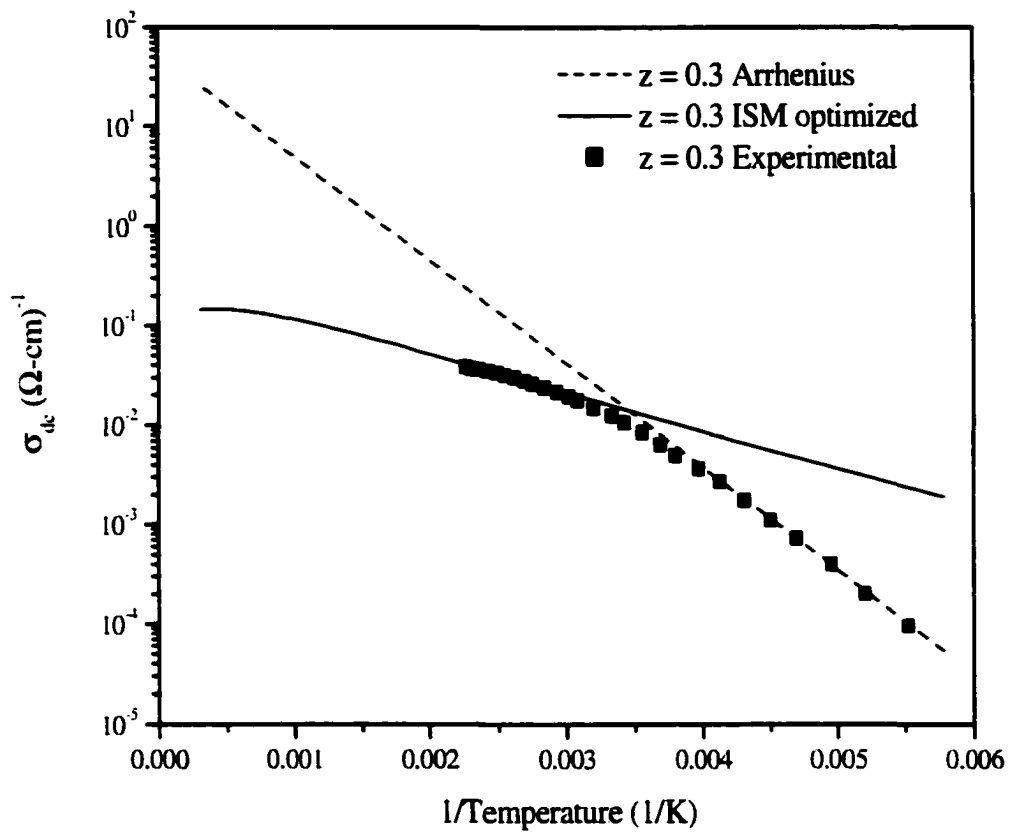


Figure (4-16)

5. General Conclusion

5.1. General Discussion

The driving force of this investigation was that fast ion conducting materials have a potential in applications as electrolytes in fuel cells and batteries. For such applications, high ionic conductivity is desirable coupled with high electrochemical stability. The non-Arrhenius temperature dependence to the ionic conductivity may become a limiting factor for the ionic conductivity thus limiting the potential applicability of such materials.

Several considerations were given as to the nature of the non-Arrhenius dependence. First off, it needed to be confirmed as a real behavior, and not a result of imperfect samples. Secondly, the high temperature nature needed to be established; would the conductivity saturate or maximize. Finally, a cause needed to be determined.

In Chapter 3, a thorough investigation was presented that showed the non-Arrhenius behavior was likely a true effect. SEM and XRD analysis confirmed that the samples were homogeneous and glassy. The structure of the glass samples was studied and determined that the glass is primarily composed of SiS_2 and BS_2 tetrahedra with small amounts of B_2S_3 six-membered rings and trigonal units. These structural units appear to intermix with the Ag_2S adding equally to the B_2S_3 structures and to the SiS_2 structures. The addition of AgI has very little effect on the structure of the glass due to AgI dissolving into voids in the glass causing a network expansion. This occurs without disrupting the short-range order of the glass.

Chapter 4 explored the high temperature behavior of the ionic conductivity to near the glass transition temperature of the samples and determined that the ionic conductivity continued to increase, but at a much slower rate than at lower temperatures. The trend is of ionic conductivity saturation, without exhibiting a maximum; however, the glass transition

occurs before this could be conclusively determined. This chapter also introduced the Ion Scattering Model, which takes a physical approach to explain the cause of the non-Arrhenius deviation. By assuming the high temperature conductivity is limited by mobile ion scattering, good fits with experimental data could be achieved in the non-Arrhenius region. However, due to the assumption that the ions do not conduct independently, the low temperature conductivity was over-estimated.

5.2. Recommendations for Future Research

One of the most challenging parts of this investigation was the determination of the d.c. conductivity. Because the investigated glass system is such a good ionic conductor, it was not possible to experimentally determine the dc conductivity. Instead, it was extrapolated. As was shown in Chapter 4, the error is thought to be quite low. In order to experimentally reach the frequency independent region where the d.c. conductivity can be determined; it is necessary to perform impedance spectroscopy measurements at higher frequencies. The setup, performance, and analysis of these measurements would likely be a thesis in-itself, but I believe the results would be worth the effort.

6. Acknowledgements

I would like to thank Dr. Steve W. Martin for his expert guidance and support through both the good times and the bad times. As we learned the hard way, research is much more fun with funding than without!

I would also like to thank Ben Meyer, Brad Tischendorf, Mike Royle, Jason Saienga, and Chad Martindale whose very thoughtful discussions often helped point the way, even if it was the wrong way...

Finally, I never would have made it without the unending and unconditional support of my wife Amy. She was always there when I needed her.

Thank you all very, very much.